

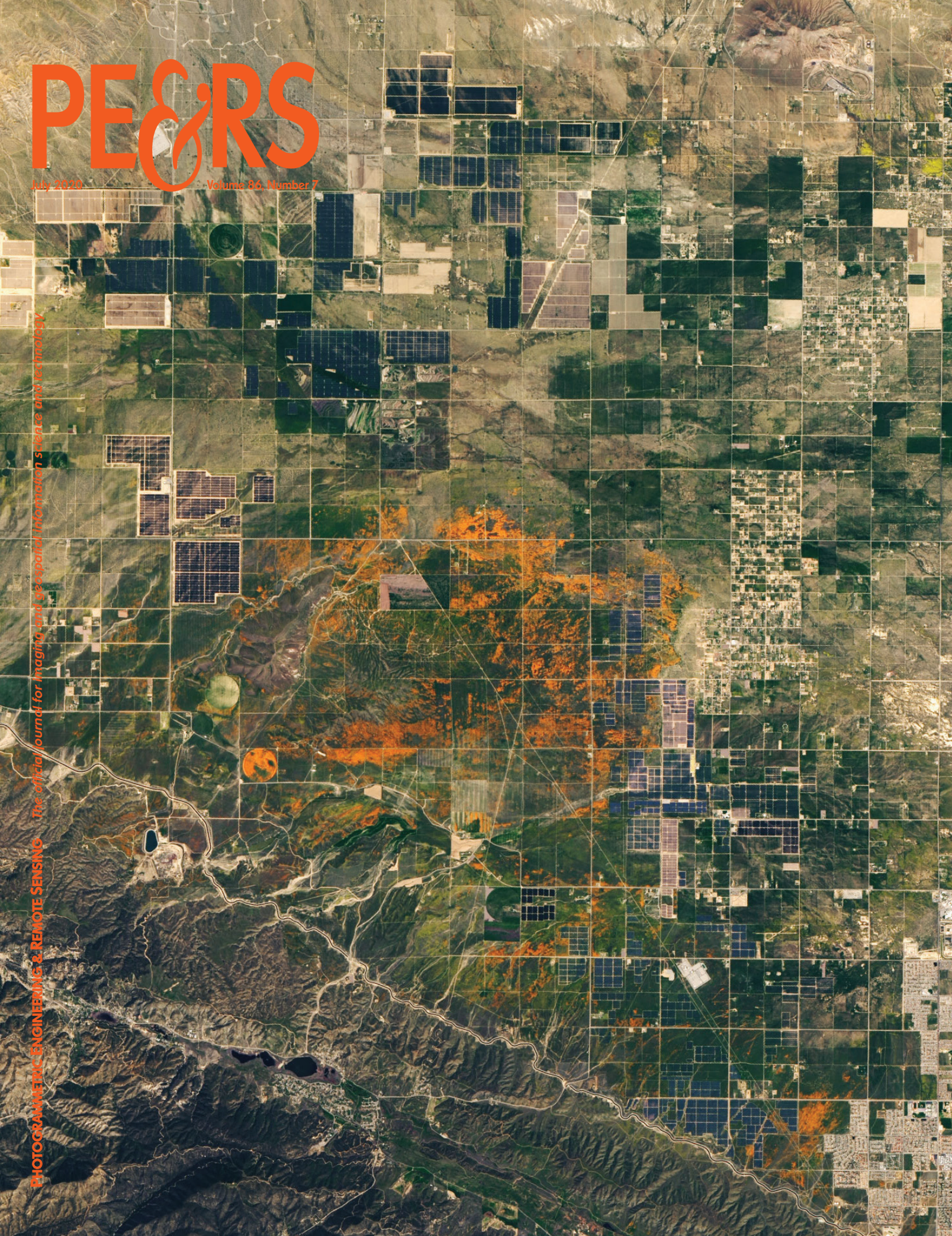
PE&RS

July 2020

Volume 86, Number 7

PHOTOGRAMMETRIC ENGINEERING & REMOTE SENSING

The official journal for imaging and geospatial information science and technology



NEW
AWARDS UP TO
\$500K



INNOVATE

TRANSFORM OUR FUTURE

R&D FUNDING PROGRAM

The National Reconnaissance Office Director's Innovation Initiative (DII) Program funds cutting-edge scientific research in a high-risk, high-payoff environment to discover innovative concepts and creative ideas that transform overhead intelligence capabilities and systems for future national security intelligence needs. The program seeks the brightest minds and breakthrough technologies from industry, academia, national laboratories, and U.S. government agencies.

Visit the website for Broad Agency Announcement and Government Sources Sought Announcement requirements.

703.808.2769



www.nro.gov/Business-Innovation-Opportunities



WHITTLES PUBLISHING

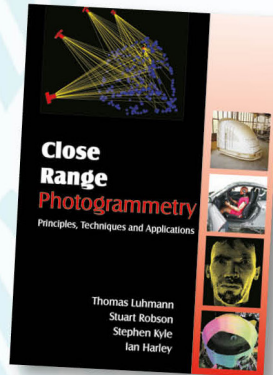
SIMPLY BRILLIANT BOOKS

ASPRS
MEMBER EXCLUSIVE

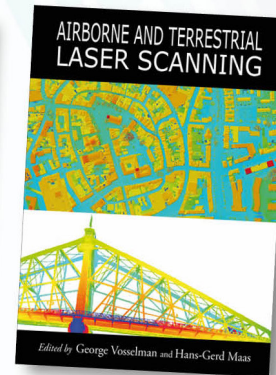
20%
DISCOUNT

ON ALL WHITTLES PUBLISHING BOOKS
USING CODE WPASPRS2

WHITTLES PUBLISHING'S STABLE OF CLASSIC GEOMATICS BOOKS INCLUDES THE THREE WINNERS OF THE PRESTIGIOUS KARL KRAUS MEDAL AWARDED BY ISPRS



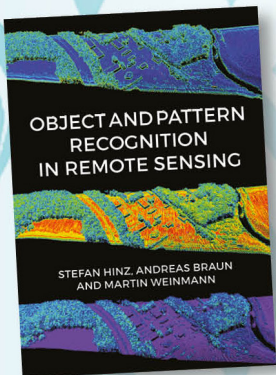
978-1870325-73-8
(Available as a CD)



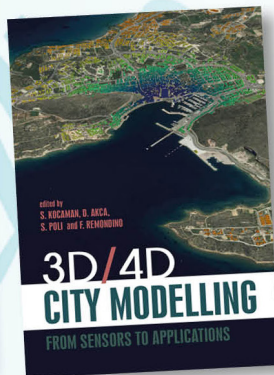
978-1904445-87-6



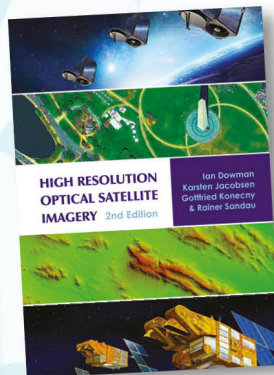
ISBN? Website only has 2nd edition



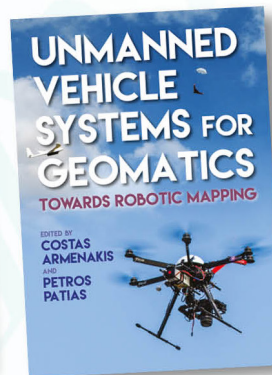
978-184995-128-9



978-184995-475-4



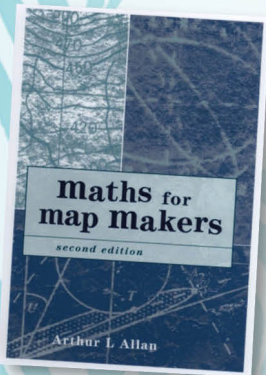
978-184995-390-0



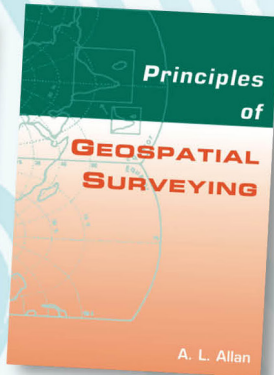
978-184995-127-2

OUR LIST CONTINUES TO EXPAND WITH THESE NEW TITLES

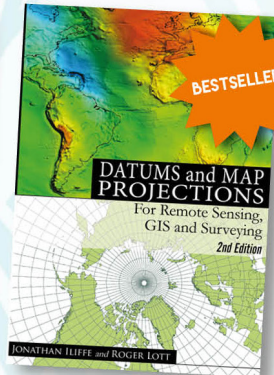
BROWSE OUR WEBSITE TO SEE OUR FULL RANGE OF ACCLAIMED GEOMATICS BOOKS



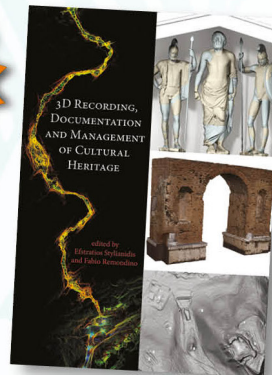
978-1870325-99-8



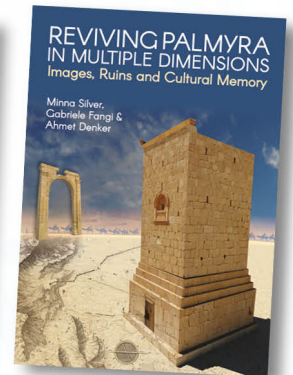
978-1904445-21-0



978-1904445-47-0



978-184995-168-5



978-184995-296-5

ANNOUNCEMENTS

California geomatics engineering firm, **Towill, Inc.** (Towill), announces the acquisition of Cunha Engineering, Inc. (Cunha) of Pinole, California. The acquisition will augment and diversify Towill's land surveying services in the SF Bay Area and throughout the state of California.

"While the closing of this transition comes during unusual times, it's been a long-term goal of both firms and a well-planned acquisition," says Towill President Ken Meme, CP, RPP. "We see this investment as an excellent way to increase our presence in critical market sectors while strengthening our team. There is a great synergistic and cultural fit between the two firms that will help us better serve clients, integrate and maximize the potential of our personnel, and bring the combined firm cross-selling opportunities. Both businesses have enjoyed robust performance in spite of the global pandemic and we look forward to even better results when the crisis abates."

Operating from seven offices strategically located throughout California and one office in Colorado Springs, Towill is well-positioned to serve the Western United States. This acquisition combines the expertise and wide range of services of the two firms and will expand Towill's depth of resources to better serve clients in multiple markets.

For more information, contact Dawn Antonucci, dawn.antonucci@towill.com.

URISA is pleased to present the following list of candidates for URISA President-Elect and for Directors on the Board.

For President-Elect: Brent Jones, PE, PLS, Global Manager, Land Records/Cadastre, Esri, Vienna, Virginia

For Board of Directors (to fill 3 positions):

- Kathryn Brewer, GISP, Partner, Spatial Relationships LLC, Boston Massachusetts
- **Xan Fredericks**, GISP, Lidar Coordinator/Associate National Map Liaison, US Geological Survey, Saint Petersburg, Florida
- Tari Martin, GISP, Director, National & Federal, National Alliance for Public Safety GIS (NAPSG) Foundation, Washington, DC
- Pravin Mathur, GISP, Clark Nexsen, Virginia Beach, Virginia
- Joseph Sloop, GISP, Geographic Information Officer, Forsyth County, Winston-Salem, North Carolina
- Steven J. Steinberg, PhD, GISP, Geographic Information Officer, Los Angeles County, Los Angeles, California

The official ballots will be distributed to the entire URISA membership by the end of June. The deadline for URISA members to cast their votes is July 30. To help members decide for whom to vote, each candidate will provide a profile of their professional experience and a statement about their ideas for URISA's future.

Those elected will begin their three-year Board terms following <https://www.urisa.org/gis-pro>.

EQUIPMENT/TECHNOLOGY

Spectral Evolution now offers a portable, compact four inch reflectance/transmittance (R/T) integrating sphere for measuring the reflectance and transmittance of a wide variety of material types.

The 4 inch R/T sphere is lightweight and portable so you can take it into the field for in situ measurements, delivered with a stand as well as a ¼-20 mount for use with tripods. When used with a Spectral Evolution spectrometer or spectroradiometer such as the PSR+, RS-3500, RS-5400, SR-6500 or RS-8800, it delivers detailed information for measurements transmittance and reflectance modes at two varying light intensity levels.

The RT sphere, similar to other field accessories, is connected to Spectral Evolution spectrometers and spectroradiometers via an industry standard SMA-905 connector. Like many other Spectral Evolution accessories, the RT sphere can be operated via a one click triggering mechanism, allowing for rapid data acquisition. It is powered by the universal accessory power supply cable for seamless integration into existing Spectral Evolution equipment.

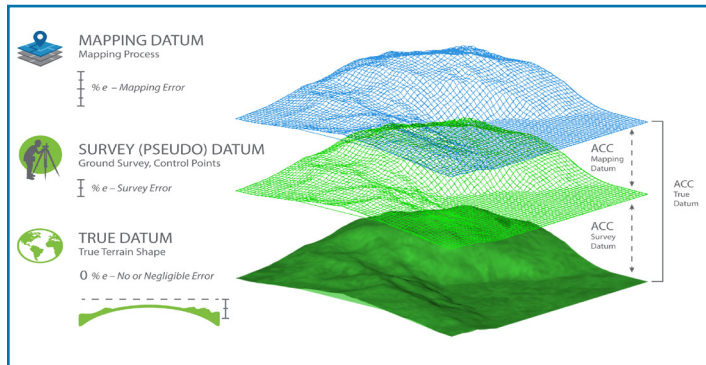
For more information on the RT sphere, visit: <https://spectralevolution.com/products/hardware/>.

Teledyne Lumenera, a Teledyne Technologies [NYSE:TDY] company, and manufacturer and developer of digital cameras for industrial and scientific imaging applications, is pleased to announce the release of its new Lt Series USB3 cameras. With robust compact enclosures and fully-locking USB3 connectors, these new cameras are built for rugged 24/7 use. Equipped with the latest rolling shutter Starvis™ CMOS sensors and global shutter Pregius™ CMOS sensors from Sony®, and ranging in resolution from 2-20 megapixels, these new cameras perform in a wide variety of imaging applications such as aerial imaging, Intelligent Traffic Systems (ITS), robotic inspection solutions, and life sciences. Teledyne Lumenera's Lt Series Cameras offer a smaller, lighter, and lower cost imaging solution and are designed specifically to meet the challenges of today's modern imaging systems that strive to provide advanced vision performance while using less power, less space, and fitting increasing-tight industry budgets.

"Even with a more compact form factor, the new Lt Series cameras offer the full set of features that the modern imaging industry demands," said Ghislain Beaupré, General Manager at Teledyne Lumenera. "These new cameras open up new opportunities for imaging system designers to incorporate full-function cameras without unnecessary performance compromises due to size."

The Teledyne Lumenera Lt Series Cameras offer proven 32 and 64-bit operating system compatibility for, Windows, Linux, Linux for embedded system platforms, and single board computers (SBCs). They are designed to deliver high dynamic range, high speed, with low read noise for both industrial and scientific imaging applications.

For more information about Teledyne Lumenera's Lt Series USB3 cameras visit <https://www.lumenera.com/products/lt-series-usb3-cameras.html>.



397 Rethinking Error Estimations in Geospatial Data: The Correct Way to Determine Product Accuracy

By Qassim Abdullah, Ph.D., PLS, CP

419 A History of Laser Scanning, Part 1: Space and Defense Applications

Adam P. Spring

This article presents the origins and evolution of midrange terrestrial laser scanning (TLS), spanning primarily from the 1950s to the time of publication. Particular attention is given to developments in hardware and software that document the physical dimensions of a scene as a point cloud. These developments include parameters for accuracy, repeatability, and resolution in the midrange—millimeter and centimeter levels when recording objects at building and landscape scales up to a kilometer away. The article is split into two parts: Part one starts with early space and defense applications, and part two (PE&RS August 2020) examines the survey applications that formed around TLS technologies in the 1990s.

431 Improved Crop Classification with Rotation Knowledge using Sentinel-1 and -2 Time Series

Sébastien Giordano, Simon Bailly, Loïc Landrieu, and Nesrine Chehata

Leveraging the recent availability of accurate, frequent, and multimodal (radar and optical) Sentinel-1 and -2 acquisitions, this paper investigates the automation of land parcel identification system (LPIS) crop type classification. Our approach allows for the automatic integration of temporal knowledge, i.e., crop rotations using existing parcel-based land cover databases and multi-modal Sentinel-1 and -2 time series. The temporal evolution of crop types was modeled with a linear-chain conditional random field, trained with time series of multi-modal (radar and optical) satellite acquisitions and associated LPIS. Our model was tested on two study areas in France ($\geq 1250 \text{ km}^2$) which show different crop types, various parcel sizes, and agricultural practices: the Seine et Marne and the Alpes de Haute-Provence classified accordingly to a fine national 25-class nomenclature.

443 Improved Depth Estimation for Occlusion Scenes Using a Light-Field Camera

Changkun Yang, Zhaoqin Liu, Kaichang Di, Changqing Hu, Yexin Wang, and Wuyang Liang

With the development of light-field imaging technology, depth estimation using light-field cameras has become a hot topic in recent years. Even through many algorithms have achieved good performance for depth estimation using light-field cameras, removing the influence of occlusion, especially multi-occlusion, is still a challenging task. The photo-consistency assumption does not hold in the presence of occlusions, which makes most depth estimation of light-field imaging unreliable. In this article, a novel method to handle complex occlusion in depth estimation of light-field imaging is proposed.

COLUMNS

405 GIS Tips & Tricks—There's More Than One Way to Import Files

409 SectorInsights.com—How Good is that Gear? Drones versus Surveyors!

411 Book Review—*Introduction to Human Geography Using ArcGIS Online*

413 Grids and Datums

This month we look at the Republic of Guinea.

ANNOUNCEMENTS

414 ASPRS Certifications

417 New ASPRS Members

Join us in welcoming our newest members to ASPRS.

418 PE&RS Call for Submissions—Urban Remote Sensing

DEPARTMENTS

394 Industry News

407 Ad Index

430 Who's Who in ASPRS

442 ASPRS Media Kit

See the Cover Description on Page 396

COVER DESCRIPTION



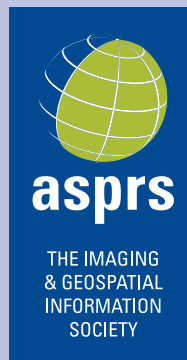
Near the western tip of the Mojave Desert and a few miles west of NASA's Armstrong Flight Research Center, fields of poppies colored the landscape a bright orange this spring. On April 14, 2020, the Operational Land Imager (OLI) on the Landsat 8 satellite acquired these images of vast blooms in the Antelope Valley California Poppy Reserve. These images were acquired when poppy flowers in the valley were thought to be at or near their peak.

The flowers bloomed after Southern California received significant rainfall in March and April 2020. This spring, Lancaster received around 10.5 inches (27 centimeters) of rain—almost 4 inches (10 centimeters) above normal. The extra rain may cause the poppies to stick around longer than usual and result in an above-average wildflower year. Park officials called this bloom an “unexpected” surprise due to the late season rains.

While many parks have restricted visitor access to the park during the COVID-19 quarantine, people can view the flowers through online livestreams, <https://www.parks.ca.gov/live/poppyreserve>. Depending on the day or even hour, the orange patches may change in appearance. The poppies open their petals during sunny periods, appearing like a large blanket over the landscape. The flowers tend to close during windy, cold periods. While the orange poppies are easy to spot in satellite imagery, the fields also contain cream cups, forget-me-nots, purple bush lupines, and yellow goldfields (a relative of the sunflower).

For more information, visit <https://landsat.visibleearth.nasa.gov/view.php?id=146642>.

NASA Earth Observatory images by Lauren Dauphin, using Landsat data from the U.S. Geological Survey. Story by Kasha Patel.



PHOTOGRAMMETRIC ENGINEERING & REMOTE SENSING

JOURNAL STAFF

Publisher ASPRS
Editor-In-Chief Alper Yilmaz
Assistant Editor Jie Shan
Assistant Director — Publications Rae Kelley
Electronic Publications Manager/Graphic Artist
Matthew Austin

Photogrammetric Engineering & Remote Sensing is the official journal of the American Society for Photogrammetry and Remote Sensing. It is devoted to the exchange of ideas and information about the applications of photogrammetry, remote sensing, and geographic information systems. The technical activities of the Society are conducted through the following Technical Divisions: Geographic Information Systems, Photogrammetric Applications, Lidar, Primary Data Acquisition, Professional Practice, and Remote Sensing Applications. Additional information on the functioning of the Technical Divisions and the Society can be found in the Yearbook issue of *PE&RS*.

Correspondence relating to all business and editorial matters pertaining to this and other Society publications should be directed to the American Society for Photogrammetry and Remote Sensing, 425 Barlow Place, Suite 210, Bethesda, Maryland 20814-2144, including inquiries, memberships, subscriptions, changes in address, manuscripts for publication, advertising, back issues, and publications. The telephone number of the Society Headquarters is 301-493-0290; the fax number is 225-408-4422; web address is www.asprs.org.

PE&RS. *PE&RS* (ISSN0099-1112) is published monthly by the American Society for Photogrammetry and Remote Sensing, 425 Barlow Place, Suite 210, Bethesda, Maryland 20814-2144. Periodicals postage paid at Bethesda, Maryland and at additional mailing offices.

SUBSCRIPTION. For the 2020 subscription year, ASPRS is offering two options to our *PE&RS* subscribers — an e-Subscription and the print edition. E-subscribers can plus-up their subscriptions with printed copies for a small additional charge. Print and Electronic subscriptions are on a calendar-year basis that runs from January through December. We recommend that customers who choose both e-Subscription and print (e-Subscription + Print) renew on a calendar-year basis.

The rate of the e-Subscription (digital) Site License Only for USA and Non-USA is \$1000.00 USD. e-Subscription (digital) Site License Only for Canada* is \$1049.00 USD. e-Subscription (digital) Plus Print for USA is \$1365.00 USD. e-Subscription (digital) Plus Print for Canada* is \$1424.00 USD. e-Subscription (digital) Plus Print for Non-USA is \$1395.00 USD. Printed-Subscription Only for USA is \$1065.00 USD. Printed-Subscription Only for Canada* is \$1124.00 USD. Printed-Subscription Only for Non-USA is \$1195.00 USD. *Note: e-Subscription/Printed-Subscription Only/e-Subscription Plus Print for Canada include 5% of the total amount for Canada's Goods and Services Tax (GST #135123065). **PLEASE NOTE: All Subscription Agencies receive a 20.00 USD discount.**

POSTMASTER. Send address changes to *PE&RS*, ASPRS Headquarters, 425 Barlow Place, Suite 210, Bethesda, Maryland 20814-2144. CDN CPM #40020812

MEMBERSHIP. Membership is open to any person actively engaged in the practice of photogrammetry, photointerpretation, remote sensing and geographic information systems; or who by means of education or profession is interested in the application or development of these arts and sciences. Membership is for one year, with renewal based on the anniversary date of the month joined. Membership Dues include a 12-month electronic subscription to *PE&RS*. Or you can receive the print copy of *PE&RS* Journal which is available to all member types for an additional fee of \$60.00 USD for shipping USA, \$65.00 USD for Canada, or \$75.00 USD for international shipping. Dues for ASPRS Members outside of the U.S. will now be the same as for members residing in the U.S. Annual dues for Regular members (Active Member) is \$150.00 USD; for Student members \$50.00 USD for USA and Canada \$58.00 USD; \$60.00 USD for Other Foreign members. A tax of 5% for Canada's Goods and Service Tax (GST #135123065) is applied to all members residing in Canada.

COPYRIGHT 2020. Copyright by the American Society for Photogrammetry and Remote Sensing. Reproduction of this issue or any part thereof (except short quotations for use in preparing technical and scientific papers) may be made only after obtaining the specific approval of the Managing Editor. The Society is not responsible for any statements made or opinions expressed in technical papers, advertisements, or other portions of this publication. Printed in the United States of America.

PERMISSION TO PHOTOCOPY. The appearance of the code at the bottom of the first page of an article in this journal indicates the copyright owner's consent that copies of the article may be made for personal or internal use or for the personal or internal use of specific clients. This consent is given on the condition, however, that the copier pay the stated per copy fee of 3.00 USD through the Copyright Clearance Center, Inc., 222 Rosewood Drive, Danvers, Massachusetts 01923, for copying beyond that permitted by Sections 107 or 108 of the U.S. Copyright Law. This consent does not extend to other kinds of copying, such as copying for general distribution, for advertising or promotional purposes, for creating new collective works, or for resale.

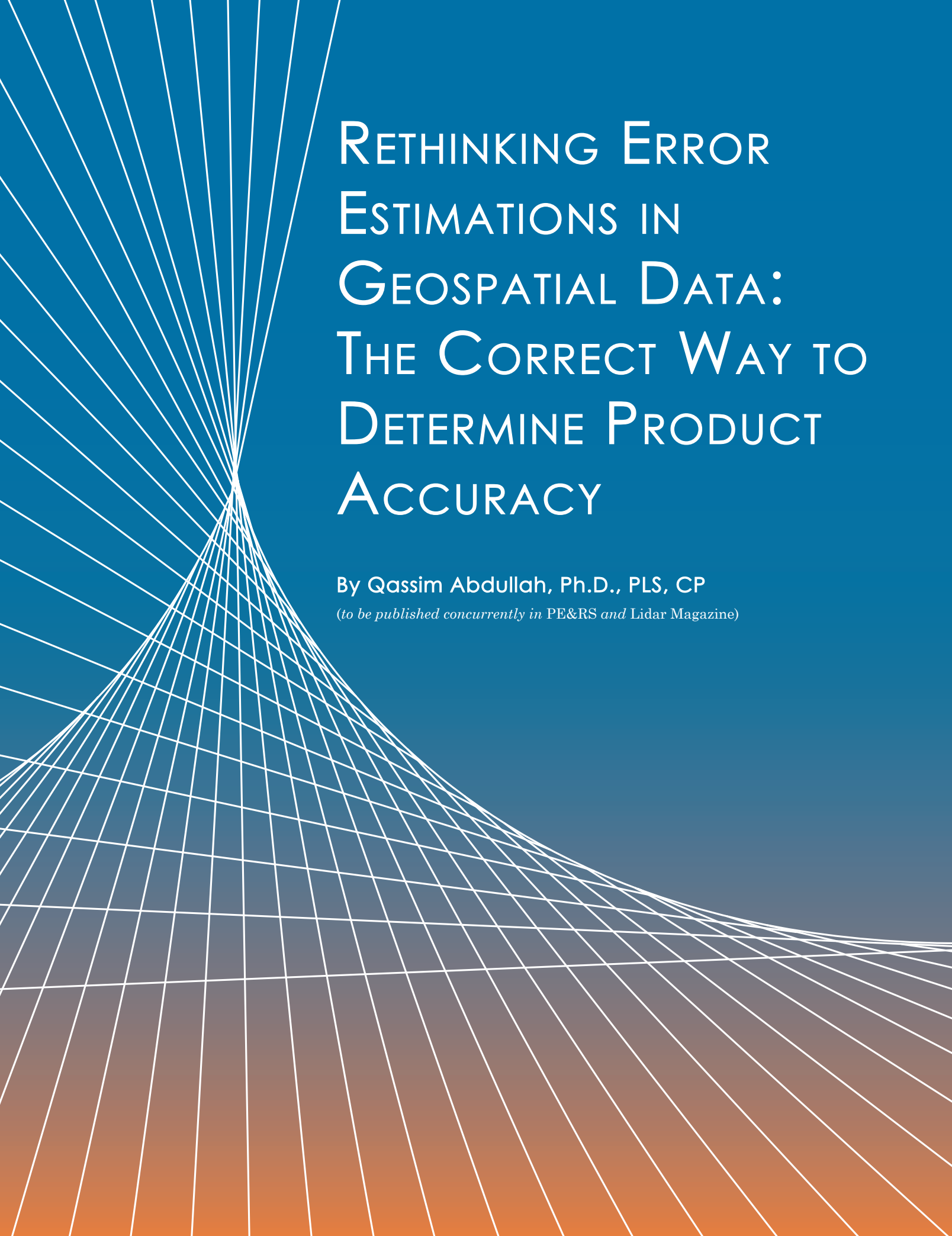
Be a part of ASPRS Social Media:

 facebook.com/ASPRS.org

 linkedin.com/groups/2745128/profile

 twitter.com/ASPRSorg

 youtube.com/user/ASPRS

The background features a complex geometric pattern of white lines. These lines originate from a single point on the left side and fan out towards the right, creating a sense of depth and perspective. The lines are thin and white, set against a background that transitions from a deep blue at the top to a warm orange at the bottom. The overall effect is clean, modern, and technical.

RETHINKING ERROR ESTIMATIONS IN GEOSPATIAL DATA: THE CORRECT WAY TO DETERMINE PRODUCT ACCURACY

By Qassim Abdullah, Ph.D., PLS, CP

(to be published concurrently in PE&RS and Lidar Magazine)

Surveying and mapping technologies have advanced tremendously over the last century, resulting in improved product accuracy. Yet some antiquated practices and processes continue, as if they are frozen in time. This article will focus on an outdated practice that needs to be addressed: the way we evaluate the positional accuracy of geospatial products.

Before detailing this problem and introducing the correct approach, we should establish a basic understanding of how to determine and report product accuracy, geometric datum, and what that datum represents. To understand the datum, one needs to know how we deal with the shape, or figure, of the Earth.

FIGURES OF THE EARTH

The physical surface of the Earth is the shape we attempt to model through our mapping or surveying practices. However, because of irregularities on the Earth's surface and the lack of a comprehensively surveyed model of that surface, several geometrically defined shapes are employed in our surveying and mapping techniques to approximate the Earth's surface to determine specific geographic locations (Figure 1). These geographic locations must be referenced by a well-known system called a "datum."

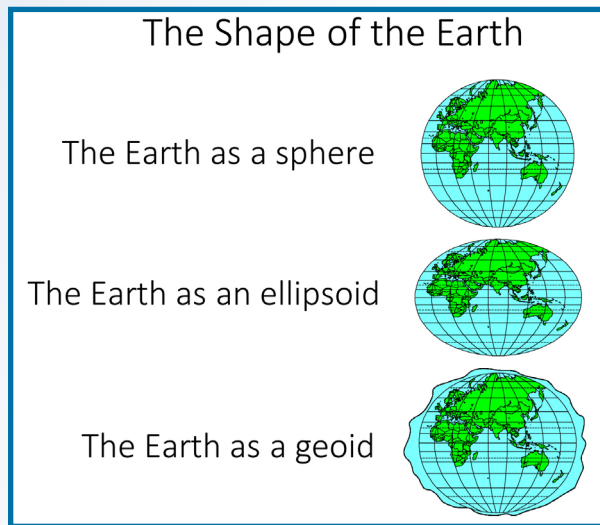


Figure 1: Shapes of the Earth (Courtesy of Esri documentations).

Photogrammetric Engineering & Remote Sensing
Vol. 86, No. 7, July 2020, pp. 397–403.

0099-1112/20/397–403

© 2020 American Society for Photogrammetry
and Remote Sensing

doi: 10.14358/PERS.86.7.397

Earth as an Ellipsoid

An ellipsoid surface is obtained by deforming a sphere by means of directional scaling, so it is the best shape to use to approximate the Earth. The term datum is nothing but an ellipsoid with defined axes, curvature, a known origin in space and axes rotation. Wikipedia defines the Earth ellipsoid as “a mathematical figure approximating the Earth's form, used as a reference frame for computations in geodesy, astronomy and the geosciences.” Datum origin can be positioned at any place in space. The origin of the NAD27 datum is at the survey marker of the Meades Ranch Triangulation Station in Osborne County, Kansas. Geocentric datum is a datum with its origin positioned at the mass center of the Earth. Examples of geocentric datums are the NAD83, ITRF and WGS84—all of which are based on the GRS80 ellipsoid. All surveying and mapping activities, including GNSS surveying, determine how far a position on the Earth's surface is from the surface of a referenced ellipsoid or geoid.

Earth as a Geoid

A geoid represents the equipotential surface of the Earth's gravity and comes very close to mean sea level. Wikipedia defines a geoid as “the shape that the ocean surface would take under the influence of the gravity and rotation of the Earth alone, if other influences such as winds and tides were absent.” Surveyors traditionally present their height measurements in reference to the geoid, i.e. how far that position is above or below the geoid surface. Since the geoid surface is shaped by the same gravitational force that causes water to flow downhill, people like to survey elevations by referencing the geoid because those elevations or slope directions align with that natural water flow. Conversely, ellipsoidal heights measuring up or down slopes may not match that water flow direction.

The True Physical Shape of Earth

The terrain around us is irregular and does not coincide with either geoid or ellipsoid surfaces. Our surveying and mapping activities are solely conducted to represent the physical figure of the Earth on a map or within a geospatial database as it is referenced to the datum.

SURVEYING TO REPRESENT THE TRUE DATUM

When we conduct field surveying, we are trying to determine terrain positions and shapes in reference to a specific geodetic datum. According to the U.S. National Geodetic Survey (NGS), a geodetic datum is defined as “an abstract coordinate system with a reference surface (such as sea level, as a vertical datum) that serves to provide known locations to begin surveys and create maps.” Because our surveying techniques, and therefore our mapping techniques, are not perfect, our surveying results are approximate positions that put us close to the true, da-

tum-derived positions (Figure 2). When we use an inaccurately surveyed network to control another process such as aerial triangulation, in reality we are fitting the aerial triangulation solution to an observed datum. The degree of approximation depends on the surveying technique or technology employed in that survey. The Real-Time Kinematic (RTK) field surveying technique can produce positions that are accurate to 2cm horizontally and perhaps 3cm vertically. The differential leveling technique used to determine height can produce elevations that are accurate to the sub-centimeter. The lesson to learn here is that our surveying techniques, no matter how accurate, do not represent the true datum—but they can get us close to it.

Surveying and Survey Datum

When we task surveyors to survey the ground control network in reference to a certain datum, they can only determine the positions of the control network to that datum as close as the surveying techniques allow. In other words, the coordinates that are being used to control the mapping process represent an observed or survey datum that represents a pseudo datum but not the original intended or true datum (Figure 2). For example, if we are trying to determine point coordinates in NAD83(2011), the surveyed coordinates used in aerial triangulation or lidar calibration represent a datum that is close to NAD83(2011) but not exactly NAD83(2011) due to the inaccuracy in our surveying techniques. That inaccurate survey represents a survey datum. Besides the inaccuracy in the surveying techniques, another layer of errors (i.e. distortion) is added to the surveyed coordinates when we convert geographic positions (in latitude and longitude) to projected coordinates or grid coordinates, such as state plane coordinates systems.

Mapping To The Mapping Datum

Any mapping process we conduct today inherits two modeling errors that influence product accuracy. The first modeling error is caused by the inaccuracy of the internal geometric determination during the aerial triangulation, or the boresight calibration in the case of lidar processing. The second modeling error is introduced by the auxiliary systems, such as GPS and IMU, and has inherent errors caused by the survey datum. Therefore, when we use mapping products to extract location information, we are determining these locations in reference to the survey datum and not the original intended datum. The point coordinates for NAD83(2011) are determined not according to the survey datum of the ground control network but through a new reality of mapping datum. The mapping datum inherits the errors of the survey datum, which were caused by the inaccuracy of our surveying techniques and the errors caused by our mapping processes and techniques (Figure 2).

Drilling to the True Datum

To reference the accuracy of determining a mapped object location within a mapping product to the original intended datum like NAD83(2011), we need to examine the layers of errors that were introduced during the ground surveying and mapping processes (Figure 2).

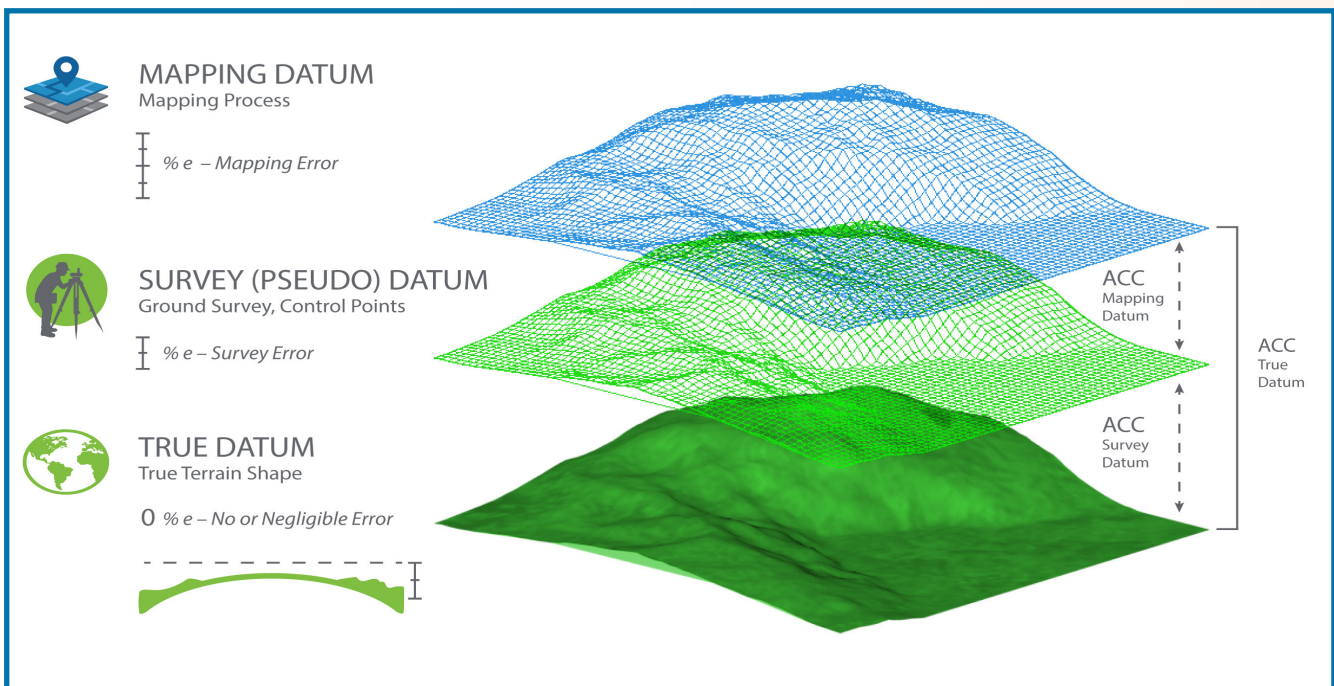


Figure 2: Datums and error propagation in geospatial data.

PRODUCT ACCURACY COMPUTATION

Currently, users of geospatial data express product accuracy based on the agreement or disagreement of the tested product per the surveyed checkpoints, ignoring checkpoint errors that have resulted from inaccurate surveying techniques. In other words, users consider the surveyed checkpoints to be free of error. The following section details how errors are propagated into the mapping product when we are trying to determine the location of a ground point “A”. Let us introduce the following terms:

$ACC_{SurveyDatum}$ equals the accuracy in determining the survey datum, generated when realizing the intended or true datum through surveying techniques. In other words, it represents the errors in the surveyed checkpoints. Due to this inaccuracy, the point will be located at location A'' (Figure 3).

$ACC_{MappingDatum}$ equals the accuracy of determining the mapping datum, or the errors introduced during the mapping process, in reference to the already inaccurate survey datum represented by the surveyed checkpoints. In other words, it is the fit of the aerial triangulation (for imagery) or the boresight/calibration (for lidar) to the surveyed ground control points represented as the survey datum. This accuracy is measured using the surveyed checkpoints during the product accuracy verification process. Due to this inaccuracy, the point will be located at location A''' (Figure 3).

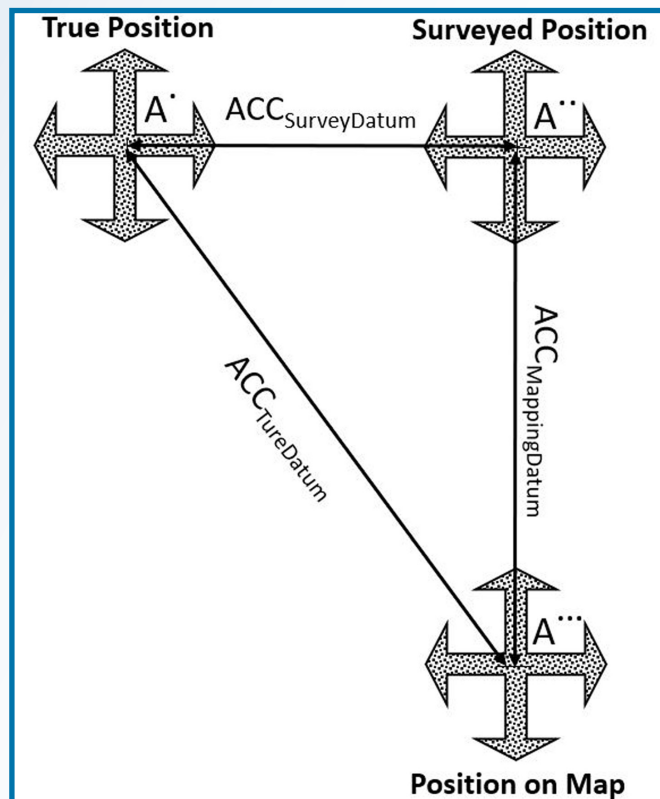


Figure 3: Influence of error propagation on point location accuracy.

$ACC_{TrueDatum}$ equals the accuracy of the mapping product in reference to the true datum, as in NAD83(2011). The point location A' (Figure 3) is considered the most accurate location determined in reference to the true datum.

Using the above definitions, the correct product accuracy should be modeled using error propagation principles according to the following formula:

$$ACC_{TrueDatum} = \sqrt{ACC_{MappingDatum}^2 + ACC_{SurveyDatum}^2} \quad 1$$

However, according to our current practices, product accuracy is computed according to the following formula, ignoring errors in the surveying techniques:

$$ACC_{TrueDatum} = ACC_{MappingDatum} \quad 2$$

Practical Method of Computing Accuracy Components

As we are dealing with three-dimensional error components, we would need to employ vector algebra to accurately compute the cumulative error.

Computing Horizontal Accuracy

To compute the horizontal accuracy for a two-dimensional map, as with orthorectified imagery, we will ignore the error component of the height survey. In other words, we will use the error component from easting and northing only. We will also assume that the accuracy of determining the X coordinates (or easting) is equal to the accuracy of determining the Y coordinates (or northing). Using error propagation principles and Euclidean vector in Figures 3 and 4, we can derive the following values for product horizontal accuracy:

$$AccX_{TrueDatum} = \sqrt{AccX_{MappingDatum}^2 + AccX_{SurveyDatum}^2} \quad 3$$

$$AccY_{TrueDatum} = \sqrt{AccY_{MappingDatum}^2 + AccY_{SurveyDatum}^2} \quad 4$$

$$AccXY_{TrueDatum} = \sqrt{AccX_{TrueDatum}^2 + AccY_{TrueDatum}^2} \quad 5$$

As an example, when modeling horizontal product accuracy according to the above formulas, let us assume the following:

- We are evaluating the horizontal accuracy for orthoimagery using independent checkpoints.
- The control survey report states that the survey for the checkpoints, which was conducted using RTK techniques, resulted in accuracy of $RMSE_{XorY}$ equal to 2cm.
- When the checkpoints were used to verify the horizontal accuracy of the orthoimagery, it resulted in an accuracy of $RMSE_{XorY}$ equal to 3cm.

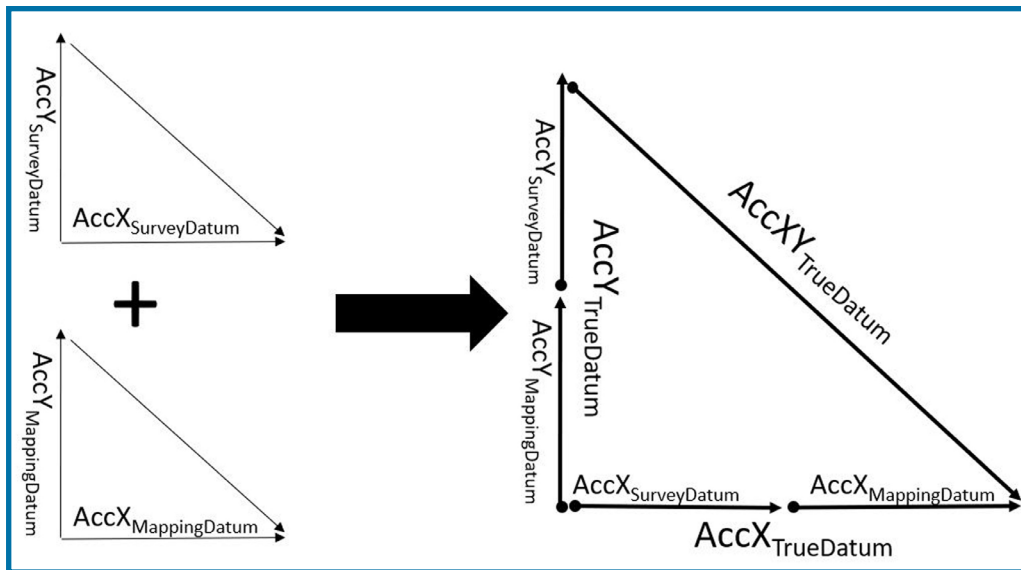


Figure 4: Vector representations of error components.

Solution

Using equations 3, 4 and 5:

$$\text{AccXTrueDatum} = \sqrt{\text{AccXMappingDatum}^2 + \text{AccXSurveyDatum}^2} = \sqrt{3^2 + 2^2} = 3.61\text{cm}$$

$$\text{AccYTrueDatum} = \sqrt{\text{AccYMappingDatum}^2 + \text{AccYSurveyDatum}^2} = \sqrt{3^2 + 2^2} = 3.61\text{cm}$$

$$\text{AccXYTrueDatum} = \sqrt{\text{AccXTrueDatum}^2 + \text{AccYTrueDatum}^2} = \sqrt{3.61\text{cm}^2 + 3.61\text{cm}^2} = 5.1\text{cm}$$

The value of 5.1cm is the true accuracy of the product versus the following value of 4.24cm used commonly today that ignores the errors introduced during the ground surveying process:

$$\text{AccXYTrueDatum} = \sqrt{\text{AccXMappingDatum}^2 + \text{AccYMappingDatum}^2} = \sqrt{3\text{cm}^2 + 3\text{cm}^2} = 4.24\text{cm}$$

Computing Vertical Accuracy

Similarly, for vertical accuracy determination of elevation data derived from lidar or photogrammetric methods, we need to consider the error in the surveyed elevation as an important component. Using error proration principles and Euclidean vector of Figure 5, we can derive the following value for vertical product accuracy:

$$\text{AccZTrueDatum} = \sqrt{\text{AccZMappingDatum}^2 + \text{AccZSurveyDatum}^2} \quad 6$$

As an example, when modeling vertical product accuracy according to the above formulas, let us assume the following:

- That we are evaluating the vertical accuracy for a mobile lidar dataset using independent checkpoints.
- The control survey report states that the survey of the checkpoints, which was conducted using RTK techniques, resulted in an accuracy of RMSEZ equal to 3cm.
- When the checkpoints were used to verify the vertical accuracy of the lidar data, it resulted in an accuracy of RMSEZ equal to 1cm.

Solution

Using Equation 6:

$$\text{AccZTrueDatum} = \sqrt{\text{AccZMappingDatum}^2 + \text{AccZSurveyDatum}^2} = \sqrt{1^2 + 3^2} = 3.16\text{cm}$$

The value of 3.16cm is the true vertical accuracy of the lidar dataset versus the value of 1cm, derived by the mapping technique used commonly that ignores the errors introduced during the ground surveying process.

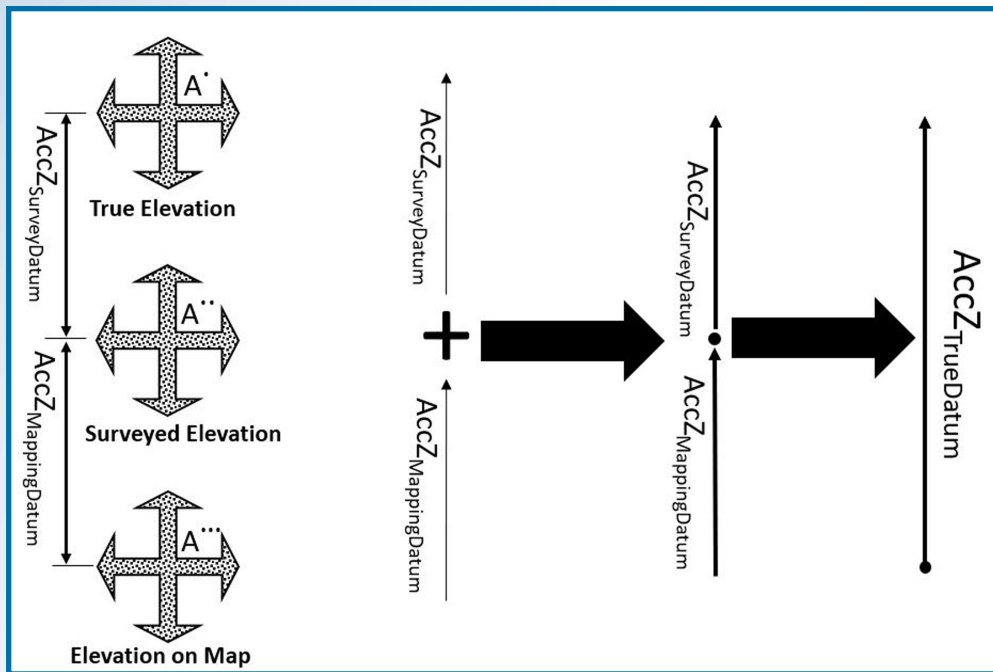


Figure 5: Influence of error propagation on point elevation accuracy.

REMARKS AND RECOMMENDATIONS

The propagation of errors through the mapping process is a well-known and well-practiced science in surveying and mapping. However, due to the gradual evolution in mapping technologies and mapping practices over decades of advancements, users have become less sensitive to the fact that surveying techniques are not perfect. Such insensitivity is caused by the following simple facts:

- 1) The early days of mapping products were highly inaccurate, and users ignored the errors caused by inadequate surveying techniques. Earlier in the days of digital mapping, the U.S. Geological Survey (USGS) introduced the Digital Orthophoto Quadrangle (DOQ). DOQs produced by the USGS cover an area measuring 7.5-minutes longitude by 7.5-minutes latitude (the same area covered by a USGS 1:24,000-scale topographic map, also known as a 7.5-minute quadrangle). The USGS also introduced second product that is higher in resolution and accuracy than the DOQ called the Digital Orthophoto Quarter Quadrangle (DOQQ), with a scale of 1:12,000 in a format of 3.75-minutes by 3.75-minutes.¹ The horizontal accuracy of the DOQQ at the time, according to the National Map Accuracy Standard (NMAS), was equal to 10.1 meter (or 33.3 ft), while our surveying techniques resulted in accuracy to the sub-decimeter level. Surveyors and mappers at the time were aware of this and intentionally ignored errors caused by the surveying techniques when deriving the accuracy of a mapping products, such as what a 5cm to 10cm difference was going to add to

the 10-meter coarse accuracy of a product. However, product accuracy improved gradually over time while a new generation of surveyors and mappers were likely still trained to ignore the errors in surveying techniques. Over time, the entire mapping industry became numb to this fact. Today, some mapping products from terrestrial lidar, mobile mapping lidar, UAS-based lidar, and some time photogrammetric products from low altitude manned and unmanned aircraft, if stringent production workflow is followed, are accurate to sub-centimeter level. Such improved accuracy presents a new challenge when it comes to people with little or no photogrammetric or surveying education or experience. The new UAS-operator-turned-mapper community is at the top of this list. Oftentimes people are claiming sub-centimeter horizontal and vertical accuracy from UAS products. This claim has merit until you ask the mapper about the technique used in surveying the ground control points for aerial triangulation or lidar calibration or for the independent surveyed checkpoints to verify this claim. In most cases, these users either were not aware of what technique that was used or, if they were aware of it, it was an RTK survey. As mentioned earlier, RTK survey results in 2cm to 3cm accuracy. The concern here is how do you obtain a sub-centimeter accuracy from a process that was controlled by ground control surveyed to an accuracy of 2-3cm? This question promptly ends that conversation. One may ask here, how the aerial triangulation or lidar boresight/calibration results in sub-centimeter accuracy while the

ground controls used during these processes are only accurate to 2cm. The answer is simple. In aerial triangulation or in lidar boresight/calibration there many variables that are adjusted during the process. These variables—including exterior orientation parameters, camera interior parameters, timing, etc.—are considered adjustable observations with error budget (or weight) built in, so they are tuned and adjusted during the process. The nature of the mathematical modeling and the least squares we perform during these processes allow errors in a parameter to change based on the constraint of that parameter. For example, over constraining the height of a ground control point in the solution may push the error in the control to the adjusted focal length of the camera. The same thing is valid for easting and northing, as it can be absorbed by the exterior orientation of the imagery or the image measurements of the tie/pass points. That is how the least squares adjustment works—it does not remove errors but minimizes their effect by redistributing those errors within the adjusted block.

The previously described reality is forcing us to reconsider original practices from softcopy or digital photogrammetry in the 1980s, when the error of ground survey was ignored while computing product accuracy.

- 2) The lack of photogrammetric and surveying knowledge with many data producers, especially the new UAS-operator-turned-mapper community, leads them to believe that the residuals in the resulted aerial triangulation or the lidar bore-sighting/calibration or the fit to the ground controls represent their final product accuracy. They are not aware that the fit of aerial triangulation or the lidar bore-sighting/calibration solutions to the surveyed control or checkpoints does not directly represent the product accuracy because it is referenced to the survey datum, which resulted from the inaccuracy in surveying techniques and not to the intended true datum and coordinates system. Without incorporating the discrepancies between the true datum and the survey datum in computing final product accuracy, product accuracy will be falsely expressed.
- 3) Creators of mapping standards fell into the same trap that early mappers fell into by ignoring the survey error component in calculating product accuracy. Users of these standards followed those guides. By ignoring the error component from the surveying technique when estimating product accuracy, these standards contributed to the problem and did not offer users with a solution.

Based on the previous discussions, the mapping community urgently needs to embrace the following corrective practices:

- 1) The mapping community needs to start incorporating the accuracy of field surveying ground control points or checkpoints into their product accuracy computations when reporting final product accuracy as illustrated in this article. This will require negotiating ground control accuracy requirements with surveyors prior to conducting surveys. Users will also need to require surveyors to deliver complete survey reports highlighting the accuracy of the survey. They should consult the ASPRS Positional Accuracy Standards for Digital Geospatial Data² to understand the required accuracy of ground control that is needed to meet specific product accuracy.
- 2) Similar actions need to be considered in the next version of the ASPRS Positional Accuracy Standards of Digital Geospatial Data. These standards need to be amended to introduce the correct way to compute product accuracy and to provide practical examples like the ones outlined in this article.
- 3) Private and public agencies need to mandate that future product accuracy should be expressed according to the new concept introduced in this article. By not doing so, the stated product accuracy according to the current practices will be incorrect and misleading.

AUTHOR

Dr. Abdullah is Vice President and Chief Scientist at Woolpert, Inc. He is also adjunct professor at Penn State and the University of Maryland Baltimore County. Dr. Abdullah is ASPRS fellow and the recipient of the ASPRS Life Time Achievement Award and the Fairchild Photogrammetric Award.

1 https://en.wikipedia.org/wiki/Digital_orthophoto_quadrangle.

2 <https://www.asprs.org/news-resources/asprs-positional-accuracy-standards-for-digital-geospatial-data>.

ASPRS BOOKSTORE

visit asprs.org

available at
amazon

Digital Elevation Model Technologies & Applications, 3rd Ed

Co-Editors: David F. Maune, PhD, CP, CFM, PSM, PS, GS, SP and Amar Nayegandhi, CP, CMS-Remote Sensing
List Price: \$100 | **ASPRS Members:** \$80
ASPRS Student Members: \$50[†]
Also available for Amazon Kindle
Amazon Kindle Price:** \$85

Landsat's Enduring Legacy: Pioneering Global Land Observations From Space

Landsat Legacy Project Team
ISBN: ISBN 1-57083-101-7 · Hardcover · 586 pages · 2017 · Stock #4958
List Price: \$95 | **ASPRS Members:** \$65
Student Members: \$60
Amazon Price*: \$100

Manual of Airborne Topographic Lidar

Editor: Michael S. Renslow
ISBN: 1-57083-097-5 · Hardcover · 528 pages · 2012 · Stock #4587
List Price: \$150 | **ASPRS Members:** \$95
Student Members: \$75
Amazon Price (hardcover)*: \$135
Also available for Amazon Kindle
Amazon Kindle Price:** \$110

Manual of Photogrammetry, Sixth Edition

Editor: J. Chris McGlone
ISBN: 1-57083-099-1 · Hardcover · 1372 pages · 2013 · Stock #4737
List Price: \$175 | **ASPRS Members:** \$125
Student Members: \$98
Amazon Price*: \$175

Glossary of the Mapping Sciences

Co-published by ASPRS, ACSM and ASCE
ISBN: 1-57083-011-8
563 pp · Paperback · 1994 · Stock #5021
List Price: \$50 | **ASPRS Members:** \$35
Student Members: \$25 | **Amazon Price*:** \$50

Hyperspectral Remote Sensing for Forestry

Paul Treitz, Valerie Thomas, Pablo J. Zarco-Tejada, Peng Gong, and Paul J. Curran
ISBN: 1-57083-093-2
107 pp · Softcover · 2010 · Stock #4584
List Price: \$26 | **ASPRS Members:** \$21
Student Member: \$21 | **Amazon Price*:** \$26

Manual of Geographic Information Systems

Editor: Marguerite Madden, PhD
Foreword: Jack Dangermond, Esri
ISBN: 1-57083-086-X · Hardcover · 1352 pages + DVD · July 2009 · Stock #4650
List Price: \$53 | **ASPRS Members:** \$40
Student Members: \$40
Amazon Price*: \$55

Meeting Environmental Challenges with Remote Sensing Imagery

Editors: Rebecca Dodge & Russ Congalton
Published by American Geosciences Institute; Publishing Partners: AmericaView, USGS Land Remote Sensing Program, ASPRS
ISBN: 978-0-922152-94-0 · 82 pp · Softcover · 2013 · Stock #4589
List Price: \$7.50 | **ASPRS Members:** \$6
Bulk Orders (3 or more copies): \$4.50 each
Amazon Price*: \$9.95

MANUAL OF REMOTE SENSING, 3RD EDITION (A SERIES)

Earth Observing Platforms & Sensors

Volume 1.1
Volume Editor: Mark Jackson
ISBN: 1-57083-089-4
550 pp · Hardcover · 2009 · Stock #4582
List Price: \$95 | **ASPRS Members:** \$75
Student Members: \$55 | **Amazon Price*:** \$95

Remote Sensing of Human Settlements

Volume 5
Editor-in-Chief: Andrew B. Rencz
Volume Editors: Merrill K. Ridd & James D. Hipple
ISBN: 1-57083-077-0
747+ pp · Hardcover · 2005 · Stock # 4576
List Price: \$99 | **ASPRS Members:** \$80
Student Members: \$60
Amazon Price*: \$69.99

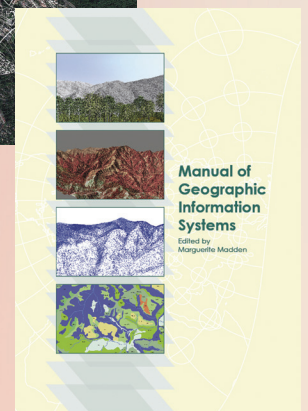
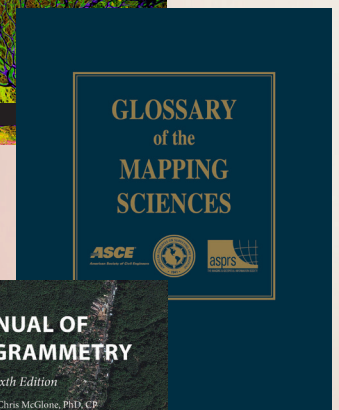
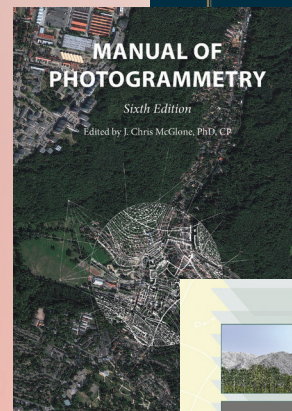
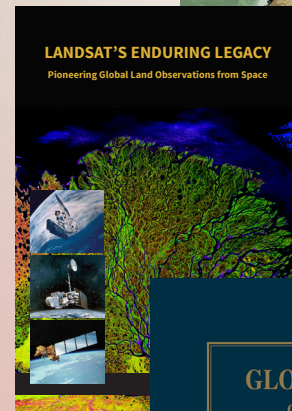
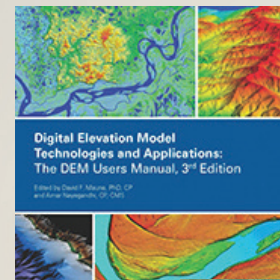
Remote Sensing of the Marine Environment

Volume 6
Editor-in-Chief: Andrew B. Rencz
Volume Editor: James F.R. Gower
ISBN: 1-57083-080-0 · 360 pp · Hardcover · 2006 · Stock # 4578
List Price: \$95 | **ASPRS Members:** \$75
Student Members: \$50 | **Amazon Price*:** \$95

*Member discounts are not available when ordering directly from Amazon.

**Member discounts are not available on Amazon Kindle e-books,

[†]Students must order via the ASPRS Bookstore & a copy of your valid student ID must be submitted to be eligible for student pricing.



GIS Tips & Tricks

There's More Than One Way to Import Files

It is strange how some GIS tasks are so common that we almost forget how to do them. Just yesterday, I needed to map a USGS Water Level Gauge and the only spatial data available was a geographic coordinate given in degrees (DD), minutes (MM), and fractional seconds (SS.xx). Of course, most GIS software packages like to have geographic coordinates expressed as Decimal Degrees (DD.xxxxxx). One of the quickest ways to convert the DMS or DD coordinates is to use Excel and two simple formulas.

To convert DMS coordinates to DD (north of the Equator and west of the Prime Meridian):

$$\text{Longitude} = -1 * ((DD) + (MM/60) + (SS.xx/3600)) \text{ and}$$

$$\text{Latitude} = ((DD) + (MM/60) + (SS.xx/3600)) \text{ where DD = degrees, MM= minutes, and SS.xx= seconds}$$

Using these formulas in an Excel spreadsheet and then importing the spreadsheet into your GIS software is a surefire, quick workflow to map a few points. However, some GIS software packages favor ASCII text files (.TXT) or comma delimited files (.CSV), and this will just add another step in the workflow. Use the Excel “save as” dropdown and select the file type needed for your software.

When you only have one or a few points to convert, manually entering the data into Excel and using the formulas is a quick workflow, or if the data are already in a projected coordinate system (Northings and Eastings) but you have several hundred points. Often, we receive survey data for lidar ground check points, and the Latitude/Longitude (or Northing and Easting) data are transmitted as an ASCII .TXT file or a .CSV file and you need to do some data processing before your software can ingest the data. The simple solution is to Import the file into Excel for processing. In the examples below, we use camera exterior orientation positions for an aerial triangulation project, but the process would be the same if importing survey data.

Here is a familiar icon from the Microsoft Excel ribbon, the Import from Text/CSV. I'm willing to bet that everyone reading this column, has at one time or another, used Microsoft Excel to read-in a comma delimited file (CSV) or some delimited or free-form ASCII file containing XY and Height coordinates. However, sometimes with software upgrades, old familiar workflows,



Chad Lopez, CMS and Al Karlin, Ph.D,
CMS-L, GISP

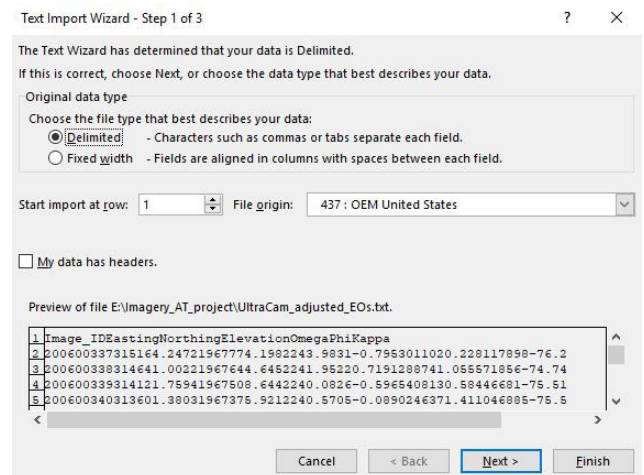
some that you have used hundreds (if not thousands of time) need to be altered. When Microsoft updated from the old “Office Suite” to the new “Office 365” several people around this office noticed that they were not seeing the usual import options that they were accustomed to seeing in Excel.

So, here are two quick tips with alternative “new” workflow for Office 365 users to import CSV and TXT files.

To import a CSV file:

- In a blank Excel spreadsheet, go to File -> Open and navigate to your text/CSV file and select it.
- The Text Import Wizard window should then open with options to choose Fixed Width or Delimited depending on how your data are formatted, and if you choose Delimited you can then choose what the delimiter is.

Step 1—First step in Import Wizard process where you can choose delimited or fixed width to separate fields.



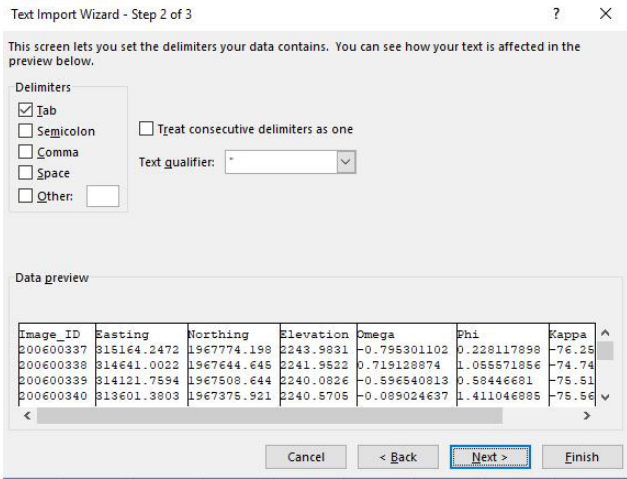
Step 2—2nd step (in this case after choosing “delimited” in the 1st step) where you can choose the delimiter type.

Photogrammetric Engineering & Remote Sensing
Vol. 86, No. 7, July 2020, pp. 405–407.

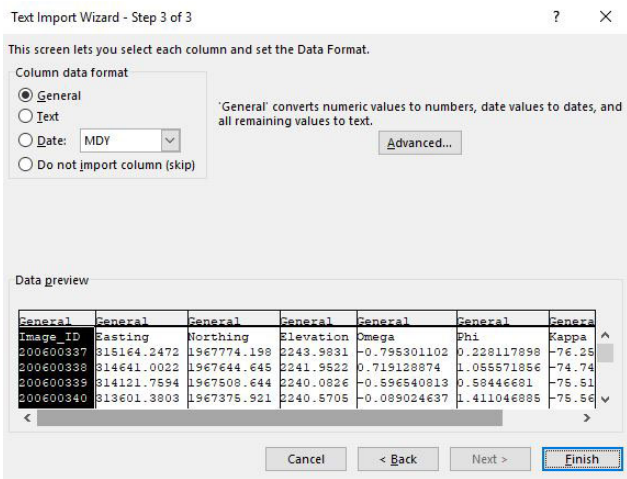
0099-1112/20/405–407

© 2020 American Society for Photogrammetry
and Remote Sensing

doi: 10.14358/PERS.86.7.405



Step 3—3rd and final step where you can format the data in your columns if choose so.



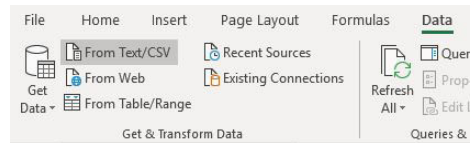
Imported spreadsheet screenshot—Final result of the import in Excel spreadsheet format. Then of course you can save it to an Excel spreadsheet file, a CSV file, etc.

	A	B	C	D	E	F	G
1	Image_ID	Easting	Northing	Elevation	Omega	Phi	Kappa
2	200600337	315164.2472	1967774.198	2243.9831	-0.795301102	0.228117898	-76.25793466
3	200600338	314641.0022	1967644.645	2241.9522	0.719128874	1.055571856	-74.7420526
4	200600339	314121.7594	1967508.644	2240.0826	-0.596540813	0.58446681	-75.51595552
5	200600340	313601.3803	1967375.921	2240.5705	-0.089024637	1.411046885	-75.5685844
6	200600341	313080.5364	1967240.925	2240.9975	0.629328601	0.724604364	-75.2359192
7	200600342	312560.0878	1967106.504	2236.2848	-0.269891603	0.435735098	-75.89084724
8	200600343	312037.3114	1966977.196	2234.5501	-0.181593927	1.265134904	-75.62713519
9	200600344	311516.5065	1966847.207	2237.1906	-0.201691115	1.046327334	-75.15044873
10	200600345	310996.0056	1966713.415	2236.202	-0.504833185	0.455062103	-75.41867367

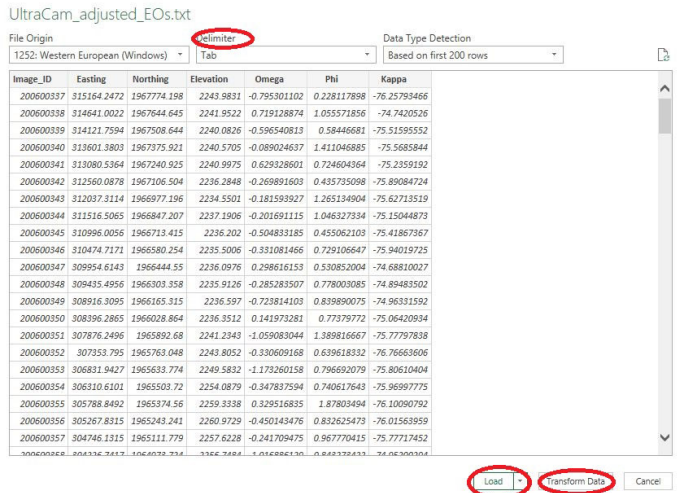
The second alternative to import a TXT (or CSV) file:

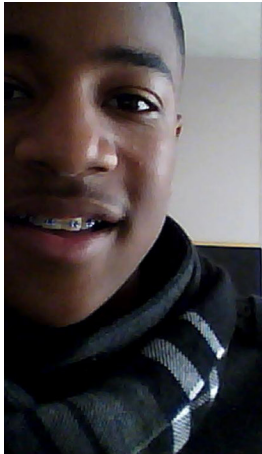
- Open a blank Excel file.

From Text/CSV button in the Get & Transform Data ribbon under Data in Excel, choose the “From Text/CSV”.



This will load the data and open the dialog boxes:





Too young to drive the car? Perhaps!

But not too young to be curious about geospatial sciences.

The ASPRS Foundation was established to advance the understanding and use of spatial data for the betterment of humankind. The Foundation provides grants, scholarships, loans and other forms of aid to individuals or organizations pursuing knowledge of imaging and geospatial information science and technology, and their applications across the scientific, governmental, and commercial sectors.

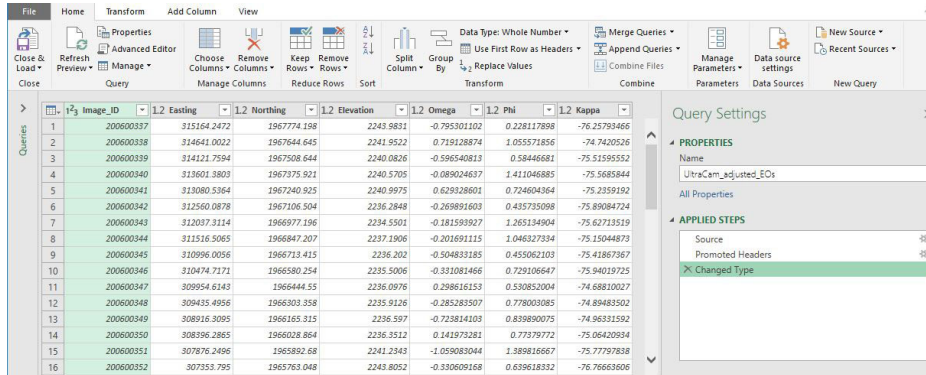
Support the Foundation, because when he is ready so will we.

asprsfoundation.org/donate



Import window after loading the text or csv file. There are different delimiter options in the Delimiter drop down menu. Usually selecting the correct Delimiter is all that is needed to complete the import process.

If you click the Transform Data in the first import window it opens the Transform Data window. This window has numerous options for formatting such as adding and removing columns, sorting, and transposing data.



When done, click the Load button in the first import window and then your text/csv file is now in spreadsheet form and you can save to an Excel file or other format.

	A	B	C	D	E	F	G
1	Image_ID	Easting	Northing	Elevation	Omega	Phi	Kappa
2	200600337	315164.2472	1967774.198	2243.9831	-0.795301102	0.228117898	-76.25793466
3	200600338	314641.0022	1967644.645	2241.9522	0.719128874	1.055571856	-74.7420526
4	200600339	314121.7594	1967508.644	2240.0826	-0.596540813	0.58446681	-75.51595552
5	200600340	313601.3803	1967375.921	2240.5705	-0.089024637	1.411046885	-75.5685844
6	200600341	313080.5364	1967240.925	2240.9975	0.629328601	0.724604364	-75.2359192
7	200600342	312560.0878	1967106.504	2236.2848	-0.269891603	0.435735098	-75.89084724
8	200600343	312037.3114	1966977.196	2234.5501	-0.181593927	1.265134904	-75.62713519
9	200600344	311516.5065	1966847.207	2237.1906	-0.201691115	1.046327334	-75.15044873
10	200600345	310996.0056	1966713.415	2236.202	-0.504833185	0.455062103	-75.41867367
11	200600346	310474.7171	1966580.254	2235.5006	-0.331081466	0.729106647	-75.94019725
12	200600347	309954.6143	1966444.55	2236.0976	0.298616153	0.530852004	-74.68810027
13	200600348	309435.4956	1966303.358	2235.9126	-0.285283907	0.778003085	-74.89483002
14	200600349	308916.3095	1966165.315	2236.597	-0.723814109	0.839890075	-74.96351592
15	200600350	308396.2865	1966028.864	2236.3512	0.141973281	0.77579772	-75.06420934
16	200600351	307876.2496	1965892.68	2241.2343	-1.05903044	1.589818667	-75.7797838
17	200600352	307355.795	1965763.048	2243.8052	-0.339609168	0.63961832	-76.76663606

And there you have it. Two new workflows for importing CSV or TXT files into Excel.

Chad Lopez and Al Karlin, Ph.D., CMS-L, GISP are with Dewberry's Geospatial and Technology Services group in Tampa, FL. Chad is a Senior Geospatial Analyst who works primarily with imagery aerotriangulation, orthorectification, and feature extraction. As a Senior GIS Professional, Al works with all aspects of Lidar, remote sensing, photogrammetry, and GIS-related projects.

ASPRS WORKSHOP SERIES

It's not too late to earn
Professional Development Hours



Miss one of our Geo Week 2020 Live Online Workshops? Not to worry! You can purchase the workshops now and watch when you are ready! Check out the workshops offered by visiting:

<https://conferences.asprs.org/geoweek-2020/workshops/>

Image Priscilla Du Preez on Unsplash.



The Rising Star program is focused on mentorship of tomorrow's leaders within ASPRS and the geospatial and remote sensing community. Geospatial companies, agencies, and ASPRS regions can all benefit by participation in the program through the advancement and professional development of their employees or associates through the process of sponsorship.

For more information go to www.asprs.org/rising-star-program.

Ad Index

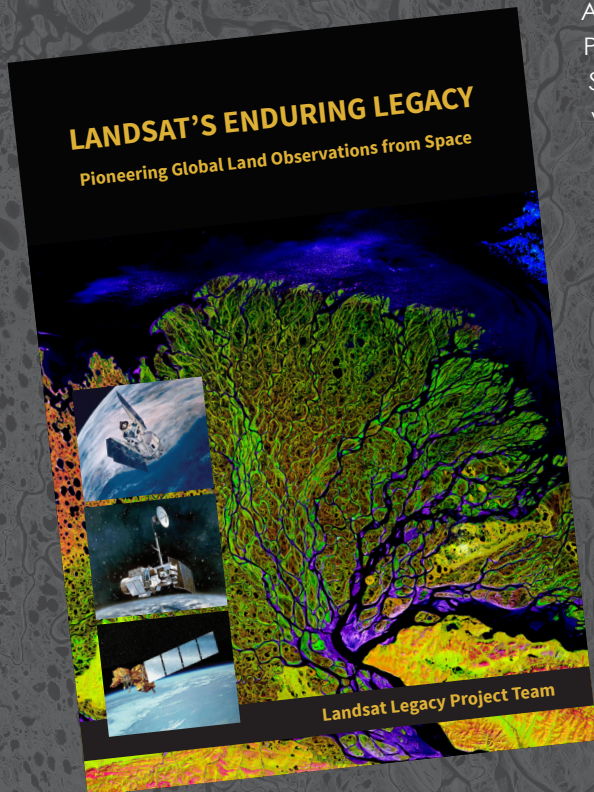
NRO

| www.nro.gov/Business-Innovation-Opportunities

| Cover 2

LANDSAT'S ENDURING LEGACY

PIONEERING GLOBAL LAND OBSERVATIONS FROM SPACE



After more than 15 years of research and writing, the Landsat Legacy Project Team is about to publish, in collaboration with the American Society for Photogrammetry and Remote Sensing (ASPRS), a seminal work on the nearly half-century of monitoring the Earth's lands with Landsat. Born of technologies that evolved from the Second World War, Landsat not only pioneered global land monitoring but in the process drove innovation in digital imaging technologies and encouraged development of global imagery archives. Access to this imagery led to early breakthroughs in natural resources assessments, particularly for agriculture, forestry, and geology. The technical Landsat remote sensing revolution was not simple or straightforward. Early conflicts between civilian and defense satellite remote sensing users gave way to disagreements over whether the Landsat system should be a public service or a private enterprise. The failed attempts to privatize Landsat nearly led to its demise. Only the combined engagement of civilian and defense organizations ultimately saved this pioneer satellite land monitoring program. With the emergence of 21st century Earth system science research, the full value of the Landsat concept and its continuous 45-year global archive has been recognized and embraced. Discussion of Landsat's future continues but its heritage will not be forgotten.

The pioneering satellite system's vital history is captured in this notable volume on Landsat's Enduring Legacy.

Landsat Legacy Project Team

Samuel N. Goward
Darrel L. Williams
Terry Arvidson
Laura E. P. Rocchio
James R. Irons
Carol A. Russell
Shaida S. Johnston

Landsat's Enduring Legacy

Hardback, 2017, ISBN 1-57083-101-7

Student	\$60*
Member	\$80*
Non-member	\$100*

* Plus shipping

Order online at
www.asprs.org/landsat





Mozhdeh Shahbazi, PhD, PEng, University of Calgary

How Good is that Gear? Drones versus Surveyors!

The integration of three-dimensional (3D) vision in drones or unmanned aerial vehicles (UAVs), has contributed a great deal to improving fine-scale mapping and monitoring applications. Passive imaging systems have been the most popular technologies used in this regard. This is mainly due to the availability of off-the-shelf, low cost, and light-weight digital cameras. Advancements in photogrammetry and computational stereo vision have also fostered this popularity (Abdullah, 2019).

As a survey engineer, a photogrammetric engineer, and a computer-vision scientist, I have given and received many debatable comments about these technologies. A question that it is still being debated by many stakeholders is this: can drone-photogrammetry result in survey-grade topographic products? The answer to this question cannot be summarized in a single word as each term used in this question is itself interpretable in several ways. In this column, we take a closer look at this question.

First, we review the main steps involved in the procedure of turning images into 3D topographic products (Figure 1). This workflow is more or less the backbone of any black-box commercial software or open-source solution available.

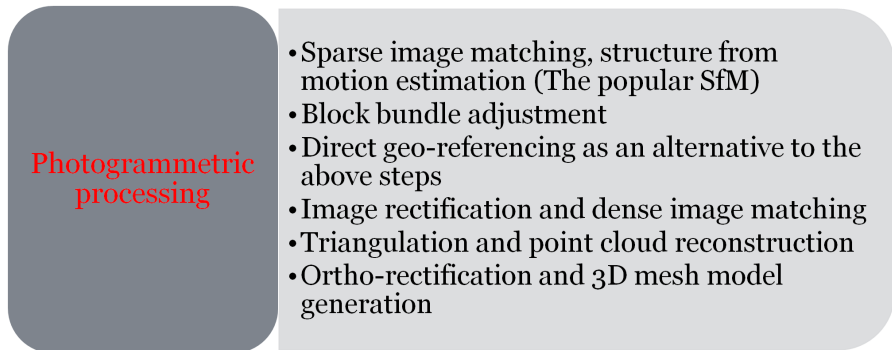


Figure 1. Steps in photogrammetric processing.

Drone Platforms

A conventional drone system for geospatial applications can be broken down into three discussable components: the platform, the navigation system, and the imaging sensor. Regarding the platform, the minimum specifications to consider are the payload capacity, endurance, degree of autonomy, ease of operation, and, last but not least, compliance with various regulations.

Navigation Sensors

GNSS-aided inertial navigation sensors are commonly de-

ployed in drone-photogrammetry systems for two purposes: auto-piloting the platform and, optionally, **georeferencing** the images. In most systems, an independent navigation system is dedicated to the latter. Georeferencing means determining the external orientation parameters of the images resolved in the mapping reference coordinate system. It can be performed in three ways: indirect georeferencing (InDG), direct georeferencing (DG), and integrated sensor orientation (ISO).

In InDG, georeferencing is performed by adding the observations of ground control points (GCPs) to the block bundle adjustment. Essential factors in the success of this method include the quality of the GCPs, their number, and their geometric distribution. The accuracy of GCPs dictates the achievable georeferencing accuracy; the georeferencing accuracy cannot supersede the average GCP accuracy. Georeferencing accuracy should not be confused with the reconstruction accuracy explained below. The only way to measure the georeferencing accuracy is to establish a fair amount of well-distributed ground checkpoints. Comparing their absolute measured coordinates with their photo-estimated coordinates yield a measure of georeferencing accuracy. In some commercial software, e.g. Pix4D Mapper, a variable is reported after initial processing, known as GCP error. It is worth mentioning that GCP error simply summarizes the difference between the observed coordinates and adjusted coordinates of the GCPs. High GCP errors can indicate either a gross error or an issue with the block bundle adjustment. Thus, a low GCP error should by no means be interpreted as high georeferencing accuracy. This is, unfortunately, a common mistake made by service providers when discussing their data quality.

In traditional airborne photogrammetry, the best configuration for GCPs is to set full control points at the corners and along the borders of the site, and height control points every 4-6 models and every 2-4 strips (Figure 2). However, in drone photogram-

Photogrammetric Engineering & Remote Sensing
Vol. 86, No. 7, July 2020, pp. 409–410.

0099-1112/20/409–410

© 2020 American Society for Photogrammetry
and Remote Sensing

doi: 10.14358/PERS.86.7.409

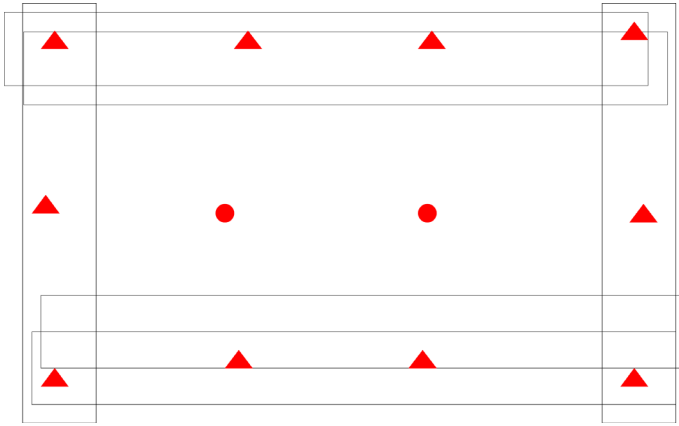


Figure 2. Suggested GCP configuration in airborne photogrammetry.

metry, usually higher model overlaps are recommended, and images are captured in unusual orientations, e.g. often highly oblique. Thus, this general suggestion for traditional photogrammetry might not be realizable as easily. Therefore, simpler configurations can be selected (Shahbazi et al., 2015)

In the case of direct georeferencing (DG), the external orientation parameters of the images are directly observed by the GNSS/INS without further modifications, i.e., one jumps directly to the dense matching step in the processing workflow. The accuracy of DG depends on three factors: the performance of the GNSS/INS components, the accuracy of platform calibration (determining the lever arm offsets and the boresight angles between the imaging and navigation sensors), and the multi-sensor time synchronization quality (depending on the flight speed, every microsecond of the synchronization bias matters!). Usually, DG is avoided unless the processing time is a priority, and one needs to skip the sparse-matching and bundle adjustment steps. The downside to this is that the DG errors directly propagate to the reconstruction errors. Finally, for ISO, the observations of the GNSS/INS are added to the block bundle adjustment as additional weighted observations. The main benefit of ISO is that there is no need for GCPs since the mapping datum gets defined by the GNSS/INS observations.

Imaging Sensors

When selecting the camera, one needs to pay close attention to its controllable parameters as shutter speed, focal distance, depth of focus, gain value, image size, image format, and rate of acquisition. The worst enemies of accurate photogrammetric products are auto-focus and zoom lenses.

A frequently asked question is whether one should calibrate the internal parameters of the camera offline before starting the photo mission or it is sufficient to perform an on-the-job self-calibration. The answer to this question depends on the mission configurations. If the imaging network is geometrically well configured and there are enough check data available on the site, then on-the-job self-calibration can be sufficient. Otherwise, throwing internal camera parameters as additional unknowns to the block bundle adjustment is not helpful – neither to camera calibration nor to scene reconstruction. The choice of camera model and lens (narrow-angle, wide-angle, and fisheye) adds another confusing element we will leave for future discussion.

The sensor pixel size and the lens focal length, together with the flight altitude, define the ground sampling distance (GSD), otherwise known as spatial resolution. However, one should be careful about reporting this theoretical GSD on the metadata of their photogrammetric products. For instance, a spatial resolution of 1-cm does not guarantee that one can distinguish two objects separated by a 1-cm distance in the produced point cloud. There are many factors such as texture, exposure sufficiency, and the dense-matching method which impact the density of the point cloud and, thus, the real GSD. Besides, the GSD is a highly variable value depending on the distance of the drone to the ground and the view-angle towards the object. Ideally, the average horizontal reconstruction accuracy must be in a range of 1 to 1.5 times the average GSD. As discussed, there can be no guarantee of this assumption. Considering reconstruction accuracy, we should clarify this often-misused term. When reconstructing the 3D model of an object, how close the model gets to the ground “truth”, e.g. vertical and horizontal distances and angles between corresponding points of the reconstructed model and the true model, is important. The reconstruction accuracy should not be confused with reconstruction completeness, which is a measure of how many detail gaps exist in the reconstructed model.

In conclusion, drone photogrammetry does have the potential of being used for surveying and high resolution mapping applications which demand high accuracy. However, many elements can negatively influence the correctness of this statement. In addition, considerable attention should be paid to the ways that service providers obtain, interpret, and represent the measures of precision, accuracy, and completeness for their topographic products.

References

- Abdullah, Q.A., 2019. Harnessing drones the photogrammetric way. *Photogrammetric Engineering & Remote Sensing* 85 (5):329-337. doi: 10.14358/PERS.85.5.329.
- Shahbazi, M.; Sohn, G.; Théau, J.; Menard, P.; Shahbazi, M.; Sohn, G.; Théau, J.; Menard, P., 2015. Development and Evaluation of a UAV-Photogrammetry System for Precise 3D Environmental Modeling. *Sensors* 15 (11) 27493–27524. doi.org/10.3390/s151127493.

Author

Mozhdeh Shahbazi (PhD, PEng) joined the Department of Geomatics Engineering at the University of Calgary in 2016. Since 2018 she has also been an adjunct professor at York University in the Earth and Space Science and Engineering graduate program. In 2019 she took on the role of lead scientist at the Centre de géomatique du Québec, a college-based center for technology transfer. She is Secretary of Working Group I, Technical Commission I of the ISPRS, a Director on the Board of the Canadian Remote Sensing Society (CRSS), chair of Working Group III at the CRSS; associate editor of *Canadian Remote Sensing Journal*; and associate editor of the *Journal of Unmanned Vehicle Systems*. Since 2012 her research has focused on autonomous mapping via vision-based unmanned aerial systems.

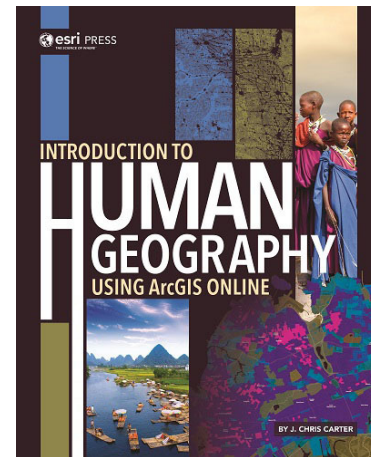
Introduction to Human Geography Using ArcGIS Online serves as an introductory textbook for undergraduate university students and high school A.P. Human Geography students. The book is organized conceptually around key areas of human geography and uses real-world data and examples to engage students with the subject. While the content and progression of this textbook are similar to other introductory texts in the study of human geography, this text separates itself by its inclusion of dozens of dynamic ArcGIS Online mapping exercises.

In chapter 1, the book begins with the introduction of broad ideas related to all subdisciplines of geography (e.g. space, region, place). However, *Introduction to Human Geography Using ArcGIS Online* immediately differentiates itself from other books on the market by also covering content one might find in an introductory GIS or Remote Sensing class. This includes subsections on various aspects of data collection, map generation, and statistical measures. While these topics take a back seat in the remainder of the book, they are used to support and engage readers in the ArcGIS Online mapping exercises and examples provided by the author.

Each chapter, excluding the first, focuses on one overarching area of study in human geography: population, migration, race and ethnicity, urban geography, food and agriculture, manufacturing, services, development, cultural geography, political geography, and human-environment interaction. Topics are explored in a deductive manner and highlight the most important ideas for students looking to complete the AP Human Geography examination or hoping to lay foundational groundwork for study in university-level geography. Approximately 4-7 mapping exercises are interspersed throughout each chapter to support and demonstrate key concepts at work.

The writing of this textbook is clear, concise, and pedagogical. Potentially contentious topics such as race and ethnicity are addressed with thoughtfulness and appropriate depth for an introductory course. Frequent subtitling and imagery incorporation also add to the book's readability. One weakness of the text is that some of the photos and maps are not quite crisp in resolution and visual quality. The images do however focus on powerful ideas and are thus still effective. Overall, the accessibility of the text and its wide use of real-world examples to demonstrate abstract concepts make the textbook engaging and relatable.

Another strength of this textbook is the inclusion of dozens of ArcGIS Online mapping exercises. The mapping exercises are rich, use dynamic and reputable data, and help expose readers to basic uses and practices of digital mapping. Mapping exercises can be accessed using a link found in the book and downloaded by chapter or in a bulk zip file. Available files contain the necessary data for the exercises as well as PDFs of lab-style instructions written in an easy-to-understand format. One can easily see the value of using up-to-date data with students instead of reviewing outdated figures, as well as providing students with a hands-on approach to topics that sometimes feel abstract to a young geographer. Instructors should be aware, however, that some exercises will require review and perhaps



Introduction to Human Geography Using ArcGIS Online

J. Chris Carter

Esri Press: Redlands, CA. 2019. 1x and 429 pp., diagrams, maps, photos, images, index. Softcover and Electronic. ISBN 9781589485198 (electronic). ISBN 9781589485181 (pbk.: alk. paper).

Reviewed by Stacey L. Kerr, Instructor, St. Jude School, Cincinnati, Ohio.

modification before assigning. This is because instructions for all exercises found in a single chapter appear in one large PDF. Opening a 70-page PDF of instructions (as is the case for the Chapter 1 exercises) could prove daunting to both high school and undergraduate students.

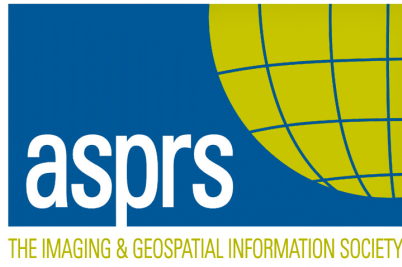
In sum, *Introduction to Human Geography Using ArcGIS Online* achieves its objective of introducing foundational topics in human geography to undergraduate and high school students with the help of active mapping exercises using ArcGIS Online. There are countless introductory texts on human geography, but this book fills a void in the literature by bridging the often-found gap between geospatial technologies education and human geography education. Effective instructor use of this text should allow students to see and understand the connection between various geography disciplines, instead of viewing them as discrete entities. This book could be valuable to both the instructor of human geography courses, in addition to GIS and Remote Sensing instructors looking for engaging lab exercises.

Photogrammetric Engineering & Remote Sensing
Vol. 86, No. 7, July 2020, pp. 411.

0099-1112/20/411

© 2020 American Society for Photogrammetry
and Remote Sensing

doi: 10.14358/PERS.86.7.411



ASPRS AERIAL DATA CATALOG

“THE SOURCE FOR FINDING AERIAL COLLECTIONS”

[HTTP://DPAC.ASPRS.ORG](http://dpac.asprs.org)

The ASPRS Aerial Data Catalog is a tool allowing owners of aerial photography to list details and contact information about individual collections.

By providing this free and open metadata catalog with no commercial interests, the Data Preservation and Archiving Committee (DPAC) aims to provide a definitive metadata resource for all users in the geospatial community to locate previously unknown imagery.

DPAC hopes this Catalog will contribute to the protection and preservation of aerial photography around the world!

ASPRS Members: We Need Your Help!
There are three ways to get involved

1

USE

Use the catalog to browse over 5,000 entries from all 50 states and many countries. Millions of frames from as early as 1924!

2

SUPPLY

Caretakers of collections, with or without metadata, should contact DPAC to add their datasets to the catalog free of charge!

3

TELL

Spread the word about the catalog! New users and data collections are key to making this a useful tool for the community!

For More Details or To Get Involved Contact:

DAVID RUIZ • DRUIZ@QUANTUMSPATIAL.COM • 510-834-2001 OR DAVID DAY • DDAY@KASURVEYS.COM • 215-677-3119



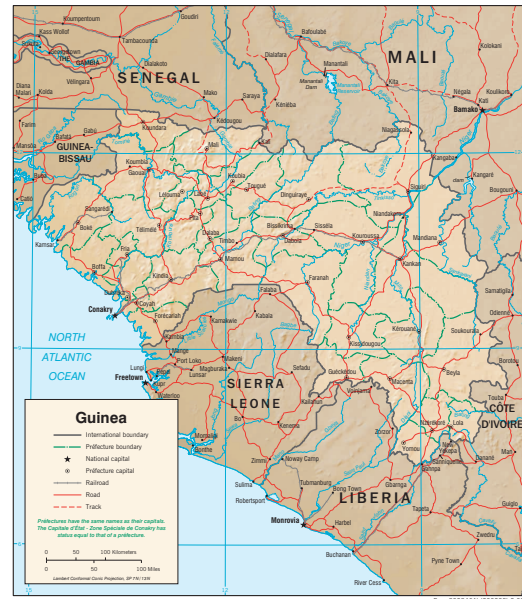
& GRIDS & DATUMS

BY Clifford J. Mugnier, CP, CMS, FASPRS

REPUBLIC OF GUINEA

The Grids & Datums column has completed an exploration of every country on the Earth. For those who did not get to enjoy this world tour the first time, *PE&RS* is reprinting prior articles from the column. This month's article on the Republic of Guinea was originally printed in 2002 but contains updates to their coordinate system since then.

The original inhabitants of Guinea were forced out of the area around 900 A.D., and numerous kingdoms were subsequently established. By the mid 1400s, the Portuguese visited the area and a slave trade was established. The area was under active trade with the British, French, and Portuguese in the 17th century; and the coastal region was declared a French Protectorate in 1849. Administered at various times by Senegal and the Rivières du Sud, the territory of French Guinea was made a colony in 1893. The Federation of French West Africa, which included Guinea as a member, was established in 1895. Its status was changed to that of an overseas territory in 1946, and on 02 October 1958, Guinea became the first state of the former French West Africa to gain independence. Guinea includes the Los Islands, an island group west of the capitol city of Conakry. The seacoast is marshy and is about 274 km long; the interior rises to hilly and plateau regions. The highest point is Mount Nimba (1,752 m), near the tripoint with Côte d'Ivoire and Liberia. Going clockwise from the north Atlantic Ocean to the west, Guinea shares borders with Guinea-Bissau, Senegal, Mali, Côte d'Ivoire, Liberia, and Sierra Leone. The Guinean maritime boundary is defined in large part by a single, unique (in the world) Straight Baseline. By Decree of the President of the Republic in 1964, the limits of the territorial waters are fixed "to the north, by parallel of altitude 10° 56' 42.55" north, and to the south, by parallel of altitude 9° 03' 18" north, along a distance of 130 sea miles seaward, reckoning from a straight line passing by the south-west of Sene Island of the Tristao group, and to the south, by the south-west foreland (cape) of Tamara Island, at low tide." The boundary between Guinea and Guinea-Bissau was established through a Franco-Portuguese convention of 12 May 1886. The demarcation of the 384-km



boundary with straight lines between 58 markers and along thalwegs of rivers was completed and approved by 1906. In 1915 an *arrêté* (decision) by the Governor General of French West Africa promulgated a French decree establishing a 328 km boundary between French Guinea and Senegal. Early in 1934 an *arrêté* promulgated a decree of the previous December changing the French Guinea –Senegal boundary in the sector between the head of the Tanague River and the junction of the Bitari and Koila Kabé. A Franco-Liberian convention of 08 December 1892 delimited a boundary between the possessions of France (Côte d'Ivoire and French Guinea) and Liberia inland from the mouth of the Cavalla River to the tripoint with Sierra Leone. That 560 km boundary with French Guinea was redrawn on 18 September 1907. Further surveys and commissions settled the matter with several *procès verbaux* (verbal proceedings) finally in 1926. The Guinea-Sierra Leone boundary has a length of approximately 648 km. Established by Anglo-French convention of 28 June 1882, a boundary was delimited from the Atlantic

Photogrammetric Engineering & Remote Sensing
Vol. 86, No. 7, July 2020, pp. 413–416.

0099-1112/20/413–416

© 2020 American Society for Photogrammetry
and Remote Sensing

doi: 10.14358/PERS.86.7.413

Ocean inland along the drainage divide of the Great Scarcies and Mélikhouré (rivers) to an in-definite point in the interior. Later determined by field surveys, the last agreement fixing the boundary was signed on 04 September 1913. In places, the boundary measurements are described to the closest half-meter. Reading between the lines, I'd guess that the boundary commission surveyors had people literally looking over their shoulders during that process!

When the federation of the eight territories constituting French West Africa came into being in 1904, the *Annexe de l'Institut Géographique National à Dakar* had the local responsibility for topographic mapping. Also known as the *Service Géographique de l'Afrique Occidentale Française* SGAOF (Geographic Service of the French West Africa), topographic mapping of Guinea has been largely at the scales of 1:200,000 and 1:500,000. This agency has performed a small amount of mapping at the scales of 1:20,000, 1:50,000, and 1:100,000. Topographic mapping of Guinea was in the past largely the result of rapid ground surveys. After WWII, the French adopted aerial photography controlled by astronomical points ("Astro" stations) as the means of surveying and mapping at scales of 1:50,000 and 1:200,000. These compilations were also used for derivative mapping at smaller scales. There is complete coverage of the country at 1:500,000 scale, and at

1:200,000 scale. The latter consists of sheets mainly based on ground surveys. A small portion of Guinea has 1:50,000-scale topographic sheets compiled, mostly by the French IGN in the coastal west, and by a cooperative agreement with the Japanese (JICA) for some sheets around Kankan and Kérouané-Macenta.

The oldest coordinate system in Guinea that I have been able to locate (with help) is the Conakry Datum of 1905 where $\Phi_0 = 9^\circ 30' 58.997''$ N, $\Lambda_0 = 13^\circ 42' 47.483''$ West of Greenwich, $\xi_0 = -4.50''$, $\eta_0 = -0.02''$, and the ellipsoid of reference is the Clarke 1880 (IGN) where $a = 6,378,249.2$ m and $1/f = 293.4660208$. Thanks go to both John W. Hager, retired from NIMA, and to Russell Fox of the Ordnance Survey of the U.K. The origin point is at the Public Works Building in Conakry, and John W. Hager went on to say: "Reingold cites *Les Manuels Coloneaux*, "Cartographie Coloniale," Paris, 1935 and "Catalogue de Positions Géographiques," Paris, 1923 give the position to the nearest second. *Annales Hydrographiques*, 4e Série, Tome 1, Année 1950, Paris 1951, p. 155 gives the above but is listed as 3rd order. A position for the Railway Astro Pillar is given as latitude = $9^\circ 30' 54.5''$ N and longitude = $13^\circ 42' 47.1''$ W, a difference in position of 138.6 meters. I would assume that the astro pillar was not permanently marked."

Some minor hydrographic surveys were performed by the

STAND OUT FROM THE REST

EARN ASPRS CERTIFICATION

ASPRS congratulates these recently Certified and Re-certified individuals:

CERTIFIED MAPPING SCIENTIST LIDAR

Sarah Stillman, Certification #L052

Effective June 1, 2020, expires June 1, 2025

CERTIFIED LIDAR TECHNOLOGIST

Tyler Stentz, Certification #035LT

Effective May 27, 2020, expires May 27, 2025

CERTIFIED UAS TECHNOLOGIST

John Monaco, Certification #034UAST

Effective June 2, 2020, expires June 2, 2023

CERTIFIED GIS/LIS TECHNOLOGISTS

Morgan Ridler, Certification #303GST

Effective May 27, 2020, expires May 27, 2023

Taylor Moore, Certification #302GST

Effective May 19, 2020, expires May 19, 2023

Matthew Brice, Certification #301GST

Effective May 19, 2020, expires May 19, 2023

Michael Mann, Certification #300GST

Effective May 19, 2020, expires May 19, 2023

RECERTIFIED PHOTOGRAMMETRIST

Dennis P. Sauers, Jr., Certification #R1433

Effective December 27, 2019, expires December 27, 2024

ASPRS Certification validates your professional practice and experience. It differentiates you from others in the profession. For more information on the ASPRS Certification program: contact certification@asprs.org, visit <https://www.asprs.org/general/asprs-certification-program.html>



French Navy, and these were based on local astro stations that served as origins of grids computed on the Hatt Azimuthal Equidistant projection. The Tabola River survey had its origin at Cabrion Base North End (1936) where $\Phi_0 = 9^\circ 56' 08.1$ N and $\Lambda_0 = 13^\circ 54' 42.4''$ West of Greenwich.

The defining azimuth to Cabrion Base South End was $\alpha_0 = 123^\circ 34' 00''$, and the baseline length was 1017.537 m. I was wondering why the French performed a survey in such a tiny locale that did not even appear on the standard CIA map of the country. I examined my *Carte Générale of Guinée* and noticed that there is a road to there through the town of Koba that winds north up into the hills. Apparently, something valuable was being trucked out of those hills to the port of Taboriya. Hager found one at “Binari 1949 (code BIN) at the I.G.N. Astro, latitude = $10^\circ 30' 26.2''$ N, longitude = $14^\circ 38' 45.0''$ W (1) or ... $41.03''$ (2) or ... $40.0''$ (3), Clarke 1880. Position (1) is from *Annales Hydrographiques*, 4e série, Tome Sixième, Année 1955, p. 247. Position (2) is from *Annales Hydrographiques*, 4e série, Tome Dixième, Années 1959-1960, p. 65, Paris 1961. Position (3) is a footnote to (2) and refers to the 1954 survey by M. Sauzey.”

There have been some other rather curious coordinate systems devised for Guinea during the 20th century. Prior to and during WWII, there were a number of military Grids that were collectively termed the “British Grids.” These were all documented and computed into projection tables by the U.S. Army. One published by the U.S. Army Corps of Engineers Lake Survey in 1943 was the Guinea Zone based on the Lambert Conical Orthomorphic Projection Tables. The defining parameters are Latitude of Origin, $(\phi_0) = 7^\circ$ N, Central Meridian $(\lambda_0) = 0^\circ$ (Greenwich), Scale Factor at the Parallel of Origin $(m_0) = 0.99932$, False Northing, FN = 500 km, and False Easting, FE = 1,800 km. The wording for the projection is characteristically British, as is the method of presenting the defining parameters, and the projection is definitely the fully conformal version rather than the French Army version of the time. Furthermore, the parameters given for the Clarke 1880 ellipsoid were the British version where $a = 6,378,249.145$ m and $1/f = 293.465$. This grid continued in use by the U.S. Army Map Service for a couple of de-cades after WWII.

Immediately after WWII, the French Institut Géographique National devised a number of grids for l'A.O.F. useage as of 12 December 1945. The region of French Guinea was to be covered by two fuseau, or zones: “Fuseau Sénégal” with $\lambda_0 = 13^\circ 30'$ West of Greenwich, and “Fuseau Cote d'Ivoire” with $\lambda_0 = 6^\circ 30'$ West of Greenwich. The scale factor at origin $(m_0) = 0.999$ and the ellipsoid of reference was to be the International (Hayford 1909) where $a = 6,378,388$ m and $1/f = 297$. Because there was not a great deal of existing mapping in French West Africa at the time, most datums were established by astro shots and few classical chains of quadrilaterals had been surveyed. The introduction of a new ellipsoid was therefore not of major geodetic importance to existing cartographic work. French Navy Hydrographic surveys of the late 1940s in Guinea were cast on the Fuseau Sénégal Grid. When I was in

college, I once read a science fiction novel about a disgruntled cartographer on a lonely expedition to a new planet. He chose risqué names for his gazetteer, and that fact went undiscovered for many years. While perusing the report of the French Navy hydrographic survey of the mouth of the Saloum River (*Mission Hydrographique de la Côte Ouest d'Afrique, 11 Mai 1950 – 18 Mai 1952*), guess what I found? Yep, an American vulgarism and an American gangster's name for triangulation stations!

The U.S. Army Map Service concocted the Universal Transverse Mercator (UTM) Grid System for worldwide use in 1948. France had been trying to gain an international consensus for some sort of similar system, and quickly adopted the UTM for most of its colonies. As of 30 September 1950, all new surveying and mapping of French Guinea was done on the UTM Grid. That situation remains to this day. The only information available on a datum shift from the local datum to WGS84 for the entire country of Guinea is the entry in NIMA's TR8358.2 for “Dabola Datum” where $\Delta a = -112,145$, $\Delta f \times 10^4 = -0.54750714$, $\Delta X = -83\text{m} \pm 15\text{m}$, $\Delta Y = +37\text{m} \pm 15\text{m}$, and $\Delta Z = +124\text{m} \pm 15\text{m}$. This four-point solution was published by NIMA in 1991. Because there is only a 1:200,000 scale map published of Dabola, and there are no 1:50,000-scale topographic maps nearby, I am unable to find a plausible reason for the choice of this transformation name or location other than it is more or less in the center of the country. I have found no other evidence of such a datum in existence.

UPDATE

Missions

The National Geographic Institute's mission is to design, implement and monitor the National Policy for National Geospatial Data Infrastructures (INDG).

As such, it is particularly responsible for:

- create, densify and protect the geodetic reference and leveling networks;
- to produce updated basic maps on a variable scale corresponding to the economic vocation of the country;
- to develop and ensure the application of national standards in terms of geodesy, cartography and aerial and satellite shots and to ensure control and harmonization of production in these areas,
- to set up, at national level, a harmonized Geographic Information System (GIS);
- participate in carrying out work relating to the materialization of national borders and administrative boundaries;
- to participate in the development of terms of reference for tender documents and in the examination of offers from the geodesy, cartography and aerial photography markets.

The National Geographic Institute is the legal depositary of all cartographic, geodetic and aerial photography production on the national territory of which it ensures the filing.

Organization / Teams

To accomplish its mission, the National Geographic Institute includes:

- **A Land Survey Service**, responsible for:
 - to design, establish, densify and maintain the national geodesic canvas, the general state leveling networks and any other network or canvas such as the astronomical and gravimetric network;
 - to draw up technical standards in terms of topography, geodesy and to ensure their correct use;
 - to provide services in its field of activity;
 - to carry out topographic and geodetic work relating to the materialization of borders and administrative boundaries.
- **A Cartography and Geographic Information System (GIS) Service**, responsible for:
 - to design and carry out basic mapping work throughout the national territory;
 - ensuring the control and harmonization of cartographic production;
 - to draw up technical standards, in particular conventional signs and to ensure their application;
 - to set up and manage the National Geographic Information System;
 - to carry out toponymic surveys with a view to standardizing geographical names;
 - manage, maintain and develop the map library;
 - participate in the development and / or validation of TORs, tender documents for mapping projects,
 - to participate in the analysis and analysis of the offers of the public mapping markets.
- **An Air Surveys and Remote Sensing Service**, responsible for:
 - to regulate all aerial shots
 - to carry out photo-interpretation and stereo preparation work;
 - carry out remote sensing and photo laboratory work as a service;

- develop technical standards in the field of aerial surveys and remote sensing and ensure their correct use;
- draft specifications for projects relating to aerial photography;
- ensuring the control and harmonization of aerial photography;
- manage and maintain the photo library;
- to participate in the preparation of tender documents and in the analysis and analysis of offers from aerial photography markets.

- **An Administrative and Financial Service**, responsible for:
 - to provide the central secretariat of the Institute;
 - to draw up the annual budget of the Directorate in relation to the technical services and to carry out all financial and accounting operations;
 - to maintain the premises, rolling stock and IT equipment of the Institute;
 - prepare and / or supervise the production of the financial reports of the Institute and present them.

A new territorial waters boundary is written that references positions on the WGS84 Datum but offers no ties to existing terrestrial coordinate systems.

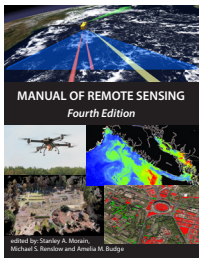
- DECREE NO. D/2015/122/PRG/SGG, 19 June

<https://www.mtp.gov.gn/le-ministere/etablissements-publics/ign/>.

The contents of this column reflect the views of the author, who is responsible for the facts and accuracy of the data presented herein. The contents do not necessarily reflect the official views or policies of the American Society for Photogrammetry and Remote Sensing and/ or the Louisiana State University Center for GeoInformatics (C⁴G).

This column was previously published in *PE&RS*.

NOW AVAILABLE!



ASPRS Announces the 4th Edition of the *Manual of Remote Sensing*!

The *Manual of Remote Sensing, 4th Ed.* (MRS-4) is an “enhanced” electronic publication available online from ASPRS. This edition expands its scope from previous editions, focusing on new and updated material since the turn of the 21st Century. Stanley Morain (Editor-in-Chief), and co-editors Michael Renslow and Amelia Budge have compiled material provided by numerous contributors who are experts in various aspects of remote sensing technologies, data preservation practices, data access mechanisms, data processing and modeling techniques, societal benefits, and legal aspects such as space policies and space law. These topics are organized into nine chapters. MRS4 is unique from previous editions in that it is a “living”

document that can be updated easily in years to come as new technologies and practices evolve. It also is designed to include animated illustrations and videos to further enhance the reader’s experience.

MRS-4 is available to ASPRS Members as a member benefit or can be purchased by non-members. To access MRS-4, visit <https://my.asprs.org/mrs4>.



JOURNAL STAFF

Editor-In-Chief

Alper Yilmaz, Ph.D., PERSeditor@asprs.org

Associate Editors

Rongjun Qin, Ph.D., qin.324@osu.edu

Michael Yang, Ph.D., michael.yang@utwente.nl

Petra Helmholz, Ph.D., Petra.Helmholz@curtin.edu.au

Bo Wu, Ph.D., bo.wu@polyu.edu.hk

Clement Mallet, Ph.D., clemallet@gmail.com

Vasit Sagan, Ph.D., Vasit.Sagan@slu.edu

Jose M. Pena, Ph.D., jmpena@ica.csic.es

Prasad Thenkabail, Ph.D., pthenkabail@usgs.gov

Ruisheng Wang, Ph.D., ruiswang@ucalgary.ca

Desheng Liu, Ph.D., liu.738@osu.edu

Valérie Gouet-Brunet, Ph.D., valerie.gouet@ign.fr

Dorota Iwaszczuk, Ph.D., dorota.iwaszczuk@tum.de

Qunming Wang, Ph.D., wqm11111@126.com

Filiz Sunar, Ph.D., fsunar@itu.edu.tr

Norbert Pfeifer, Ph.D., np@ipf.tuwien.ac.at

Jan Dirk Wegner, Ph.D., jan.wegner@geod.baug.ethz.ch

Hongyan Zhang, Ph.D., zhanghongyan@whu.edu.cn

Zhenfeng Shao, Ph.D., shaozhenfeng@whu.edu.cn

Dongdong Wang, Ph.D., ddwang@umd.edu

Assistant Editor

Jie Shan, Ph.D., jshan@ecn.purdue.edu

Contributing Editors

Grids & Datums Column

Clifford J. Mugnier, C.P., C.M.S., cjmce@lsu.edu

Book Reviews

Sagar Deshpande, Ph.D., bookreview@asprs.org

Mapping Matters Column

Qassim Abdullah, Ph.D., Mapping_Matters@asprs.org

Sector Insight

Lucia Lovison-Golob, Ph.D., lucia.lovison@sat-drones.com

Bob Ryerson, Ph.D., FASPRS, bryerson@kimgeomatics.com

GIS Tips & Tricks

Alvan Karlin, Ph.D., CMS-L, GISP akarlin@Dewberry.com

ASPRS Staff

Assistant Director — Publications

Rae Kelley, rkelley@asprs.org

Electronic Publications Manager/Graphic Artist

Matthew Austin, maustin@asprs.org

Advertising Sales Representative

Bill Spilman, bill@innovativemediasolutions.com

NEW ASPRS MEMBERS

ASPRS would like to welcome the following new members!

At Large

Yuwei Cai

Carol Lockhart

Bo Wu, Ph.D.

Cascadia

Benjamin M. Allen

Katharine Hannah Nicolato

Florida

Dr. Howard Andrew Lassiter

Heartland

David Beattie

Dr. Gregory Rouze

Todd Greenwood

Mid South

James B. Gillis, PLS

Dustin McGrew

Evan Lee Merelli

Mark W. O'Neal, CP

Lindsey Galyen, Jr.

North Atlantic

Brenda Allen

Cori Elizabeth Indelicato

Northeastern

Lindsay J. Gee

Bethany Lauren Muñoz Delgado

Pacific Southwest

Hikari Murayama

Potomac

Clayton Brenke

Sawsan Gad

Hatteras Hoops

Ryan Lavery

Louis Neel

Rocky Mountain

Manuel Larsen Santos, GST

FOR MORE INFORMATION ON ASPRS MEMBERSHIP, VISIT

[HTTP://WWW.ASPRS.ORG/JOIN-NOW](http://www.asprs.org/join-now)

Your Path To Success In The Geospatial Community

Call for Submissions

Special Issue on Urban Remote Sensing

Photogrammetric Engineering and Remote Sensing (PE&RS) is seeking submissions for a special issue on Urban Remote Sensing.

The formulation of the 17 Sustainable Development Goals (SDGs) is a major leap towards humankind's quest for sustainability. In recent decades, global urban areas have been rapidly expanding, especially in developing countries. The prospect is that the urbanization rate will reach 60% by 2030. Urban expansion will inevitably increase vulnerability to natural hazards, natural vegetation cover decline and arable land loss, urban heat islands, air pollution, hydrological cycle alteration and biotic homogenization. Since urban ecosystems are strongly influenced by anthropogenic activities, a considerable amount of research has been conducted all around the world to understand the spatial patterns, driving forces and the ecological and social consequences of urbanization. It is not only crucial for characterizing the ecological consequences of urbanization but also for developing effective economic, social and environmental policies in order to mitigate its adverse impacts.

Remote sensing has been widely used for investigating urban environment and the associated drivers during the urbanization process, as it can quickly and frequently monitor large area surface change with lower cost, compared to field survey or in situ measurements. Digital archives of remotely sensed data provide an excellent opportunity to study historical urban changes and to relate their spatio-temporal patterns to environmental and human factors. With the rapid development of Earth observation techniques, it has become convenient to obtain a large number of remotely-sensed imagery over a certain area at different times, from hundreds of Earth observation platforms. However, this brings challenges to researchers to timely process the remote sensing big data as well as to rapidly transfer the data into information and knowledge.

Considering this, this special issue of *PE&RS* is aimed at reporting novel studies on exploiting remote sensing big data to monitor and improve urban environment, and showing the potential of remote sensing in developing sustainable cities, including but not limited to:

- Urban remote sensing big data
- Remote sensing information interpretation
- Urban expansion, dynamics and associated environment consequences
- Remote sensing of urban water quality

- Remote sensing of urban thermal environment
- Remote sensing of urban geological environment
- Urban sustainability assessment
- Urban sustainable development
- Urban Spatiotemporal analysis
- Urban Sustainability Indicators
- Urban environmental Monitoring

Papers must be original contributions, not previously published or submitted to other journals. Submissions based on previous published or submitted conference papers may be considered provided they are considerably improved and extended. Papers must follow the instructions for authors at <http://asprs-pers.edmgr.com/>.

Important Dates

- July 1, 2020 Submission system opening
- October 31, 2020 Submission system closing
- Planned publication date: Dec. 2020
- Submit your manuscript to <http://asprs-pers.edmgr.com/> by Oct. 31, 2020.

Guest Editors

Zhenfeng Shao, *Wuhan University, China*

Prof. Zhenfeng Shao, Professor at the State Key Laboratory of Information Engineering in Surveying, Mapping and Remote Sensing, Wuhan University, China. His research interests include urban remote sensing. He is now an associate editor of Email: shaozhenfeng@whu.edu.cn.

Orhan Altan, *Istanbul Technical University, Turkey*

Prof. Orhan ALTAN, Professor at the Department of Geomatics Engineering, Istanbul Technical University, Turkey. He is Past President and Honorary Member of ISPRS, Honorary Member of Science Academy. He has published more than 200 scientific papers in scientific journals and conferences, and editor or co-editor of more than 20 international books. Email: oaltan@itu.edu.tr

J.L.van Genderen, *University of Twente, Netherlands*

Professor J.L.van Genderen, Prof. at the Department of Earth Observation Science, Faculty of Geo-information Science and Earth Observation(ITC),University of Twente, Netherlands, he is an associate Editor of Geo-Spatial Information Science. His research interests include photogrammetry and remote sensing, urban remote sensing and computer vision. Email: Genderen@alumni.itc.nl.

A History of Laser Scanning, Part 1: Space and Defense Applications

Adam P. Spring

Abstract

This article presents the origins and evolution of midrange terrestrial laser scanning (TLS), spanning primarily from the 1950s to the time of publication. Particular attention is given to developments in hardware and software that document the physical dimensions of a scene as a point cloud. These developments include parameters for accuracy, repeatability, and resolution in the midrange—millimeter and centimeter levels when recording objects at building and landscape scales up to a kilometer away. The article is split into two parts: Part one starts with early space and defense applications, and part two examines the survey applications that formed around TLS technologies in the 1990s. The origins of midrange TLS, ironically, begin in space and defense applications, which shaped the development of sensors and information processing via autonomous vehicles. Included are planetary rovers, space shuttles, robots, and land vehicles designed for relative navigation in hostile environments like space and war zones. Key people in the midrange TLS community were consulted throughout the 10-year period over which this article was written. A multilingual and multidisciplinary literature review—comprising media written or produced in Chinese, English, French, German, Japanese, Italian, and Russian—was also an integral part of this research.

Introduction

Midrange terrestrial laser scanning (TLS) developed out of space and defense applications. As will be discussed in part two, it evolved as a laser-based methodology that documents an object or environment to a known scale of measurement. Government agencies such as the Defense Advanced Research Projects Agency (DARPA) were a main source of funding for midrange TLS from the 1960s to the 1990s, until the technology was recognized as a valuable tool for industrial uses during the period 1987–1998. Up to that point, midrange TLS provided an effective solution for the operation of unmanned vehicles and robots in environments otherwise hazardous to humans, such as war zones and space. It was primarily created and refined for use in remote navigation systems from the 1960s to the 1990s. Subsequent uses based on computer-aided documentation, which were facilitated by industrial as well as cultural-heritage (CH) applications, began in the late 1980s. Transitions into this world of survey and documentation were as much about changes in business cultures and practices as they were about the available technologies in place at the time.

Four phases of development for mid-range TLS are explored in both parts of this article. The first phase is the initial technological development – where government agencies like DARPA and the National Aeronautics and Space Administration (NASA) started sensor-led initiatives. The second phase seeded business cultures and technologies - via corporate philanthropy laws, technology transfer laws and further developments in microelectronics. The third phase is shaped by the tripod based commercial systems that inspired this article,

along with non-profit corporations that came out of California. Phase four was still playing out at the time this article was published. It is a period where remote navigation, mixed reality applications and simultaneous and localized mapping were transforming midrange TLS sensors into commodity items. Where mobile phones, tablet based computing and car based applications were clearly shaping future developments.

Time of flight (ToF) and phase-shift (PS) laser scanning in phases one and two of the development cycle are predominantly focused on in part one of this article. This part ends at the point where triangulation-based midrange TLS systems (developed by Xin Chen and with the founding of Mensi in 1987 by Auguste D'Aligny and Michel Paramythioti) became the gateway to industrial applications, which helped turn laser scanners into survey instruments (see Figure 1b). It explores initiatives funded by government agencies like DARPA, NASA, and the European Space Agency (ESA); the partnerships formed to develop solutions alongside emerging trends in computing; and early user adoption outside of space- and defense-based applications. It also lays the foundation for later discussions outlined in part two. This includes midrange TLS as it is currently defined, as well as an exploration of the period where technologies made the transition to commercial markets of use.

The Road to General Use

A road map of the development of midrange TLS is presented in Figure 1a. It shows the applications, technological developments, and projects that were required to attain the broad range of application that is now possible. For example, the period of research and development dating back to the 1960s was an era shaped by space and defense applications, where the development cycle in place was driven by artificial intelligence and robotics (Matthies 1999). The funding model that sustained it was driven by government grants (Waldron and McGhee 1986; Song and Waldron 1989; Everett 1995; Gleichman *et al.* 1998; Matthies 1999; Roland and Shiman 2002). Laser based sensors were developed to serve the interests of departments like DARPA and later research programs like the Strategic Computing Initiative (Roland and Shiman 2002).

Despite being overlooked or untold, this part of the story of midrange TLS remains embedded in solutions used today. For example, laser scanners know their position in relative space because they were originally used for relative navigation in space-driven applications. The methodology can be traced back to the Space Race, where it became part of the NASA Surveyor program (Matthies 1999). It was this initiative that identified the need for more accurate sensors and sensing in unmanned space exploration—for guidance systems that could be used in vehicles like planetary rovers or docking space shuttles (Lewis and Johnston 1977; Waldron and

Photogrammetric Engineering & Remote Sensing
Vol. 86, No. 7, July 2020, pp. 419–429.
0099-1112/20/419–429

© 2020 American Society for Photogrammetry
and Remote Sensing

doi: 10.14358/PERS.86.7.419

Remotely Interested LLC, adam@remotely-interested.com

McGhee 1986; Gleichman *et al.* 1988; Tchoryk *et al.* 1991; Everett 1995; Flatscher *et al.* 1999; Gage 1995; Matthies 1999; Nilsson 2010). Feeding into this were sensors that came out of the Environmental Research Institute of Michigan (ERIM) and the Jet Propulsion Laboratory (JPL) at the California Institute of Technology (Matthies 1999; Roland and Shiman 2002).

The technologies developed between 1966 and 1997 were not created with an intention to compete with survey equipment like total positioning stations, as they do in the marketplace today. The driving force behind their refinement was government- and university-led initiatives like the Surveyor program and the Carnegie Mellon University (CMU) Navigation Laboratory (NavLab) (Everett 1995; Roland and Shiman 2002). This continued to be the case until commercialization took place in the 1990s.

Prior to the development of tripod-mountable systems for surveying, midrange TLS solutions had been used on satellites, space-exploration vehicles, robots like Shakey or Odex I, and autonomous land vehicles (Moravec 1983; Kweon, Hoffman and Krotkov 1991; Everett 1995; Matthies 1999). It was a form of computer vision used for navigation and terrain modeling, as an alternative to passive video and stereo camera-based navigation like structure from motion (Besl 1988; Tchoryk *et al.* 1991; Amann *et al.* 2001). For example, the Adaptive Suspension Vehicle (ASV) and Autonomous Land Vehicle (ALV) projects, which were funded by DARPA, both used laser scanners as part of their guidance systems (Waldron and McGhee 1986; Gleichman *et al.* 1988; Song and Waldron 1989). Again, they were used to guide vehicles remotely through war zones and other environments hazardous to humans.

Shakey

Running parallel to the Surveyor program (1966–1968) was the DARPA-funded artificial-intelligence project called Shakey (1966–1972). This four-wheeled robot was developed by the

Stanford Research Institute (Nilsson 1984). It incorporated both active and passive systems of sensing into its design, which made it autonomous in a specially designed environment (Nilsson 1969, 1984, 2010; Moravec 1983; Gage 1995). Shakey could use a vidicon television camera or a custom-built laser range finder (with rotating mirror) to determine its location (Nilsson 1984; “Shakey Images” n.d.). Its design laid the foundation for TLS in general in robotic engineering at the Stanford Research Institute, as well as at CMU via Hans Moravec (Moravec 1983; Gage 1995). Shakey currently resides in the Computer History Museum in Mountain View, California (“Shakey” 2018).

Space, Defense, and Autonomous Vehicles

By 1977, a ToF-based scanning device, the Scanning Laser Rangefinder, had been developed by JPL (Lewis and Johnston 1977; Everett 1995). The project identified limitations based on accuracy, how these limitations might be mitigated, and laid the groundwork for tripod-based ToF solutions (Lewis and Johnston 1977). Yoshiaki Shirai and his team at the Electrotechnical Laboratory in Tokyo had also developed a slit projection-based method for range-finding in the period after Shakey but before the work at JPL. This was for the vision system in their ETL-ROBOT, with point information represented in a scan line-based pattern (Shirai 1972). Similar triangulation-based methods are discussed later in the section called **The Point Cloud** – via the early CH based work of the Coignard family (Figure 6) and (separately) the Scannerless Range Imager. The latter was developed at Sandia National Laboratories in New Mexico, and was built to run on a Motorola 68000 computer processing unit-based Amiga computer (Sackos *et al.* 1998).

Hans Moravec also explored navigation and obstacle avoidance at the Stanford Research Institute around the same period as the JPL Scanning Laser Rangefinder, 1973 to 1981, (Moravec 1983; Gage 1995). He used a stereo vision system on

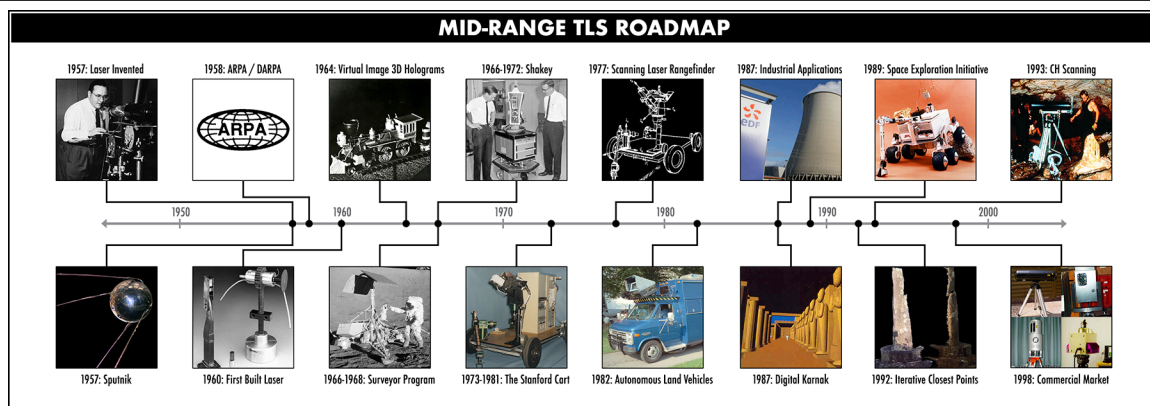


Figure 1. (a) The road map of midrange terrestrial laser scanning outlines the transition from vehicle-based systems, which started out as research-funded projects focused on space and defense applications. These solutions eventually crossed over to commercial tripod-based applications for geodetic and surveying-based uses in 1998. They were, however, first used for industrial and cultural heritage applications in the build up to a market forming around the technology. ARPA= Advanced Research Projects Agency; CH = cultural heritage; DARPA = Defense Advanced Research Projects Agency.



Figure 1. (b) Midrange TLS solutions available at time of publication. They came out of 11 different countries, 18 different companies, and a research laboratory.

Midrange Terrestrial Laser Scanning Systems (at Time of Publication)

- (a) The RGB Imaging Laser Radar, which came out of the Italian National Agency for New Technologies, Energy and Environment (ENEA) in 2007. The scanner uses three distinct beams (red: 650 nm, green: 532 nm, and blue: 450 nm) in monostatic configuration to create a color point cloud using the laser information alone.
- (b) The BLK360 unit from Leica Geosystems. It is a time-of-flight system that was developed as part of a third pricing tier, which formed around laser scanning as technologies matured.
- (c) The Effortless 3D scanner is also part of this third tier, and like the NCTech unit (m) contains a multibeam time-of-flight Velodyne VLP-16 sensor.
- (d) The phase shift-based Zoller and Fröhlich 5016. It contains a low-light shooting functionality to support the high-dynamic-range camera system inside. It can also use a FLIR thermal imaging camera to combine with the point-cloud information it produces.
- (e) The time-of-flight Stonex scanner from Italy resold by Leica Geosystems under its GeoMax brand.
- (f) The P50 time-of-flight unit from Leica Geosystems. It uses a fiber laser and has a range of up to 1 kilometer. Gregory C. Walsh—who is discussed in part two of this article—suggested the fiber laser inside the unit and designed the high-dynamic-range photography capabilities.
- (g) The time-of-flight Topcon GLS-2000. It is based on the work of Jerry Dimsdale and the team at Voxis – the company Dimsdale founded after leaving Leica Geosystems. Voxis was acquired by Topcon in 2008.
- (h) The Faro Focus S, another phase-shift laser scanner to come out of Germany. Faro laser scanners are discussed in more detail in part two.
- (i) The time-of-flight Trimble TX8. The US-based Trimble entered into midrange TLS via the French company Mensi, which is discussed later.
- (j) The Riegl VZ-400i time-of-flight scanner. It has a range of up to 800 m and is one of four TLS units sold by this Austrian company. Riegl was one of the first companies to sell commercial midrange laser scanners, along with Cyra Technologies (now Leica Geosystems HDS), K²T (later Quantapoint), and Mensi (absorbed into Trimble after acquisition in 2003).
- (k) The Clauss RODEONscan, L.A.M.B.E.R.T., and Smartsan units stemmed from the company's background in panoramic and gimbal-head unit-based photography. Clauss scanners are priced in the same range as (b), (c), and (m).
- (l) is the Sweep kit from Scanse. The Sweep unit came in a build it yourself kit – similar to early personal computers like the ALTAIR 8800. It included low cost computers like Raspberry Pi. The Sweep is – along with SLAM based sensors produced by companies like Velodyne in n) - an indicator that a commodity market had started to solidify around laser scanning technologies by 2016. This is similar to how microchips started to become a commodity item as personal computers evolved, as discussed in more detail in the second part of this article. The RPLidar from Slamtec was another sensor that could be used with the ARM based Raspberry Pi at time of publication.
- (m) The NCTech LASiris incorporates a Velodyne VLP-16 sensor and was primarily positioned for virtual and augmented reality-based applications.
- (n) Velodyne sensors stemmed from the DARPA Grand Challenge. They have become commodity sensors that were being heavily used in mobile mapping and self-driving-car applications by time of publication. Units from Effortless 3D and NCTech demonstrate that these sensors found a use in tripod-based systems as well.
- (o) The RTC360 from Leica Geosystems. This time-of-flight laser scanner saw the return of Gregory C. Walsh as primary system architect for a scanner developed by Leica Geosystems. The last one he had led the development of at the company was the C10 (the final unit to use the green laser system suggested by John Zayhowski to Cyra Technologies). RTC360 contains an inertial measurement unit (IMU), as well as a series of cameras to help track its position in the scene it documents. It also has double laser and imaging features.
- (p and q) The Polaris and ILRIS-3D time-of-flight scanners from Optech. The company and its laser-scanning technology have close ties to the Canadian Space Agency due to past projects developing sensors for space, such as the laser ranging interferometer. The first ILRIS was released commercially in 2000.
- (r) The Opal family of time-of-flight scanners from Neptec also has close ties to the Canadian Space Agency, for the same reason. These scanners also have debris-filtering features built into their functionality.
- (s) The Surphaser range of phase-shift scanners came out of Russia. The company also produces scanners in the submillimeter range.
- (t) The Maptek range of time-of-flight scanners came out of Australia. They primarily stemmed from mining and industrial applications, as well as complementing Maptek software such as I-Site and PointStudio.
- (u) The Trimble X7, released in September 2019. This time of flight-based system is more in line with the Zoller and Fröhlich 5016 (d) and the Leica Geosystems RTC360 (o) – in that it incorporates other sensors like an IMU into its hardware. This makes the registration of point clouds more automated and easier to achieve.
- (v and w) The VS1000 and VS10/VS30 laser scanners from Simai Surveying Instrument in Hefei, China. The VS1000 is a time-of-flight scanner that uses a class 1 905-nm laser to collect information at a range of up to 1000 m. It collects points at a rate of 36,000 points/s and has a global navigation satellite system receiver attached for absolute coordinate retrieval. It uses a Canon 5D Mark II camera to add red, green, and blue information to the scans. The VS10 and VS30 also have a class 1 laser, collecting information at a rate of 250,000 points/s over distances of 15 and 40 m.
- (x) Hi-Target is a company based in Guangzhou, China. Its HS450 scanning unit has been most comprehensively documented by Shan and Toth (2018). It is described as having a 1545-nm class 1 laser, scanning at a rate of 300,000 points/s at a range of 450 m. It also uses an external camera to collect red, green, and blue information.

For a more detailed description of the specifications for each scanner, see their manufacturer specification sheets.

a robot called the Stanford Cart. This took a similar form to the JPL Laser Rangefinder by 1979 (Moravec 1983; Gage 1995). When Moravec moved to CMU in 1981, his work became the reference point for a smaller system called the CMU Rover (Moravec 1983). It also laid the groundwork for the CMU NavLab created in 1984 (Thorpe *et al.* 1987). This university-based laboratory was dedicated to developing semiautonomous and autonomous vehicles using computer vision. PS laser scanners sold as survey tools—from Quantapoint (formerly K²T) and Zoller and Fröhlich (Z+F)—were developed because of NavLab-led initiatives, such as the Franklin scanner (Hancock *et al.* 1998a; K²T 1998). There was also a connection to European efforts, such as the Eureka PROMETHEUS Project, through Dirk Langer. He helped develop the laser module for the Franklin scanner, and brought Christoph Fröhlich to CMU to collaborate because of the laser module he had designed in Germany. The PROMETHEUS Project was the largest research and development project for self-driving cars, running from 1987 to 1995; Langer worked on ultrasonic sensors for it, which was the groundwork for his coming to CMU. Both the Franklin and PROMETHEUS projects marked a collaborative effort between universities and businesses. Car manufacturer's were amongst the companies interested in the technology.

The JPL Laser Rangefinder was soon followed by a PS system funded by DARPA (Gleichman *et al.* 1988; Gage 1995; Roland and Shiman 2002; Nilsson 2010). It was built by ERIM, which had worked with the Bendix Corporation, an American manufacturing and engineering company, to develop Lunar Surface Experiments Packages for NASA as part of the Apollo missions (Latham *et al.* 1969; Hartman 1992). ERIM had also worked extensively on multispectral scanning systems in satellites (Polcyn, Lyzenga and Marinello 1977). This work included tracking the exact distance to a point on the moon's surface to within a few inches using modulated lasers (Knockeart and Wilkinson 1975; Wolfe and Zissis 1978).

The ERIM sensor was built for the ASV in 1982 (Gleichman *et al.* 1988; Gage 1995; Roland and Shiman 2002; Nilsson 2010). As seen in Figure 2, the ASV was a six-legged all-terrain vehicle, which used the same alternating tripod movement seen in insects (Waldron and McGhee 1986; Song and Waldron 1989). The ASV came out of a collaboration between Battelle Columbus Laboratories and Ohio State University, with

the ERIM sensor forming part of its navigation system (Zuk and Dell'Eva 1983; Patterson *et al.* 1984; Waldron and McGhee 1986; Gleichman *et al.* 1988). It was designed to be deployed in environments unsuitable for wheeled vehicles and considered too dangerous to go through on foot (Patterson *et al.* 1984; Waldron and McGhee 1986).

The ASV project was part of a long-term strategy that emerged from US military-funded research, which was directed by an advisory board made up of artificial-intelligence specialists from academia and industry (Stefik 1985; Roland and Shiman 2002). It explored the use of autonomous vehicles for direct combat as well as search and rescue (Patterson *et al.* 1984). It also led to ERIM being chosen for the 1984–1988 ALV program (Gleichman *et al.* 1988). It was this project that demonstrated that PS systems were becoming a viable means of 3D data acquisition. The ALV program also formed part of a broader Strategic Computing Initiative program in digital technologies, which ran from 1983 to 1993 (Roland and Shiman 2002).

Autonomous Land Vehicle

Work began on the ALV project in September 1984, using the experimental ERIM sensor seen in the guidance system for the six-legged ASV (Gleichman *et al.* 1988). It can be seen in Figure 3, which shows an illustration of the ALV from *Popular Science* (Schefter 1985). The sensor was retrofitted to correct known deficiencies, then mounted to a vehicle and sent out to map the DARPA-Martin Marietta ALV test site in Denver, Colo. It was the first of four data-capture missions that provided information to the contractors: CMU, Martin Marietta Aerospace, and Sandia National Laboratories. Each played a key role in future midrange TLS developments by refining both the hardware and the software (Zuk *et al.* 1985; Beyer, Jacobus and Pont 1987; Everett 1995).

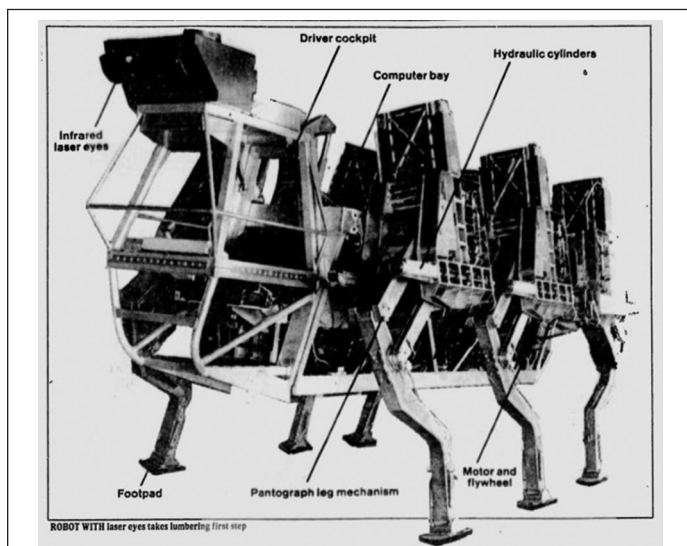


Figure 2. The Adaptive Suspension Vehicle was developed via a collaboration between Battelle Columbus Laboratories and Ohio State University. It used an insect-inspired leg system to navigate terrain. Its vision system also included a laser scanner from the Environmental Research Institute of Michigan (Hoggett 2010).

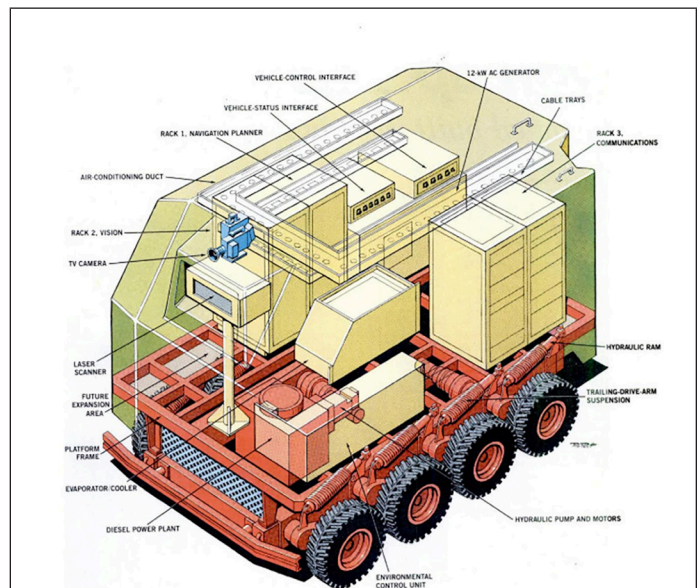


Figure 3. The Autonomous Land Vehicle project introduced several new participants to laser scanning because of the Environmental Research Institute of Michigan sensor. It also brought Takeo Kanade, Pradeep Khosla, and Chuck Thorpe together—through two separate projects managed by Clint Kelly III. The three would later go on to form K²T together at Carnegie Mellon University and release the Franklin scanner as a commercial product. Christoph Fröhlich would also go on to create the Zoller and Fröhlich range of phase shift scanners after working on the Franklin. (Illustration by Ray Pioch. Reproduced by permission from John Schefter, “Look, Ma! No Driver,” *Popular Science* 227: PP. © 1985 by Ray Pioch.)

The ALV program was a turning point for PS laser scanning. ERIM's sensor, which collected sample range data for terrain-modeling purposes, was a catalyst that brought together highly skilled research teams from CMU, Martin Marietta Aerospace, and Sandia National Laboratories (Gleichman *et al.* 1988; Thorpe *et al.* 1991a; Thorpe *et al.* 1991b). Their efforts refined PS based hardware and software solutions, making them more efficient at collecting spatial information. For example, the ALV project led to the development of computers small enough to fit inside a vehicle – in order to process ERIM data in real time. The ALV project also laid the groundwork for sustained research and development through CMU as the computer-vision partner, as well as kept the momentum going for space-driven initiatives like the Space Exploration Initiative (SEI) (Thorpe *et al.* 1991a; Thorpe *et al.* 1991b). PS solutions were on the

cusps of being refined for industrial application via the NavLab initiative by the late 1980s.

Several ALV contractors acquired ERIM scanners in 1985 (Gleichman *et al.* 1988). CMU used its scanner, along with other systems built by Perceptron and Odetics, as part of the NavLab autonomous vehicle initiative that began in 1986 (Kweon *et al.* 1991; Hebert and Krotkov 1992; Kweon and Kanade 1992; Kelly 1994).

In particular, the NavLab explored and refined the application of road vehicles modified for remote driving in urban or city environments. There was even a direct link to the ALV project through Takeo Kanade, Pradeep Khosla, and Chuck Thorpe (Chuck Thorpe, email to author, January 19, 2015). Kanade and Khosla were developing a robotic arm for a project managed by Clint Kelly III, the same person overseeing Thorpe's work on the ALV. Kanade, Khosla, and Thorpe went on to become K²T. The NavLab continued to produce autonomous and semiautonomous vehicles at the time of publication of this article; such vehicles, though, were first designed by the Robotics Institute at CMU and then the CMU NavLab.

PS technologies stemming from this branch of CMU research include those produced by K²T/Quantapoint (USA) and Zoller and Fröhlich (Germany; Hebert and Krotkov 1992; Froehlich, Mettenleiter and Haertl 1997, 1998; Hancock, Hoffman *et al.* 1998; Hancock, Langer *et al.* 1998). iQvolution/Faro (Germany) went on to create its first PS systems in 2003–2004 (Feitz 2003; “iQvolution Announces the iQsun” 2004). By 1998, K²T had released a scanner called the SceneModeler, after the research-driven Franklin in 1997 (Hancock *et al.* 1998b; Cho 2000), and changed its name to Quantapoint in 1999 (“Quantapoint lands \$4 million” 2001). Christoph Fröhlich (Z+F) and Eric Hoffman (K²T/Quantapoint) had also conducted CH scans of the Eastern sculpture niche of the College of Fine Arts at CMU seen in Figure 4 (Froehlich *et al.* 1997, 1998; Hancock *et al.* 1998b). The Franklin system used for these scans was a joint effort between CMU, Z+F, and K²T. It was partly sponsored by the Ben Franklin Technology Center of Southwestern Pennsylvania, from which the Franklin took its name (Hancock *et al.* 1998b). Other contributors included the US Department of Transportation and DARPA under the auspices of the Technology Enhancements for Unmanned Ground Vehicles (UGV) project (Hancock *et al.* 1998b).

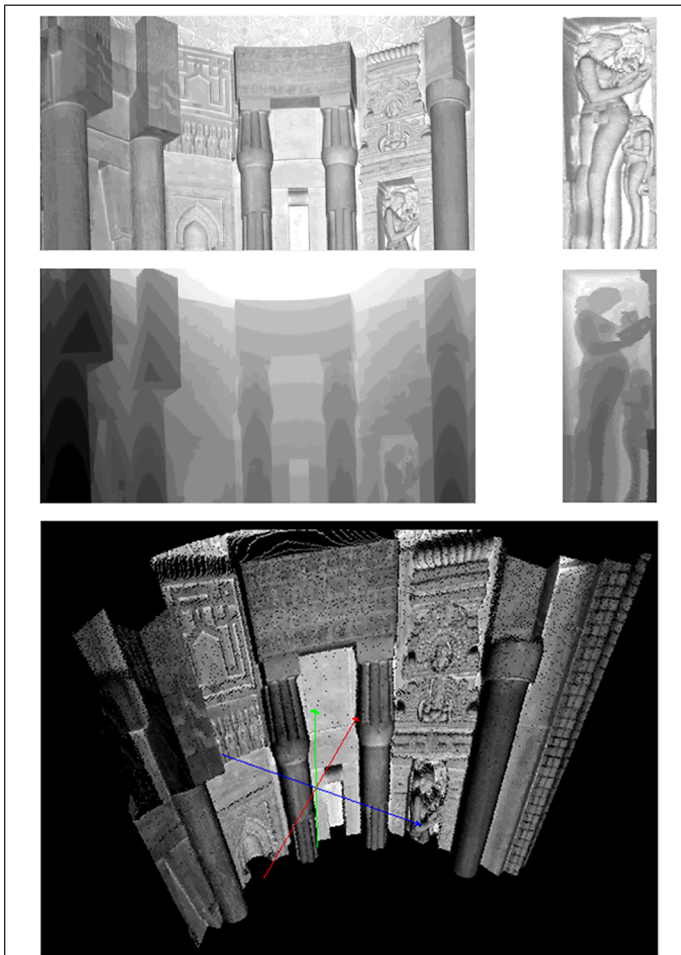


Figure 4. The scans of the Eastern sculpture niche of the College of Fine Arts at Carnegie Mellon University (CMU). The Franklin scanner that produced this data would soon evolve into the SceneModeler range of scanners. It was a tipping point moment for the Robotics Institute at CMU – built on experience gained from exposure to the ERIM sensor; projects like ALV; and collaborative efforts with researchers coming out of the Technical University of Munich (TUM) and the German manufacturing sector. Graduates of TUM like Dirk Langer played a key role in bringing Fröhlich, Mettenleiter, and Haertl to CMU – to work on the Franklin and SceneModeler scanners. All four men went on to become the driving force behind the Imager 5003, the first midrange TLS system from Z+F. In one respect, the story of phase shift-based midrange TLS is one of American and German collaboration and cross-pollination.

When Timing Was Right

The second of the four phases of development for midrange TLS came to its conclusion in the same year as the SEI. This was one of the last space programs, along with European Space Agency initiatives, to advance laser scanning prior to the third, more general era of midrange TLS (Flatscher *et al.* 1999). The SEI was equally as important as the ASV and ALV projects and the NavLab at CMU, because it led to a series of research programs and output that supported the system architectures of hardware released in 1997–1998. This was further driven by advancements encouraged in pumped and Q-switched laser systems, as well as the use of retroreflective targeting systems. The SEI was announced on July 20, 1989, and was part of the 20th-anniversary celebrations for the Apollo 11 moon landing in 1969 (Tchoryk *et al.* 1991; Matthies 1999). Funding was geared toward the exploration of Mars (Tchoryk *et al.* 1991; Zubrin, Baker and Gwynne 1991).

Developments from the SEI included an analysis of active and passive sensors for space docking, planetary landing, and rover navigation via three comprehensive evaluation reports from ERIM (Tchoryk *et al.* 1991). Strategy reports were also provided by Martin Marietta Astronautics, and rover systems were developed by contractors like JPL (Zubrin *et al.* 1991; Matthies 1999). Technologies that made their way into industrial systems, such as those developed by Cyra Technologies, included target solutions based on retroreflective surfaces and

Q-switched or pulsed ToF laser systems (Zubrin *et al.* 1991; Wilson *et al.* 1999; Zayhowski 2010, 2018). For example, passive Q-switching of a laser was incorporated into Cyra Technologies laser scanners via John Zayhowski of the Massachusetts Institute of Technology (MIT) Lincoln Laboratory—a research laboratory with a long history of developing laser systems for space and defense projects (Jelalian 1992; Delaney and Ward 2000; Gschwendtner and Keicher 2000; Grometstein 2011). Zayhowski recognized that a 532-nm green laser using a Q-switched system would fit the specifications given to him by Ben Kacyra and Jerry Dimsdale (seen in Figure 5). It addressed eye-safety issues that could occur in a commercial-based laser scanning unit (Wilson *et al.* 1999; Zayhowski 2010). The diameter of the laser beam and the use of Q-switching provided a means of adjusting the intensity of a laser that was otherwise ideal for survey-based applications. Other requirements needed for the Cyra Technologies based midrange TLS systems—such as the timing circuit that came out of the Department of Energy's Los Alamos National Laboratory—are discussed in more detail in part two of this article. The incentive to commercialize technologies linked to the SEI, which included the JPL rover seen in Figure 1a, came about when manned missions to Mars were abandoned for cheaper, robot-based solutions in 1992 (Hogan 2007).

Policy based influences on turning point moments to come out of the US can be traced back to the Stevenson-Wydler Technology Innovation Act of 1980. This started a chain of legislation passed over the next two decades, which enabled federal laboratories to transfer technologies to non federal entities in the US. The last of note in this time period being the Small Business Technology Transfer Act of 1992.

Best-Fit Solution and Developments in Computing

Midrange TLS is shaped by end-user requirements, the applications around which services or solutions are developed, and trends linked to computer processing. These contributing factors stretch across all phases of its history, be it space-based applications, machine vision for use in autonomous vehicles, or use for “as-built” surveying (explored in more detail in part two of this article). Its transition to industrial uses for “as-built” information collection was also stimulated by the need for safer forms of environmental data collection in environments otherwise hazardous to humans. For example, two of the earliest European and North American companies to seriously explore midrange TLS outside of research applications did so for nuclear and industrial plant applications (Addison and Gaiani 2000; Kacyra *et al.* 1997; Pot, Thibault and Levesque 1997). Cyra Technologies had stemmed from observations made by Ben Kacyra when he worked in nuclear and industrial plants at his engineering company, Cygna (Cheves 2014). Ben envisioned what was later described to the MIT Lincoln Laboratory (by Cyra Technologies) as a solution that could produce something like a “3D Polaroid” of the scene collected. On the other hand, triangulation-based Mensi systems were designed to meet the accuracy, repeatability, and resolution requirements needed to document nuclear power plants owned and managed by Électricité de France (EDF) (Pot *et al.* 1997).

In its commercial period of use, midrange TLS became an answer to problems associated with preexisting computer-aided design (CAD) workflows (Pot *et al.* 1997). This included idealized representations or designs in working environments where not knowing the imperfections in a built environment could cost lives. Midrange TLS was able to easily document an object or scene, enabling CAD drawings or plans to be based on real-time conditions at a level of detail not seen before (Pot *et al.* 1997; Zheng, Lewis and Gethin 1996). Prior to this, CAD-based models ran the risk of being detached from their real-world counterparts. The resolution of information capture was restricted to collecting a series of points on a surface, as opposed to collecting a digital mold of the surface itself. This

was especially the case in environments where everything had known measurements assigned to it, such as pipe-filled spaces in industrial plants.

Enter Mensi

The first Mensi SOISIC scanners were developed around optical triangulation because of the accuracy, repeatability and resolution requirements of their application in industrial power plants in the early 1990s (X. N. Chen *et al.* 2005; Shan and Toth 2008). There the driving force was the speed of data recording in relation to safer working conditions for the end user. A system architecture based around optical triangulation was adopted due to the restrictions associated with PS and ToF systems of the time (X. N. Chen, email to author, October 18, 2013; Fienup 2013). The accuracies and ranges at which information could be collected were not yet to millimeter standard (Pot *et al.* 1997), and computer-based timing and calculation were not yet powerful enough to make ToF and PS viable options for high-resolution documentation and measurement (Wilson *et al.* 1999; Fienup 2013). It was only later, through improvements in integrated timing circuits and algorithm-based noise filtering in the waveform of the laser beam, that PS and ToF became the standard system architectures for midrange TLS (Hebert and Krotkov 1992; Froehlich 1997; Flatscher *et al.* 1999; Wilson *et al.* 1999; Fienup 2013). It is no coincidence that Mensi replaced optical triangulation completely by 2001, with the GS 100 scanner bringing their technology more in line with Cyra Technologies and Riegl systems. (X. N. Chen *et al.* 2005; Shan and Toth 2008). By this time, computer graphics-based processing was becoming powerful enough to make working with point-cloud data easier and more affordable. 3D graphic architectures like RealityEngine from Silicon Graphics (SGI) had evolved into open standard application programming interfaces, such as OpenGL, which also made applications portable between devices (Akeley 1993). In other words, it was now easier for developers to create commercial point cloud-based software because of the continuity such an open standard provided—much in the same way the MIDI file format did for sound engineers and musicians (Loy 1985).

Point Cloud-Based Computing Before Graphics Cards

Earlier examples of midrange TLS, like the ALV project, highlight restrictions caused by computing power available at the time of the Strategic Computing Initiative (Roland and Shiman 2002). Onboard parallel computing—which enabled tasks or complex sets of information to be separated into smaller calculations and processed simultaneously—had to be used in order to work with terrain data in real time (Weems *et al.* 1991; Chuck Thorpe, email to author, Month DD, 2015). It was expensive but necessary due to the fact that the only other hardware capable of doing this was mainframe computers. Parallel processing allowed for the custom manufacture of a computer small enough and light enough to fit inside the ALV (Weems *et al.* 1991; Roland and Shiman 2002).

Point cloud based information became more accessible to a broader population of people because of graphic processing units (GPU). These started to make graphic intensive computer based tasks more affordable to a general consumer by the end of the 1990s. Prior to this, graphic based work carried out on most micro computers (an early term for a personal computer) were handled by the central processing unit and custom chipsets. Even by the mid-1990s, point cloud-based software like Computer Graphics Perception (CGP) was developed on specialist SGI and Sun Microsystems hardware—even though softwares like CGP were designed to run on standard Windows NT machines and Intel 486 processor-based laptops of the time (Kacyra *et al.* 1997). Software and hardware development was,

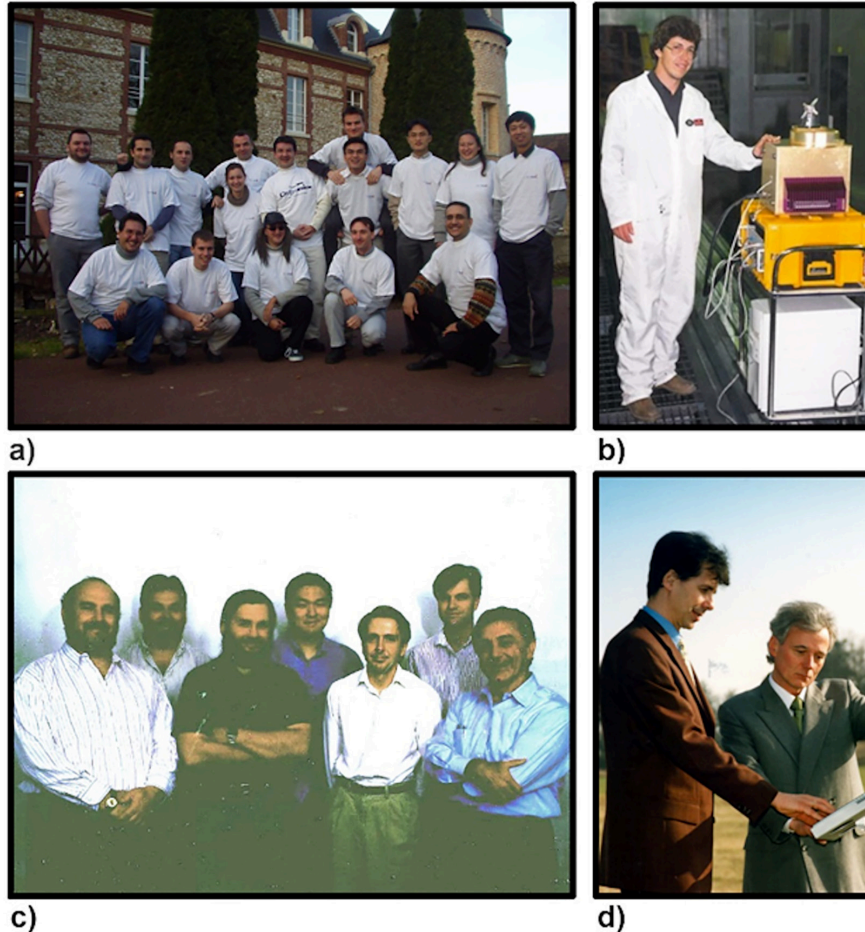


Figure 5. Key teams and some of the people who brought midrange terrestrial laser scanning (TLS) solutions to market in 1997–1998. I would like to thank Xin Chen for the Mensi group photograph, Markus Mettenleiter for the SceneModeler photograph, Reigl USA for the photograph of Andreas Ullrich and Johannes Riegl, and Gregory C. Walsh and Guy Cutting for the Cyra Technologies group photograph. (a) The Mensi development team in France, 2001. Though they would cross over to time-of-flight scanning that same year, their work in laser-based optical triangulation (via the SOISIC scanner) helped to bridge the gap between close and midrange scanning between 1987 and 2001 (this is discussed in part two of this article). Trimble acquired Mensi in 2003. Far right, standing; Xin Chen, Chief Technology Officer of Mensi; far left, kneeling; Omar-Pierre Soubra, who also went on to work for Trimble and then Dassault in director-level marketing roles. (b) Christoph Fröhlich, Dirk Langer, Markus Mettenleiter, and Franz Haertl played a key role in helping to develop the K²T/Quantapoint Franklin and then SceneModeler phase-shift scanners. They went on from their time at the Robotics Institute at Carnegie Mellon University to develop the Z+F range of phase-shift scanners. Four of this German cohort of the phase-shift story graduated from the Technical University of Munich; Haertl had been working on hardware and software development for Z+F's preexisting wire-processing machinery business before transitioning to the emerging midrange TLS side of the business. This photograph was taken by Christoph Fröhlich and shows Markus Mettenleiter with an early version of the SceneModeler. It is seen to contain all of the components that would go into commercial midrange TLS (discussed in part two of this article). The big yellow box contains a signal processing unit. This and the computer were replaced in later versions of the SceneModeler by two smaller blue boxes that contained smaller single and computer hardware. Leica Geosystems sold Zoller and Fröhlich laser scanners under an original equipment manufacturers (OEM) agreement from 2005 to 2012. (c) Cyra Technologies was formed by Ben Kacyra and Jerry Dimsdale in California in 1993. The photograph shows Chief Technology Officer Jerry Dimsdale (front left), Chris Thewalt (back left), Jonathan Kung (back middle), and chief executive officer Ben Kacyra (front right). Cyra Technologies combined a 532-nm pulsed green laser from the Massachusetts Institute of Technology Laboratory with a timing circuit developed at Los Alamos National Laboratory to create its Cyrax scanners. The company also played a key role in helping form a stable market around midrange TLS, especially after its acquisition by Leica Geosystems in late 2000. Dimsdale, after the acquisition of his later company Voxis, went on to create another generation of midrange TLS systems that became the GLS series of scanners for Topcon. Kacyra went on to form the cultural heritage-based nonprofit CyArk (discussed in more detail in part two of this article). (d) Riegl is an Austrian company that brought a time-of-flight midrange TLS system to market in 1997–1998. This photograph shows Andreas Ullrich (right), who went on to become Chief Technology Officer at Riegl, next to the company's founder and namesake, Johannes Riegl. Ullrich played a fundamental role in the development of the system architecture for the Riegl LMS-Z160/Z210 scanners. They were developed out of an European Space Agency funded project exploring landing shuttle sensors in the 1990s. Both Johannes Riegl and Andreas Ullrich graduated from the Vienna University of Technology (VUT). Dr. Riegl carried out long terms research at VUT on avalanche pulse generators (nothing to do with snow and ice) prior to forming the company in 1978. Ullrich completed a PhD thesis based on high-resolution optical Doppler radar. By the time this article was published, Riegl had evolved into a company with a long history in the development of tripod-based and simultaneous and localized mapping (SLAM) laser scanning systems (discussed in more detail in part two of this article).

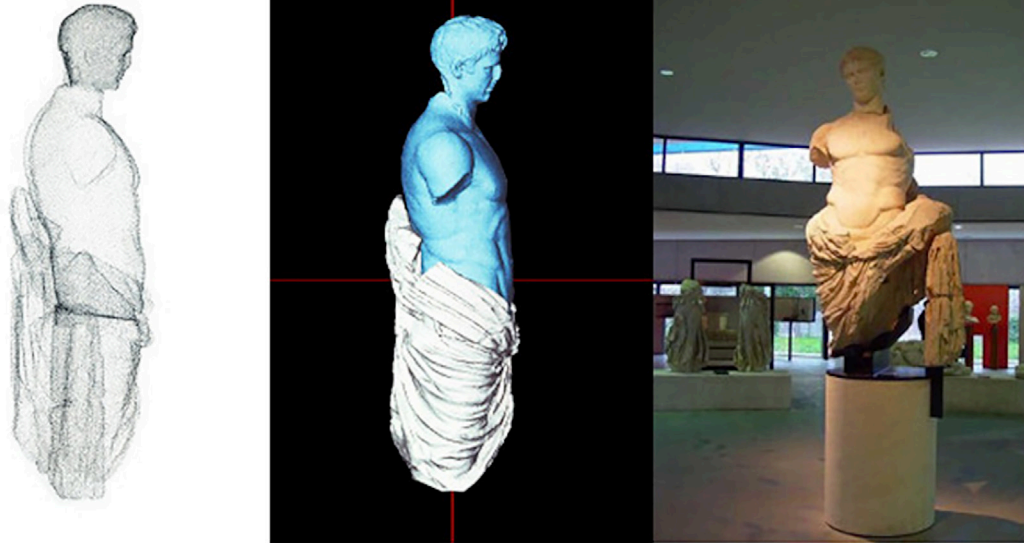


Figure 6. The documentation of a statue of Emperor Augustus was one of many to come out of the collaboration between Mensi and the Coignard family in the 1990s. This example was one of the earliest attempts at creating a digital surrogate from an artifact. The point cloud (left) was used to generate a solid mesh (middle), which was then used to create a precise replica of the statue (right).

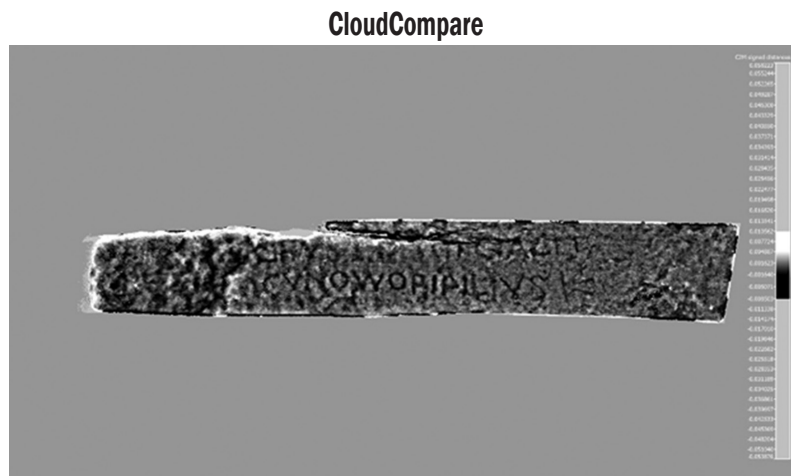


Figure 7. The example above is a Poisson shading of inscribed stone surface from the Tristan Stone in Cornwall, UK. Scan data was processed in CloudCompare and the test was carried out by George Bevan, Queens University, Canada. It built on previous work published by Adam P. Spring and Caradoc Peters outlined in the *Journal of Archaeological Science* article (Spring and Peters 2014). Developing a low-cost 3D imaging solution for inscribed stone surface analysis. The on site collection of data is also seen in Figure 3 of part two of this article.

CloudCompare was developed as part of a PhD thesis between 2004-2007 by Daniel Girardeau-Montaut. Girardeau-Montaut was working between Telecom ParisTech and EDF Research and Development (R&D) at that time. The software was initially geared toward industrial plant applications for "as-built" monitoring. This included the reporting and simulation of maintenance operations. However, previous mid-range TLS experience gained in organizations like EDF through MENSİ - which included the heritage preservation work of EDF engineer Guillaume Thibault - took its development in other directions as well. For example, both the ambient occlusion shader (also referred to as 2D skydome) and unroll functions were implemented by Girardeau-Montaut and Florent Duguet as part of scanning work done on the Omphalos in the museum at Delphi (Duguet *et al.* 2004; Thibault and Martinez 2007; Tarini *et al.* 2003). They represented features being implemented into software because of CH carried by EDF. The scans themselves were also inspired by Marc Levoy's research group – more specifically the work that had been done as part of the Digital Michelangelo Project (INSIGHT 2018). Kevin Cain, who is discussed further in the sections **Cultural Heritage as Marketing (Second to Third Phase)** and **The Non-profit Corporations (Third Phase)** in Part two of this article, was also involved in the project.

Along with former Chief Technology Officer (CTO) of MENSİ, Xin Chen, Guillaume - who supervised the development of CloudCompare – was instrumental in the development of the SOISIC scanners. Included in this development was the 3Dipsos software, as well as his involvement with both the Coignard family and CH projects discussed later in part two. CloudCompare uses an octree file structure that subdivides point cloud data into eight sections within the same coordinate system. This reduces the computational power needed to work with large datasets, such as scandata, by spreading tasks between eight sections.

in other words, still tethered to expensive custom hardware to make point cloud-based products work for an emerging user base. By 1999, a second wave of software came about due to the growing use of computers in the workplace. It was centered on client server-based workflows (Frei *et al.* 2005). Software like Cyclone from Leica Geosystems, developed to be the successor to CGP by Cyra Technologies, is one such example from this period.

It was only in the 2000s that computer graphics became more affordable, because of companies like AMD and Nvidia. A substantial price and performance gap had existed between general and high-performance computing prior to this. For example, manufacturers like IBM viewed personal computing as the preserve of scientific or business machine applications (DeCuir and Nicholson 2016). The functionality and screen displays of personal computers were generally geared toward productivity software like spreadsheets and word-processing packages; they were not primarily made to be used for sophisticated or visually complex graphics. Consumer applications that pushed those boundaries had their roots in entertainment or creative computing activities, such as video games and audio video production.

The Point Cloud

In the 1980s, the point cloud was revisited as an alternative to surface modeling, which had become a technique commonly used in computer graphics-based disciplines (Levoy and Whitted 1985; Levoy 2007). Earlier work on “virtual images” in the field of holography, however, had demonstrated the potential for documenting and presenting a scene in 3D using light-based techniques. The train examples generated by Leith and Upatnieks (1964), one of which is shown in Figure 1a, are a famous instance of this earlier work. CAD users started to realize that solid models made drafting and design processes more efficient—they could present actual surface conditions as opposed to working from plan drawings (Levoy and Whitted 1985; Besl and McKay 1992; Kacyra *et al.* 1997; Addison and Gaiani 2000; Dekeyser *et al.* 2003). At the same time, the potential to use personal computers for graphic-intensive tasks was also starting to emerge. For example, Amiga computers equipped with the Video Toaster from NewTek laid the foundation for reasonably priced ray-tracing software like LightWave 3D (DeCuir and Nicholson 2016). There was even a Scannerless Range Imager developed at Sandia National Laboratories to run on the Amiga (Sackos *et al.* 1998). Digital terrain modeling and height mapping had also become more accessible to a general audience. Design packages like Alias on SGI machines and fractal landscape generators like Scene Generator were bridging a gap that would later be filled by point clouds (Jaenisch *et al.* 1994; Campbell 1997).

Point clouds provided a template from which scenes and objects could be modeled. From these point clouds, the “as-built” or “as-is” conditions of a scene could be used as the baseline data for survey-driven projects. This approach was fundamental to the CH-based workflows used by the Coignard family (father and two sons) and EDF engineers like Guillaume Thibault. This early “as-built” based work—as applied to artifacts and cultural heritage sites—is explored in more detail in part two (Bommelaer and Albouy 1997; Coignard 1999; Thibault and Martinez 2007). Like the pixels of a photograph, which have an x- and a y-coordinate, a point cloud is used to document an environment with coordinates, except in three dimensions (Levoy and Whitted 1985; Levoy 2007). The z-coordinates give depth to the scene collected. Other information, like height-field data and surface reflectance, can also be retrieved (Nitzan, Brain and Duda 1977; Y. Chen and Medioni 1992). One of the key outcomes of the relationship between Mensi and EDF that

remains in use is CloudCompare – as discussed in more detail in Figure 7 (Daniel Girardeau-Montaut, email to author, April 15, 2012). This EDF-funded point-cloud software became open source in 2009 (Girardeau-Montaut, n.d).

Summary

Part one of this article ends at a point where midrange TLS information starts to be collected to known accuracies, repeatability of results and standards of resolution necessary for “as-built” documentation. Otherwise known as a theoretical camera model in 3D imaging, these types of considerations enable an object or scene to be documented within millimeters and centimeters over a known distance. Examples for repeatability of results within the context of midrange TLS include a) the ability to rescan an object or site with the same instrument and workflow to compare to previous results or baseline and b) features of the system architecture of the instrument, such as the number of times the signal of points returning to the scanner can be sampled to help improve data quality.

Providing an historical perspective for development helps the potential user of midrange TLS to better understand it in a number of ways. First, it helps provide context to what might otherwise be seen as a black box technology - where the knowledge economy mainly resides with the manufacturers of the technology. Second, it helps to better contextualize how and why relative navigation remains at the core of midrange TLS technologies - because of early space and defense applications identified through agencies like NASA and funded by DARPA. Third, survey based solutions used today are part of a lineage that can be traced back to vehicle based solutions. In other words, the technology made the transition to tripod based applications. It did not start out as a tripod based survey method. Fourth, the development of midrange TLS was closely aligned with and reactionary to broader developments in personal computing and microelectronics at time of publication. Fifth, a thread running throughout the history of midrange TLS is the need for applied research and development based on detailed information retrieval in environments otherwise hazardous to humans. For example, it is a common point of reference between the foundation companies for commercial use - discussed in more detail in part two.

Acknowledgements

The author would like to thank the many leaders in their field who enthusiastically waited for these articles to make it to publication. This includes core people from Cyra Technologies, K²T, Mensi and Reigl. Both articles pay homage to them and many other pioneers in 3D imaging.

The articles are dedicated to Rebecca, Fonzie, Harvey, Poppy and Willow. This article was made open access by Remotely Interested LLC.

References

- Addison, A. C. and M. Gaiani. 2000. Virtualized architectural heritage: New tools and techniques. *IEEE MultiMedia* 7 (2):26–31.
- Akeley, K. 1993. RealityEngine graphics. Pages 109–116 in *SIGGRAPH '93: Proceedings of the 20th Annual Conference on Computer Graphics and Interactive Techniques*, held in Anaheim, Calif., 2–6 August 1993. Edited by M. C. Whitted. New York: Association for Computing Machinery.
- Amann, M.-C., T. Bosch, M. Lescure, R. Myllylae and M. Rioux. 2001. Laser ranging: A critical review of usual techniques for distance measurement. *Optical Engineering* 40 (1):10–19.
- Besl, P. J. 1988. Active, optical range imaging sensors. *Machine Vision and Applications* 1 (2):127–152.

- Besl, P. J. and N. D. McKay. 1992. A method for registration of 3-D shapes. *IEEE Transactions on Pattern Analysis and Machine Intelligence* 14 (2):239–256.
- Beyer, J., C. Jacobus and F. Pont. 1987. Autonomous vehicle guidance using laser range imagery. Pages 34–43 in *Robotics and IECON 87 Conferences for the International Society for Optics and Photonics*, held in City, St., DD Month YYYY. Edited by J. Editor. City, St.: Publisher.
- Bommelaer, J.-F. and M. Albouy. 1997. *Marmaria: le sanctuaire d'Athéna à Delphes*. Paris: Ecole française d'Athènes.
- Campbell, B. D. 1997. "3-D Collaborative Multiuser Worlds for the Internet." MS thesis, Rensselaer Polytechnic Institute/University of Washington. <http://bdcampbell.net/articles/bdc_masters.pdf> Accessed 1 October 2018.
- Chen, X. N., Q. Xia, Q., S. H. Zhang and Y. Zhou. 2005. 3D laser scanner system for surveying and engineering. Pages 14–16 in *Proceedings of the ISPRS Joint Conference: 3rd International Symposium Remote Sensing and Data Fusion Over Urban Areas (URBAN 2005) and 5th International Symposium Remote Sensing of Urban Areas (URS 2005)*, held in Tempe, Ariz., 14–16 March 2005. Edited by M. Moeller and E. Wentz. City, St.: Publisher.
- Chen, Y. and G. Medioni. 1992. Object modelling by registration of multiple range images. *Image and Vision Computing* 10 (3):145–155.
- Cheves, M. 2014. Monumental challenge: Ben Kacyra's remarkable perseverance. *American Surveyor* 11 (11):18–22.
- Cho, Y. 2000. "Human-Assisted Rapid Workspace Modeling for Construction Equipment Operations." PhD diss., The University of Texas at Austin.
- Coignard, B. 1999. Rapport de Restauration du Colosse d'Alexandrie. <<http://www.sculpt.fr/RESTAURATION/PDF/Anastyllose-du-colosse-d-Alexandrie.pdf>> Accessed 13 May 2015.
- DeCuir, J. and R. H. Nicholson. 2016. The Amiga: A hardware engineering story—advancing multimedia computing capability. *IEEE Consumer Electronics Magazine* 5 (4):57–67.
- Dekeyser, F., F. Gaspard, L. de Luca, M. Florenzano, X. Chen and P. Leray. 2003. Cultural heritage recording with laser scanning, computer vision and exploitation of architectural rules. *International Archives of the Photogrammetry, Remote Sensing and Spatial Information Sciences* 34 (5/W12):145–149.
- Delaney, W. P. and W. W. Ward. 2000. Radar development at Lincoln Laboratory: An overview of the first fifty years. *Lincoln Laboratory Journal* 12 (2):147–166.
- Duguet, F., G. Drettakis, D. Girardeau-Montaut, J.-L. Martinez and F. Schmitt. 2004. A point-based approach for capture, display and illustration of very complex archaeological artefacts. Pages 105–114 in *VAST 2004: The 5th International Symposium on Virtual Reality, Archaeology and Intelligent Cultural Heritage*, held in Brussels, Belgium, 7–10 December 2004. Edited by Y. Chrysantou, K. Cain, N. Silberman and F. Niccolucci. Goslar, Germany: Eurographics Association.
- Everett, H. R. 1995. *Sensors for Mobile Robots: Theory and Application*. Boca Raton, Fla.: CRC Press.
- Feitz, K. 2003. iQvolution Introduces First Modular Design 3D Laser Scanner with Built-In PC. <<https://www.prweb.com/releases/2003/10/prweb82297.htm>> Accessed 13 May 2015.
- Fienup, J. R. 2013. Phase retrieval algorithms: A personal tour. *Applied Optics* 52 (1):45–56.
- Flatscher, R., A. Ullrich, G. Paar and G.-J. Ulbrich. 1999. Active surface imaging system (ASIS). Pages 379–384 in *Proceedings of the Fifth International Symposium, Artificial Intelligence, Robotics and Automation in Space*, held in Noordwijk, the Netherlands, 1–3 June 1999. Edited by M. Perry. Paris: European Space Agency.
- Frei, E., Kung, J. and Bukowski, R. 2005. High-definition surveying (HDS): a new era in reality capture. *International Archives of Photogrammetry, Remote Sensing and Spatial Information Sciences*, 36, pp. 204–208.
- Froehlich, C., M. Mettenleiter and F. Haertl. 1997. Active laser radar (lidar) for measurement of corresponding height and reflectance images. *Proceedings of SPIE* 3101: 292–305.
- Froehlich, C., M. Mettenleiter and F. Haertl. 1998. Imaging laser radar for high-speed monitoring of the environment. *Proceedings of SPIE* 3207: 50–64.
- Gage, D. W. 1995. UGV history 101: A brief history of unmanned ground vehicle (UGV) development efforts. *Unmanned Systems Magazine* 13 (3):9–32.
- Girardeau-Montaut, D. n.d. CloudCompare. <<https://www.danielgm.net/cc/>> Accessed 14 September 2018.
- Gleichman, K., L. Harmon, T. Miciek, C. Miller and D. Zuk. 1988. *Sensor Support for the DARPA Autonomous Land Vehicle Program*. Publication No. ERIM-176600-12-F. City, St.: Publisher.
- Grometstein, A. A., ed. 2011. *MIT Lincoln Laboratory, Technology in Support of National Security*. Lexington, Mass.: Lincoln Laboratory, Massachusetts Institute of Technology. <https://www.ll.mit.edu/sites/default/files/other/doc/2018-04/MIT_Lincoln_Laboratory_history_book.pdf> Accessed 14 May 2015.
- Gschwendtner, A. G. and W. E. Keicher. 2000. Development of coherent laser radar at Lincoln Laboratory. *Lincoln Laboratory Journal* 12 (2):383–396.
- Hancock, J., E. Hoffman, R. M. Sullivan, D. Ingimarson, D. Langer and M. Hebert. 1998a. High-performance laser range scanner. *Proceedings of SPIE* 3207: 40–49.
- Hancock, J., D. Langer, M. Hebert, R. Sullivan, D. Ingimarson, E. Hoffman, M. Mettenleiter and C. Froehlich. 1998b. Active laser radar for high-performance measurements. Pages 1465–1470 in *Proceedings, 1998 IEEE International Conference on Robotics and Automation*, held in Leuven, Belgium, 16–20 May 1998. Edited by J. Editor. Piscataway, N.J.: Institute of Electrical and Electronics Engineers.
- Hartman, H. L., ed. 1992. *SME Mining Engineering Handbook, Vol. 1*. Littleton, Colo.: Society for Mining, Metallurgy, and Exploration.
- Hebert, M. and E. Krotkov. 1992. 3D measurements from imaging laser radars: How good are they? *Image and Vision Computing* 10 (3):170–178.
- Hogan, T. 2007. Lessons learned from the Space Exploration Initiative. *News & Notes* (24) 4: 1–2, 4–5. <<http://history.nasa.gov/nltr24-4.pdf>> Accessed 17 November 2013.
- Hoggett, R. 2010. 1984 – OSU ASV (Adaptive Suspension Vehicle) – Waldron & McGhee (American). <<http://cyberneticzoo.com/walking-machines/1984-osu-asv-adaptive-suspension-vehicle-mcghee-american/>> Accessed 24 September 2018.
- INSIGHT. 2018. Rebuilding an Acanthus Column in Delphi. <<https://hal.archives-ouvertes.fr/hal-01774309/document>> Accessed 27 September 2018.
- iQvolution Announces the iQsun 880 -HE80 3D Laser Scanner. 2004, December 20. <<https://www.pobonline.com/articles/85212-iqvolution-announces-the-iqsun-880-he80-3d-laser-scanner>> Accessed 12 February 2015.
- Jaenisch, H. M., J. W. Handley, J. Scoggins and M. P. Carroll. 1994. Simulating landscapes using an FFT-based fractal filter. *Proceedings of SPIE* 2223: 434–444.
- Jelalian, A. V. 1992. *Laser Radar Systems*. London: Artech House.
- K²T. 1998. <https://web.archive.org/web/19980127210625fw_/http://www.k2t.com/franklin.HTM> Accessed 14 June 2017.
- Kacyra, B. K., J. Dimsdale, M. Brunhart, J. A. Kung and C. R. Thewalt. 1997. Integrated system for imaging and modeling three-dimensional objects. WIPO Patent WO/1997/040342.
- Kelly, A. 1994. *Concept Design of a Scanning Laser Rangefinder for Autonomous Vehicles*. Publication No. CMU-RI-TR-94-21. Pittsburgh, Penn.: Carnegie Mellon University Robotics Institute.
- Knockeart, R. P. and J. R. Wilkinson. 1975. System for converting modulated signals to squarewave outputs. US Patent 3,860,794.
- Kweon, I. S., R. Hoffman and E. Krotkov. 1991. *Experimental Characterization of the Perceptron Laser Rangefinder*. Publication No. CMU-RI-TR-91-1. Pittsburgh, Penn.: Carnegie Mellon University Robotics Institute.
- Kweon, I. S. and T. Kanade. 1992. High-resolution terrain map from multiple sensor data. *IEEE Transactions on Pattern Analysis and Machine Intelligence* 14 (2):278–292.
- Latham, G., M. Ewing, F. Press and G. Sutton. 1969. The Apollo Passive Seismic Experiment. *Science* 165 (3890):241–250.
- Leith, E. N. and J. Upatnieks. 1964. Wavefront reconstruction with diffused illumination and three-dimensional objects. *Journal of the Optical Society of America* 54 (11):1295–1301.

- Levoy, M. 2007. The early history of point-based graphics. In *Point-Based Graphics*, edited by M. Gross and H. Pfister, 9–18. Amsterdam: Morgan Kaufmann. <<http://graphics.stanford.edu/papers/points/levoy-pointbook-ch2.pdf>> Accessed 17 July 2017.
- Levoy, M. and T. Whitted. 1985. *The Use of Points as a Display Primitive*. Technical Report 85-022. Chapel Hill, N.C.: University of North Carolina, Department of Computer Science. <<http://citeseerx.ist.psu.edu/viewdoc/download?doi=10.1.1.89.1180&rep=rep1&type=pdf>> Accessed 17 July 2017.
- Lewis, R. A. and A. R. Johnston. 1977. A scanning laser rangefinder for a robotic vehicle. Pages 762–768 in *IJCAI'77: Proceedings of the 5th International Joint Conference on Artificial Intelligence*, held in Cambridge, Mass., 22–25 August 1977. Edited by J. Editor. San Francisco: Morgan Kaufmann.
- Loy, G. 1985. Musicians make a standard: The MIDI phenomenon. *Computer Music Journal* 9 (4):8–26.
- Matthies, L. H. 1999. Robotic perception for autonomous navigation of Mars rovers. In *Frontiers of Engineering: Reports on Leading Edge Engineering from the 1998 NAE Symposium on Frontiers of Engineering*, edited by J. Editor, 99–105. Washington, DC: National Academies Press.
- Moravec, H. P. 1983. The Stanford Cart and CMU Rover. *Proceedings of the IEEE* 71 (7):872–884.
- Nilsson, N. J. 1969. A Mobius automaton: An application of artificial intelligence techniques. Pages 509–520 in *Proceedings of the First International Joint Conference on Artificial Intelligence*, held in Washington, DC, 7–9 May 1969. Edited by J. Editor. San Francisco: Morgan Kaufmann.
- Nilsson, N. J. 1984. *Shakey the Robot*. Technical Note 323. Menlo Park, Calif.: SRI International.
- Nilsson, N. J. 2010. *The Quest for Artificial Intelligence: A History of Ideas and Achievements*. Cambridge, UK: Cambridge University Press.
- Nitzan, D., A. E. Brain and R. O. Duda. 1977. The measurement and use of registered reflectance and range data in scene analysis. *Proceedings of the IEEE* 65 (2):206–220.
- Patterson, M. R., J. J. Reidy and R. C. Rudolph. 1984. *Guidance and Actuation Systems for an Adaptive-Suspension Vehicle: Final Technical Report*. Publication AD-A139111. City, St.: Publisher.
- Polcyn, F. C., D. R. Lyzenga and E. I. Marinello. 1977. *Investigation of Intertidal Zone Mapping by Multispectral Scanner Techniques*. Ann Arbor, Mich.: Environmental Research Institute of Michigan.
- Pot, J., G. Thibault and P. Levesque. 1997. Techniques for CAD reconstruction of “as-built” environments and application to preparing for dismantling of plants. *Nuclear Engineering and Design* 178 (1):135–143.
- Quantapoint lands \$4 million from Mellon Ventures. 2001, August 28. *Pittsburgh Business Times*. <<https://www.bizjournals.com/pittsburgh/stories/2001/08/27/daily12.html>> Accessed 4 December 2016.
- Roland, A. and P. Shiman. 2002. *Strategic Computing: DARPA and the Quest for Machine Intelligence, 1983–1993*. Cambridge, Mass.: The MIT Press.
- Sackos, J.T., Nellums, R.O., Lebien, S.M., Diegert, C.F. Grantham, J.W. and Monson, T. 1998. Low-Cost, High-Resolution, Video-Rate Imaging Optical Radar. O.S.T.I., U.S. Department of Energy.
- Scheffer, J. 1985. Look, Ma! No driver. *Popular Science* 227 (4):94, 114–116.
- Shakey. 2018. <<http://www.computerhistory.org/revolution/artificial-intelligence-robotics/13/289>> Accessed 15 January 2018.
- Shakey Images. n.d. <<http://www.ai.sri.com/shakey/images.php>> Accessed 14 June 2017.
- Shan, J. and C. K. Toth, eds. 2008. *Topographic Laser Ranging and Scanning: Principles and Processing*. Boca Raton, Fla.: CRC Press.
- Shan, J. and Toth, C. K. second eds. 2018. *Topographic Laser Ranging and Scanning: Principles and Processing*. Boca Raton, Fla.: CRC Press.
- Shirai, Y. 1972. Recognition of polyhedrons with a range finder. *Pattern Recognition* 4 (3):243–244, IN1, 245–250.
- Song, S.-M. and K. J. Waldron. 1989. *Machines That Walk: The Adaptive Suspension Vehicle*. Cambridge, Mass.: The MIT Press.
- Spring, A. P. and C. Peters. 2014. Developing a low cost 3D imaging solution for inscribed stone surface analysis. *Journal of Archaeological Science* 52: 97–107.
- Stefik, M. 1985. Strategic computing at DARPA: Overview and assessment. *Communication of the ACM* 28: 690–704.
- Tarini, M., P. Cignoni and R. Scopigno. 2003. Visibility based methods and assessment for detail-recovery. Pages 457–464 in *IEEE Visualization 2003*, held in Seattle, Wash., 19–24 October 2003. Edited by J. Editor. Los Alamitos, Calif.: IEEE Computer Society.
- Tchoryk Jr, P., K. W. Gleichman, D. C. Carmer, Y. Morita, M. Trichel and R. K. Gilbert. 1991. Passive and active sensors for autonomous space applications. *Proceedings of SPIE* 1479: 164–182.
- Thibault, G. and J.-L. Martinez. 2007. La reconstitution de la colonne des danseuses de Delphes. Pages 231–238 in *Actes du colloque Virtual Retrospect 2007*, held in Pessac, France, 14–16 November 2007. Edited by R. Vergnieux and C. Delevoise. Bordeaux, France: Editions Ausonius. <<https://hal.archives-ouvertes.fr/hal-01774309/document>> Accessed 14 June 2018.
- Thorpe, C., M. Hebert, T. Kanade, S. Shafer and the Strategic Computing Vision Lab. 1987. Vision and navigation for the Carnegie-Mellon NavLab. *Annual Review of Computer Science* 2: 521–556.
- Thorpe, C., Hebert, M., Kanade, T., and Shafer, S. 1991a. Toward Autonomous Driving: The CMU Navlab. Part I: Perception. *IEEE Expert*, 6 (4): 31–42.
- Thorpe, C., Hebert, M., Kanade, T., and Shafer, S. 1991b. Toward Autonomous Driving: The CMU Navlab. Part II: System and Architecture. *IEEE Expert*, 6 (4): 44–52.
- Waldron, K. and R. McGhee. 1986. The Adaptive Suspension Vehicle. *IEEE Control Systems Magazine* 6 (6):7–12.
- Weems, C. C., C. Brown, J. A. Webb, T. Poggio and J. R. Kender. 1991. Parallel processing in the DARPA strategic computing vision program. *IEEE Expert* 6 (5):23–38.
- Wilson, K., C. Smith, D. Neagley, B. Kacyra, J. Dimsdale and J. J. Zayhowski. 1999. Cyrax: A portable three-dimensional laser-mapping and imaging system. In *1997–1998 Physics Division Progress Report*, Los Alamos National Laboratory Report LA-13606-PR, edited by J. Editor, 76–79. City, St.: Publisher.
- Wolfe, W. L. and G. J. Zissis, eds. 1978. *The Infrared Handbook*. Ann Arbor, Mich.: Environmental Research Institute of Michigan.
- Zayhowski, J.J. 2010. Passively Q-Switched Microchip Lasers – A Historical Perspective, *The Review of Laser Engineering* 26 (12): 841-846.
- Zayhowski, J. J. 2018. Microchip lasers. In *Encyclopedia of Modern Optics*, 2nd ed., edited by R. Guenther and D. Steel, vol. 2, 415–423. Amsterdam: Elsevier.
- Zheng, Y., R. W. Lewis and D. T. Gethin. 1996. Three-dimensional unstructured mesh generation: Part 1. Fundamental aspects of triangulation and point creation. *Computing Methods in Applied Mechanics and Engineering* 134 (3–4):249–268.
- Zubrin, R. M., D. A. Baker and O. Gwynne. 1991. *Mars Direct: A Simple, Robust, and Cost Effective Architecture for the Space Exploration Initiative*. Publication AIAA-91-0328. Reston, Va.: American Institute of Aeronautics and Astronautics. <<https://pdfs.semanticscholar.org/644f/3a1eb49cbef7b7e2ef987ab3f6389d822ee.pdf>> Accessed 14 October 2013.
- Zuk, D. M., and M. L. Dell’Eva. 1983. *Three-Dimensional Vision System for the Adaptive Suspension Vehicle*. Final Report Number 170400-3-F. Washington, DC: Defense Supply Service.
- Zuk, D., F. Pont, R. Franklin and V. Larrowe. 1985. A System for Autonomous Land Navigation. Technical Report IR-85-540. Ann Arbor, Mich.: Environmental Research Institute of Michigan.

WHO'S WHO IN ASPRS

BOARD OF DIRECTORS

BOARD OFFICERS

President

Jeff Lovin
Woolpert

President-Elect

Jason M. Stoker, Ph.D.
U.S. Geological Survey

Vice President

Christopher Parrish, Ph.D.
Oregon State University

Past President

Thomas Jordan, Ph.D.
University of Georgia

Treasurer

Stewart Walker, Ph.D.

Secretary

Lorraine B. Amenda, PLS, CP

BOARD MEMBERS

Sustaining Members Council – 2021

Chair: Joe Cantz
www.asprs.org/About-Us/Sustaining-Members-Council.html

Early-Career Professionals Council – 2021

Chair: Bobby Arlen
Vice Chair: Melissa Martin

Region Officers Council – 2021

Chair: Lorraine B. Amenda, PLS, CP
Vice Chair: Demetrio Zourarakas

Student Advisory Council – 2021

Chair: Youssef Kaddoura
<http://www.asprs.org/Students/Student-Advisory-Council.html>

Technical Division Directors Council – 2021

Chair: Bandana Kar, Ph.D.
Vice Chair: Denise G. Theunissen

TECHNICAL DIVISION OFFICERS

Geographic Information Systems Division – 2021

Director: Xan Fredericks
Assistant Director: Denise G. Theunissen
www.asprs.org/Divisions/GIS-Division.html

Lidar Division – 2022

Director: Joshua Nimetz, CMS
Assistant Director: Ajit Sampath
www.asprs.org/Divisions/Lidar-Division.html

Photogrammetric Applications Division – 2022

Director: Kurt Rogers
Assistant Director: Benjamin Wilkinson
www.asprs.org/Divisions/Photogrammetric-Applications-Division.html

Primary Data Acquisition Division – 2021

Director: Jon Christopherson
Assistant Director: J. Chris Ogier
www.asprs.org/Divisions/Primary-Data-Aquisition-Division.html

Professional Practice Division – 2022

Director: Harold W. Rempel, III, CP
Assistant Director: Bill Swope
www.asprs.org/Divisions/Professional-Practice-Division.html

Remote Sensing Applications Division – 2022

Director: Raechel A. Portelli, Ph.D.
Assistant Director: Amr Abd-Elrahman
www.asprs.org/Divisions/Remote-Sensing-Applications-Division.html

Unmanned Autonomous Systems (UAS) – 2022

Director: Megan Ritelli, Ph.D.
Assistant Director: Dan Hubert

REGION PRESIDENTS

Alaska Region

David Parret
<http://www.asprsalaska.org/>

Cascadia Region

Robert Hairston-Porter

Eastern Great Lakes Region

Shawana P. Johnson, Ph.D, GISP
<http://egl.asprs.org/>

Florida Region

Xan Fredericks
<http://florida.asprs.org/>

Heartland Region

Whit Lynn
<http://heartland.asprs.org/>

Mid-South Region

<https://www.asprs.org/all-regions/mid-south.html>

Northeast Region

(representing the merger of The New England and Central New York Regions)
Trevis Gigliotti, Interim President

North Atlantic Region

Richard W. Carlson, Jr., P.L.S., C.P.
<http://natlantic.asprs.org/>

Pacific Southwest Region

Omar G. Mora
<https://pswasprs.org/>

Potomac Region

Dave Lasko
<http://www.asprspotomac.org/>

Rocky Mountain Region

<http://www.asprs-rmr.org/>

Western Great Lakes Region

Brandon Krumwiede
<http://wgl.asprs.org/>

Improved Crop Classification with Rotation Knowledge using Sentinel-1 and -2 Time Series

Sébastien Giordano, Simon Bailly, Loïc Landrieu, and Nesrine Chehata

Abstract

Leveraging the recent availability of accurate, frequent, and multimodal (radar and optical) Sentinel-1 and -2 acquisitions, this paper investigates the automation of land parcel identification system (LPIS) crop type classification. Our approach allows for the automatic integration of temporal knowledge, i.e., crop rotations using existing parcel-based land cover databases and multi-modal Sentinel-1 and -2 time series. The temporal evolution of crop types was modeled with a linear-chain conditional random field, trained with time series of multi-modal (radar and optical) satellite acquisitions and associated LPIS. Our model was tested on two study areas in France ($\geq 1250 \text{ km}^2$) which show different crop types, various parcel sizes, and agricultural practices: the Seine et Marne and the Alpes de Haute-Provence classified accordingly to a fine national 25-class nomenclature. We first trained a Random Forest classifier without temporal structure to achieve 89.0% overall accuracy in Seine et Marne (10 classes) and 73% in Alpes de Haute-Provence (14 classes). We then demonstrated experimentally that taking into account the temporal structure of crop rotation with our model resulted in an increase of 3% to +5% in accuracy. This increase was especially important (+12%) for classes which were poorly classified without using the temporal structure. A stark positive impact was also demonstrated on permanent crops, while it was fairly limited or even detrimental for annual crops.

Introduction

The Sentinel-1 and -2 satellites provide open and free acquisitions exhibiting unprecedented characteristics which are well-suited to agriculture monitoring: high temporal frequency (5–6 days), the complementary C-band Sentinel-1 radar images and multispectral Sentinel-2 images with relevant spectral bands to crop mapping, and high spatial resolution (10–20 m). In Europe, several cases of agricultural monitoring using Sentinel images have been proposed (European Commission 2016), such as observing crops (e.g., for crop area estimates, crop map products, crop phenology indicators) and controlling Common Agricultural Policy payments (e.g., for permanent grasslands, greening measures). Sentinel Images have also been used for updating and controlling the quality of the land parcel identification system (LPIS), a geographical information system on agricultural parcels, at a national scale, updated annually (Boryan, Yang, Mueller *et al.* 2011).

This paper introduces a tool for automated LPIS crop type classification from multi-modal Sentinel time series which incorporates knowledge from existing LPIS editions to improve its accuracy.

Multi-Temporal Satellite Images for Crop Mapping

Satellite time series are particularly well-suited for identifying different crop types, as they allow for the monitoring of the

evolution of the plant's phenology. This is particularly crucial in the growing or harvest seasons. Synthetic aperture radar (SAR) data are crucial as well, as they mitigate the effect of cloud cover.

Many studies have demonstrated the potential of multi-temporal Sentinel and Landsat-8 images for crop type mapping (Palchowdhuri, Valcarce-Diñeiro, King *et al.* 2018; Veloso, Mermoz, Bouvet *et al.* 2017; Vuolo, Neuwirth, Immitzer *et al.* 2018; Belgiu and Csillik 2018; Ottosen, Lommen, Skjåvåg, 2019; Defourny, Bontemps, Bellemans *et al.* 2019) and the contribution of SAR time series for crop monitoring (Whelen and Siqueira, 2017; Li, Zhang, Zhang *et al.* 2019).

Inglada, Arias, and Tardy *et al.* (2015) assessed state-of-the-art methods for automatic crop mapping with multi-temporal and high resolution optical images. Five different classification approaches using SPOT4 and Landsat-8 images were compared for six annual crops, over 12 different study areas, with the best results (overall accuracy) (OA = 80%) obtained using the Random Forest classifier. In Kussul, Lemoine, and Gallego *et al.* (2016), Landsat-8 and Sentinel-1 time series were used on a study area in Ukraine. A pixel-based classification combined with a parcel-based regularization (majority voting) was proposed using LPIS ancillary data. An OA of 89% was reached, but only on a nomenclature comprised of six annual crops and large parcels (>250 hectares (ha)). Wagner, Narasimhan, and Waske (2018) combined Sentinel-1 and -2 to improve land cover mapping in cloud-prone regions. Veloso, Mermoz, and Bouvet *et al.* (2017) showed the importance of radar data for crop mapping. More recently, the Sentinel-2 Agriculture Consortium (Sen2Agri) has led experiments at the country level (Czech Republic) using Sentinel time series for crop mapping (Sen2-Agri GISAT s.r.o. 2018). A multi-sensor (Sentinel-1, Sentinel-2) pixel-based supervised classification was performed. The LPIS was used for both learning and validation steps. Monthly cropland maps were produced with an overall accuracy greater than 80%, and each land cover type had a F-score greater than 60%. In Defourny, Bontemps, Bellemans *et al.* (2019), three entire countries (Ukraine, Mali, and South Africa) and five local cities were mapped using Sen2Agri system. Overall accuracy values were higher than 90%, and already as high as 80% midseason. However, only the five major crops were considered for each site. For the Sen2Agri framework, the nomenclature was generally limited to 5–7 classes and did not fully integrate temporal knowledge from existing data.

Crop Rotation Integration

Crop rotation knowledge can be used to improve agricultural yields (Berzsenyi, Györfy, and Lap *et al.* 2000) and soil quality (Karlen, Hurlley, Andrews *et al.* 2006). Crop type prediction can also be improved using *prior* knowledge on crop rotations per parcel since a crop type is strongly correlated to past crop types. Modeling such temporal structures from

Sébastien Giordano, Loïc Landrieu, and Nesrine Chehata are with the University Paris-Est, LASTIG MATIS, IGN, ENSG, F-94160 Saint-Mandé, France.

Simon Bailly is with Wanaka, Paris, France.

Nesrine Chehata is with EA 4592, G & E Lab, Bordeaux INP/Bordeaux Montaigne University, France.

Photogrammetric Engineering & Remote Sensing
Vol. 86, No. 7, July 2020, pp. 431–441.
0099-1112/20/431–441

© 2020 American Society for Photogrammetry
and Remote Sensing
doi: 10.14358/PERS.86.7.431

Sentinel image time series can lead to significant gains in classification accuracy. To take into account crop rotations in crop mapping, two issues have to be addressed:

1. How to model the crop rotations?
2. How to integrate crop rotations in a land cover classification process?

Two different approaches can be used to model rotations. The first one uses *a priori* agronomist expert knowledge. The second one consists in automatically learning crop rotations from the statistical analysis of past practices, as found in the LPIS annual archives. This crop rotation knowledge can then be modeled in a probabilistic framework by estimating the transition probabilities between each crop type from past years to the next. Castellazzi, Wood, Burgess *et al.* (2008) introduced a mathematical framework modeling such transition probabilities to predict crop rotations at the landscape scale. Few studies have yet focused on the integration of crop rotation information into classification pipelines. Osman, Inglada, and Dejoux (2015) studied early crop mapping using Markov logic, but not in combination to remote sensing observations. This model proved efficient for early crop type predictions at the beginning of the growing season, when few satellite images are available and crops are hard to distinguish. Other studies proposed to introduce a temporal structure using Hidden Markov Chains in a classification pipeline but aimed at modeling phenology instead of crop rotations (Aurdal, Huseby, Eikvil *et al.* 2005; Leite, Feitosa, Formaggio *et al.* 2011; Siachalou, Mallinis, Tsakiri-Strati 2015). Kenduiywoa, Bargiel, and Soergel (2015) modeled phenology information into a conditional random field (CRF), but the classification was performed at different dates through the year. The CRFs were used for classifying land cover classes and crop types on mono-temporal Landsat data (Roscher, Waske, Förstner 2017). Hoberg, Rottensteiner, Feitosa *et al.* (2015) used CRF on multi-temporal and multi-scale classification for change detection.

Objectives

This paper focuses on crop type prediction using LPIS and crop rotation knowledge learned from Sentinel-1 and -2 time series. This raises three main application and methodological questions: (1) What are the respective contributions of optical and radar time series for crop type prediction? (2) How to combine crop rotation and satellite observations into a unified classification pipeline? (3) What is the contribution of the temporal structure with regard to observation-based classification?

To answer these questions, we propose a series of experiments on the areas of interest using a detailed nomenclature with 25 classes with no assumption on parcel sizes. We test the contribution of both optical and radar time series separately and jointly. We then compare the accuracy of classifying these time series each year independently and integrating the temporal structure into a probabilistic model (linear chain CRFs) representing the influence of crop rotations.

This paper is organized as follows: we present the study sites and data in the section “Sites and Material”. In the section “Methodology”, an observation-based classification at the parcel scale is presented, as well as a temporal-structured framework to integrate crop rotation information. Results are given and discussed in the sections “Results” and “Discussion”, respectively.

Sites and Material

Study Sites

Two complementary sites were chosen in French territories. Both sites are research observatories where in-field crop type annotations are made annually. The location and characteristics of each site are provided in Figure 1 and Table 1,

respectively. The site name refers to the national number of the corresponding administrative department. Site04 is located in South Eastern France, in the Alpes de Haute-Provence region, in the Durance River Valley. It is a representative of Mediterranean cultivated areas. It covers 1050 km² and is characterized by a highly variable topography, a very fragmented landscape, and a high diversity of crop types. Site77 is located near Paris, in the Seine et Marne region. It covers 233 km². Contrary to Site04, it is characterized by a flat relief, with large parcels and a majority of cereal crops. Figure 2 shows the distribution of parcel sizes on both sites. One can see that Site04 is much more fragmented with very small parcels, while Site77 has larger parcels reaching 20 ha.

Land Parcel Identification System

In France, the land parcel identification system (LPIS) is called *registre parcellaire graphique* (RPG). It has been available for the whole territory since 2002. For cultivated areas, the RPG gathers the geometric information (i.e., the parcel

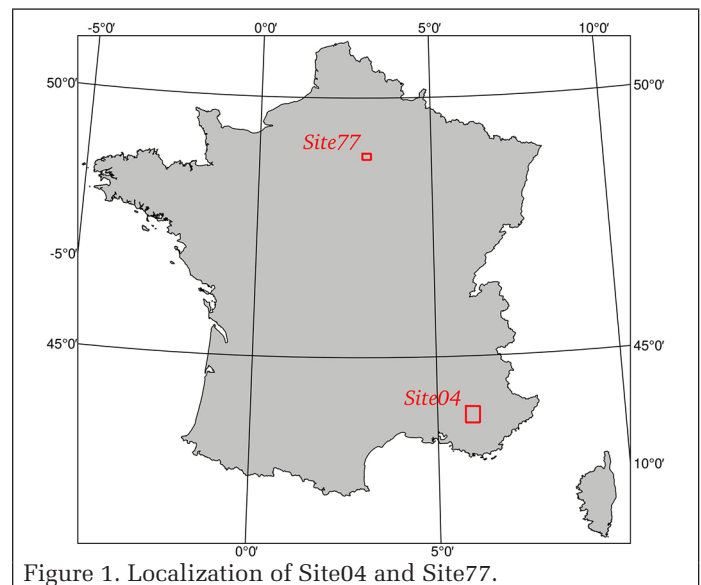


Figure 1. Localization of Site04 and Site77.

Table 1. Comparison of both study sites in terms of areas and crop types.

Class	No. parcels– Site04	No. parcels– Site77
Corn	147	350
Barley	517	158
Other cereals	2176	889
Rapeseed	154	85
Sunflower	293	X
Other oilseeds	116	X
Protein (peas)	87	76
Fiber plants	X	76
Forage crops	1215	46
Meadows	3652	725
Fruit trees	298	30
Vineyards	249	X
Olive groves	1029	X
Aromatic crops	1452	X
Vegetables	520	131
Total no. classes	14	10
Total no. stable parcels (2015–2016)	9230	1902
Site area (km ²)	1050	233

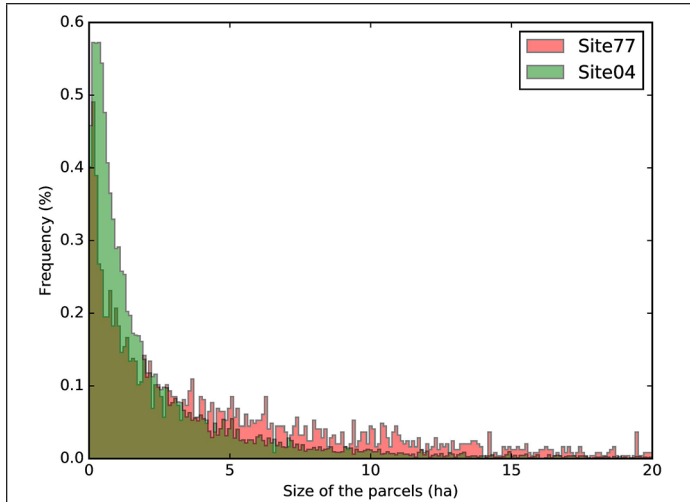


Figure 2. Normalized histogram of parcel areas for Site04 and Site77.

delimitation) and the corresponding semantic information such as the owner, the operator, the area, and the crop type.

Both geometric and semantic information are updated by the farmers annually. Until 2014, the declarations were made at a block scale that corresponds to contiguous parcels with the same operator. Since 2015, the declarations have been made at the parcel scale, which simplifies machine-learning based approaches to crop prediction. The crop type is specified among more than 300 subclasses which are organized into 25 classes. 14 and 10 of these classes are present on Site04 and Site77, respectively (cf. Table 1).

Figures 3 and 4 show the 2016 RPG edition, i.e., the ground truth data on Site04 and Site77 respectively, with the corresponding crop types. For Site04, dominant crops are: cereals (23.8%), meadows (30.7%), aromatic crops (12.2%), forage crops (10.2%), and olive groves (8.6%). As for Site77, two dominant crops are present: cereals (57.7%) and meadows (28.3%), followed by vegetables (5.1%). In this latter case, the data is highly imbalanced, making Site77 classification task more complex.

In this study, to be in tune with the first Sentinel-2 images availability, only the 2016 edition of parcel-based RPG was used for the training and the validation of the supervised classification model (see the section “Parcel-Wise Multi-Source Classification”). The 2015 parcels were necessary to train the temporal structured method (see the section “Temporal-Structured Classification”). For learning crop rotations, only the geometrically stable blocks of parcels from 2010 to 2014 were used. The number of geometrically stable parcels for both sites is given in Table 1.

Multimodal Sentinel-1 and -2 Images

We use both optical and radar Sentinel time-series for crop mapping. Sentinel-2 (S2) provides 10 multispectral bands for earth observation on the visible-short-wave infrared (VIS-SWIR) domain at 10 m and 20 m spatial resolution. Near infrared (NIR) and red-edge bands allow a fine characterization of crops. Sentinel-1 (S1) is a C-band SAR. The available mode on the studied sites was the Interferometric Wide (IW) mode that presents a dual polarization VV and VH.

For the year 2016, Sentinel-2 images were automatically downloaded from the Theia platform (<https://www.theia-land.fr/>) in tiled format, calibrated as Top of Canopy (TOC) reflectance (Hagolle, Huc, Villa Pascual, *et al.* 2010) and accompanied with robust cloud mask information (Hagolle, Huc, Villa Pascual, *et al.* 2015). The 20 m Sentinel-2 images were resampled to 10 m spatial resolution. Radar Sentinel-1 images were downloaded from the Peps platform ([| LPIS - RPG \(2016\) : 11 905 parcels | | | DTM \(m\) | |
|------------------------------------|----------------------|------------------------|---------|-----|
| Corn \(1.2%\) | Other oilseeds \(1%\) | Vignards \(2.1%\) | 276 | 418 |
| Barley \(3.9%\) | Protein\(peas\) \(0.7%\) | Olive groves \(8.6%\) | 561 | 703 |
| Other cereals \(18.7%\) | Forage crops \(11.1%\) | Aromatic crops \(12.3%\) | 846 | |
| Rape seed \(1.3%\) | Meadows \(29.8%\) | Vegetables \(4.3%\) | | |
| Sun flower \(2.5%\) | Fruit trees \(2.5%\) | | | |](https://</p>
</div>
<div data-bbox=)

Figure 3. Site04: 2016 RPG parcel superimposed to a very high resolution Digital Terrain Model.

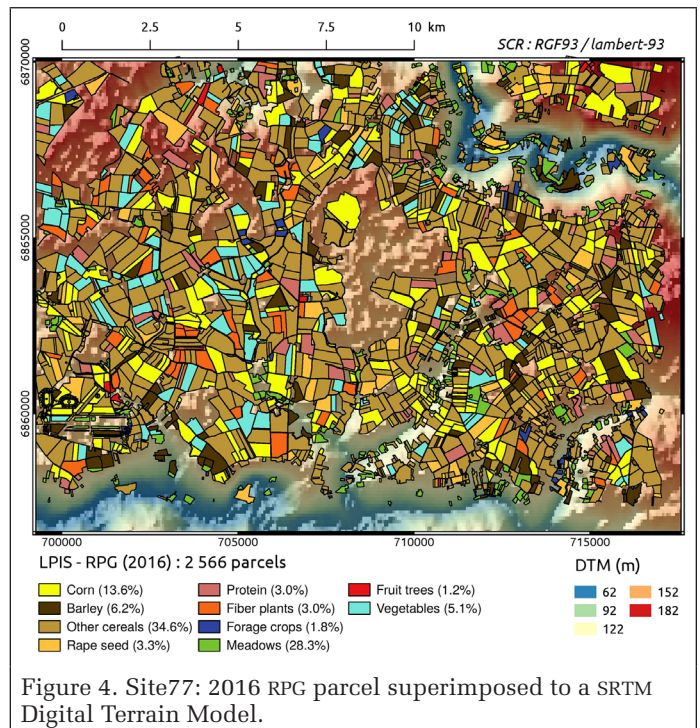


Figure 4. Site77: 2016 RPG parcel superimposed to a SRTM Digital Terrain Model.

peps.cnes.fr) in the Ground Range Detected format (GRD) which corresponds to the average of approximately five Single Look Complex acquisitions corrected by the incidence angle and resampled at 10 m spatial resolution.

The total number of images is given in Table 2 and confirms the complementarity between Sentinel-1 and Sentinel-2 images. On Site77, particularly high cloud coverage led to only 12 Sentinel-2 images. In addition, S2 orbit over Site77 had many acquisition problems in 2016. On the contrary, on this site, ascendant S1 images overlap, leading to more available radar images.

Sentinel Images Preprocessing

Figure 5 illustrates the optical and radar preprocessing steps to obtain parcel-based features for the classification workflow.

The dual polarization GRD S1 images were first calibrated to σ_0 radar backscattering coefficient. The orthorectification was performed using the Shuttle Radar Topography Mission (SRTM) digital terrain model. The speckle is partly removed using a simple 5×5 Lee filter (Lee 1980). In addition to VV and VH radar features, an extra radar feature ($\sigma_{0_{VH}}/\sigma_{0_{VV}}$) was derived. This ratio is known to be more robust to acquisition system errors or environmental factors such as soil moisture leading to a more stable temporal indicator (Veloso, Mermoz, Bouvet *et al.* 2017). Average and standard deviation of these three features were then computed for each date and for each parcel. The number of radar features is shown in Table 2.

Sentinel-2 images were already orthorectified and calibrated in TOC reflectance. On Site77, only 12 Sentinel-2 optical images were obtained in 2016, as shown in Figure 6 with corresponding cloud cover, whereas 23 images were available on Site04 (cf. Figure 7). The missing data (clouds) were filled using a multi-temporal spline interpolation (Inglada 2016). Average and standard deviation of the 10 spectral bands and the Normalized Difference Vegetation Index (NDVI) per optical image were then computed for each date and for each parcel. The number of optical features is shown in Table 2.

Methodology

Our method proceeds in two steps: parcel-wise classification and temporal modeling. The first step aims to predict the crop types per parcel using Sentinel time-series for each year independently. The second step integrates the temporal structure into a probabilistic structured model representing the influence of crop rotations. Modeling this temporal dependency may help correct erroneous classifications made in the first step and may also help classify ambiguous parcels by considering crops from previous years.

Parcel-Wise Multi-Source Classification

We first compute discriminative parcel-based features from satellite time-series. For each parcel, we consider all available optical and radar images for one year. We consider the average and standard deviation of each spectral feature over the pixels composing the parcel extent. We then concatenate the

Table 2. Characteristics of the parcel-based features for both sites.

Site	No. of dates	Optical features	Radar features	Total
04	Optical: 23	22 per image	6 per image	Optical: 460
	Radar: 28	σ, μ of (10 bands + NDVI)	(σ, μ of 3 radar features)	Radar: 168
Total				628
77	Optical: 12	22 per image	6 per image	Optical: 240
	Radar: 85	σ, μ of (10 bands + NDVI)	(σ, μ of 3 radar features)	Radar: 509
Total				749

Features are detailed in the text.

observations over the span of a year of acquisitions. A Random Forest classifier provides a parcel-wise prediction under the form of pseudoprobabilities.

For a given parcel i and a given year t , we denote $X_i^{(t)} \in \mathbb{R}^D$ the tensor of combined selected features, with D the selected feature size. Since we compute both mean and standard deviation for each channel at each time step, $D = 2 \times C \times S$, with C the number of channels, and S the number of acquisitions per year. To counterbalance the over-representation of certain classes in our data sets, we set class weights inversely proportional to the square root of the number of instances in each class. This class weights are used by the random forest classifier to give more importance to rare classes and recover them more easily.

Temporal-Structured Classification

We now consider the year-by-year temporal structure of each parcel independently. We denote by $X_i^{(t)} \in \mathbb{R}^{T \times D}$ the sequence

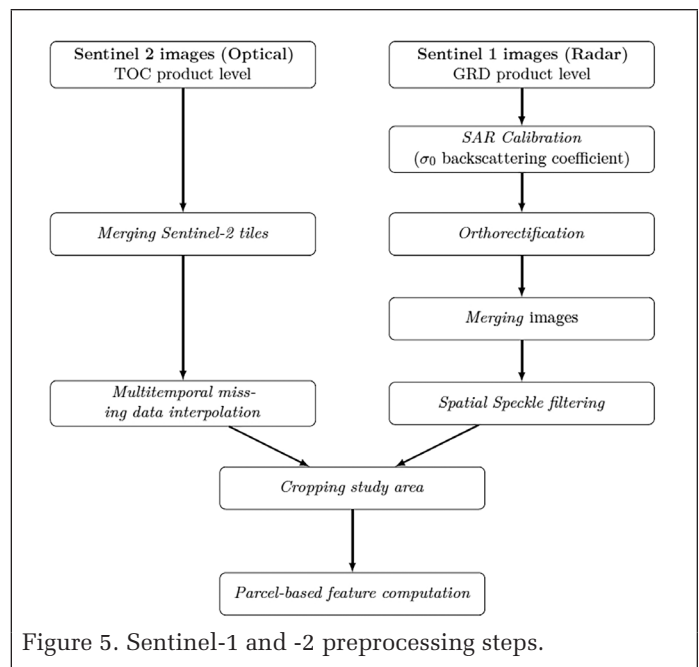


Figure 5. Sentinel-1 and -2 preprocessing steps.

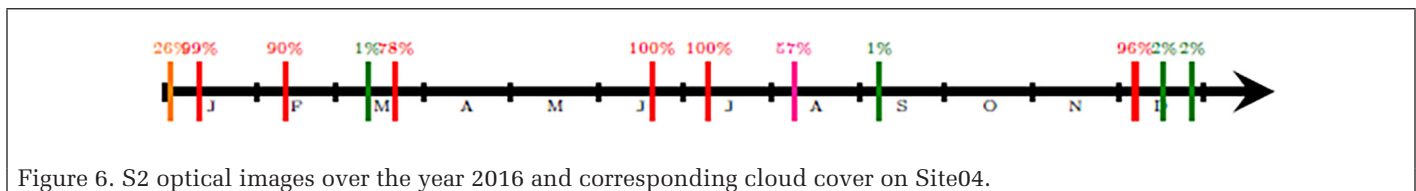


Figure 6. S2 optical images over the year 2016 and corresponding cloud cover on Site04.

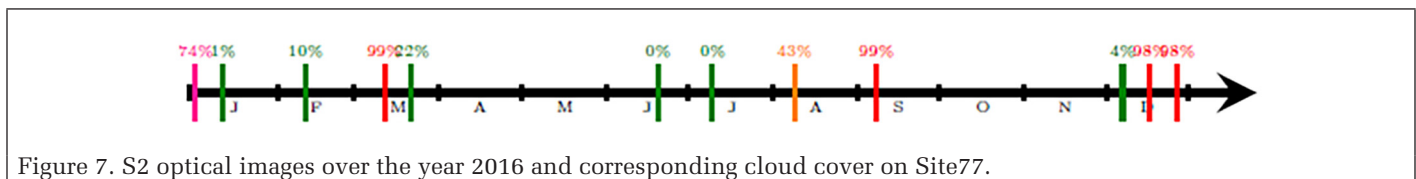


Figure 7. S2 optical images over the year 2016 and corresponding cloud cover on Site77.

of observed features $X_i^{(t)} \in \mathbb{R}^D$ for parcel i and for all years $t = 1, \dots, T$ available for training. Likewise, we denote $Y_i \in \mathcal{K}^T$ the ground truth labels for parcel i for each observed year $t = 1, \dots, T$ and with \mathcal{K} the set of all possible labels.

In the section “Temporal Structure”, we present the graphical model chosen to capture crop rotation. In the section “Learning”, we explain how the parameters of this model can be learned from previous LPIS editions. In the section “Inference”, we explain how to use our model to compute prediction of the label of a parcel at a given date.

Temporal Structure

The aim of this step is to model the yearly crop rotations in order to improve crop type prediction. We model this dependency with a linear chain CRF of order m , as shown in Figure 8. For a parcel i , we model the posterior distribution $P(Z_i | X_i)$ of predicted labels $Z_i \in \mathcal{K}^T$ given the observed features X_i as:

$$P(Z_i | X_i) = \frac{1}{A} \exp\left(\sum_{t=1}^T O(Z_i^{(t)}, X_i) + \sum_{t=m+1}^T I(Z_i^{(t-m)}, \dots, Z_i^{(t)}, X_i)\right), \quad (1)$$

where A is a normalizing factor, O the observation potentials, and I the interaction potentials, described below.

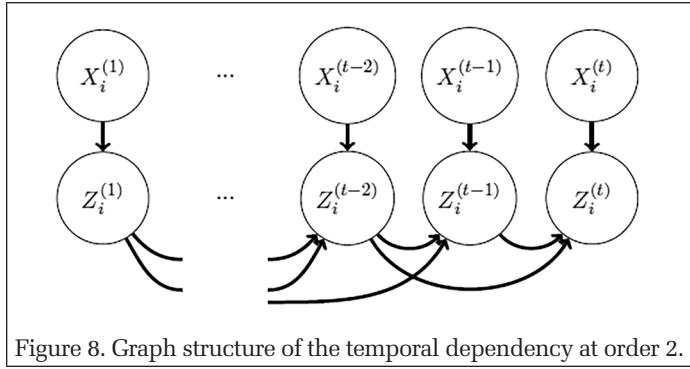


Figure 8. Graph structure of the temporal dependency at order 2.

Observation potential: The observation potential models the link between the observed features and the label of each parcel. $O(Z_i^{(t)}, X_i)$ is taken as the logarithm of $P_{RF}(Z_i^{(t)}, X_i)$, the pseudoprobability for parcel i at year t to be class $Z_i(t)$ given by the Random Forest classifier, described in the section “Parcel-Wise Multi-Source Classification”:

$$O(Z_i^{(t)}, X_i) = \log P_{RF}(Z_i^{(t)}, X_i). \quad (2)$$

Interaction potential: This potential models the temporal dependencies between the parcel’s labels at a given year t given the labels at the m previous years. We model this potential as the logarithm of the transition probability $M(Z_i(t-m), \dots, Z_i^{(t)})$ from the sequence of m previous labels $Z_i^{(t-m)}, \dots, Z_i^{(t-m)}$, to a label $Z_i^{(t)}$ at the current date (Liu, Song, Townshend *et al.* 2008). For the sake of simplicity, we choose a temporally homogeneous parametrization, independent of the observed features, and shared by all parcels and years:

$$I(Z_i^{(t-m)}, \dots, Z_i^{(t)}, X) = \log(M(Z_i^{(t-m)}, \dots, Z_i^{(t)})) \quad (3)$$

with $M \in \mathbb{R}^{\mathcal{K}^{m+1}}$ a tensor such that

$$\sum_{z_1, \dots, z_{m-1} \in \mathcal{K}^{m-1}} M_{z_1, \dots, z_{m-1}, z_m} = 1$$

for all $z_m \in \mathcal{K}$, i.e., a stochastic tensor of order m . The tensor M is referred to as the transition tensor.

Learning

The observation potential is obtained by training the random forest classifier. A transition tensor \hat{M} can be learned from labeled data over past years. Indeed, maximizing the log-likelihood in Equation 1 with respect to

$$z_1, \dots, z_m \in \mathcal{K}$$

to M yields the following tensor M , defined for all

$$\hat{M}_{z_1, \dots, z_m} = \frac{N_{z_1, \dots, z_m}}{N_{z_1, \dots, z_{m-1}}} \quad (4)$$

with N_{k_1, \dots, k_m} the number of sequences k_1, \dots, k_m observed in the labeled data for all parcels and all years, and $N_{k_1, \dots, k_{m-1}}$ the number of sequences k_1, \dots, k_{m-1} observed in the first $T-1$ years, where T is the total number of years available for training. Excluding the last year is necessary to ensure that \hat{M} is indeed a stochastic tensor.

To account for the large size of this matrix ($|\mathcal{K}|^{m+1}$), and to prevent numeric issues, we perform a Laplacian smoothing with $\alpha = 1$ as described in Manning, Raghavan, and Schütze (2008, chapter 11.3.2)).

Inference

The aim of this step is to predict the label $Z_i^{(t)}$ of a given parcel at year t from the observation of the current year, and knowing its labeling in the m previous years. Once the random forest yielding the observation potential is trained on all available data, and the transition tensor \hat{M} estimated, the prediction is given by:

$$P(Z_i^{(t)} = k | Z_i^{(t-m, \dots, t-1)}, X_i) \propto P_{RF}(Z_i^{(t)}, X_i) \times \widehat{M}[Z_i^{(t-m)}, \dots, Z_i^{(t-1)}] \quad (5)$$

and normalizing the results over $k \in \mathcal{K}$ to obtain a probability.

Experimental Setup

The random forest classifier is composed of 100 decision trees. The meta-parameters of the forest, such as the maximum number of attributes considered at each node, are chosen by k -fold cross-validation with $k = 4$.

For the temporal structure, spatiotemporal homogeneity hypothesis allows us to estimate the transition tensor \hat{M} . For each study site, we use the geometrically stable parcel blocks over a period of five years (2010–2014). To decrease the number of parameters, only first order transitions were used (transition from one year to the next).

The data is randomly split equally into two distinct training and testing sets. The model is trained and validated on the training set while the quality of the model is estimated on the testing set. The OA is used to assess the general performance of the model. The F-score combines user accuracy (UA, or precision) and producer accuracy (PA, or recall) and allows estimating the per-class quality. The F-score for a class C is defined as follows:

$$\text{F-score}(C) = 2 * \frac{UA_c \cdot PA_c}{UA_c + PA_c} \quad (6)$$

To sum up this information, the F-scores are averaged, with and without weighting by each class cardinality. The weighted F-scores reduce biases due to imbalanced data. The results are averaged over 10 runs.

Results

The results are presented on two distinct agricultural sites ($\geq 1250 \text{ km}^2$), showing different crop types with highly

imbalanced data, various parcel sizes, different agricultural practices, and acquired by different Sentinel image distributions. Prediction accuracies are presented using different feature combinations and both with and without temporal modeling. The impact of parcel size on the classification accuracy is also studied.

Transition Matrix Assessment

Figure 9 shows the estimated transitions between crop types as Hinton diagrams for both sites. First order transitions are normalized by the number of parcels of the initial class (year $n - 1$) which ensures it to be nonsensitive to imbalanced data. Besides, in case of missing crops, a smoothing is processed to avoid zeros in the transition matrix (cf. the section “Learning”). This smoothing may lead to some biases on minor classes but do not impact the results.

On Site04, the most probable transitions are to and from permanent crops, such as olive groves, vineyards, orchards, permanent meadows, and fruit trees reaching 98.34%, 93.87%, 92.72%, 91.89%, and 84.23%, respectively. From Figure 9, we can observe that the standard rotation patterns of annual crops are generally not applied in this area. For instance, the rapeseed, proteins, and sunflowers have probabilities of 76.53%, 66.78%, and 64.25%, respectively to be transformed to *other cereals* the following year.

On Site77, more transitions are observed for the annual crops. Agricultural rules for annual crop rotations seem to be better followed in this area. The rapeseed and proteins have probabilities of 97.09% and 94.85%, respectively, to be transformed to other cereals the following year. Indeed, rapeseed \rightarrow winter wheat (in other cereals) \rightarrow barley is a well-known three-year rotation for farmers of this area. Permanent crops such as meadows and fruit trees have a probability of being carried over the next year of 94.45% and 81.39%, respectively.

Optical versus Radar Sentinel Time Series

Overall accuracy and F-scores, using different configurations of optical and radar data, are displayed in Tables 3 and 4 for Site04 and Site77, respectively.

As reported in Site04 (cf. Table 3), optical data lead to better results than radar data (+9% for OA and +10% for weighted F-score). This may be explained by a low cloud cover in this area (Figure 7) and a finer native resolution of optical imagery that is more suited to small parcel sizes. Table 3 confirms that optical and radar combination led to the best results when not modeling the temporal structure.

Contrary to the previous site, on Site77 (cf. Table 4), radar attributes improved the results of optical ones by 7%, achieving an overall accuracy of 89%. This can be explained by a combination of frequent acquisition problems and a high cloud cover in 2016, leading to many missing optical Sentinel-2 data (cf. Figure 6). In addition, the parcels on Site77 are larger and thus more compatible with radar Sentinel-1 image spatial resolution. Consequently, using radar imagery solely led to similar results when combining optical and radar attributes.

Weighted F-scores, using combined radar and optical images, reached 88% and 71% on Site77 and Site04, respectively. The crop type mappings and prediction errors are illustrated on Figures 10, 11, 12, and 13 for Site04 and Site77, respectively for test parcels.

Impact of Temporal Structure

Table 5 and Table 6 display the F-score, the user, and producer accuracy measures per class for both approaches with and without temporal modeling using combined radar and optical images on Site04 and Site77, respectively. On Site77, from Table 6, one can see that high F-scores are obtained for annual

Table 3. Site04—Global prediction accuracies, using optical and radar imagery.

Config	OA	F-score	Weighted F-score
No temporal modeling			
Radar	0.64	0.59	0.61
Optical	0.73	0.67	0.71
Radar + Optical	0.73	0.68	0.71
Temporal modeling			
Radar	0.76	0.60	0.7
Optical	0.78	0.63	0.72
Radar + Optical	0.78	0.64	0.72

Table 4. Site77—Global prediction accuracy, using optical and radar imagery.

Config	OA	F-score	Weighted F-score
No temporal modeling			
Radar	0.89	0.73	0.88
Optical	0.82	0.62	0.81
Radar + Optical	0.89	0.74	0.88
Temporal modeling			
Radar	0.92	0.78	0.91
Optical	0.87	0.67	0.85
Radar + Optical	0.92	0.76	0.91

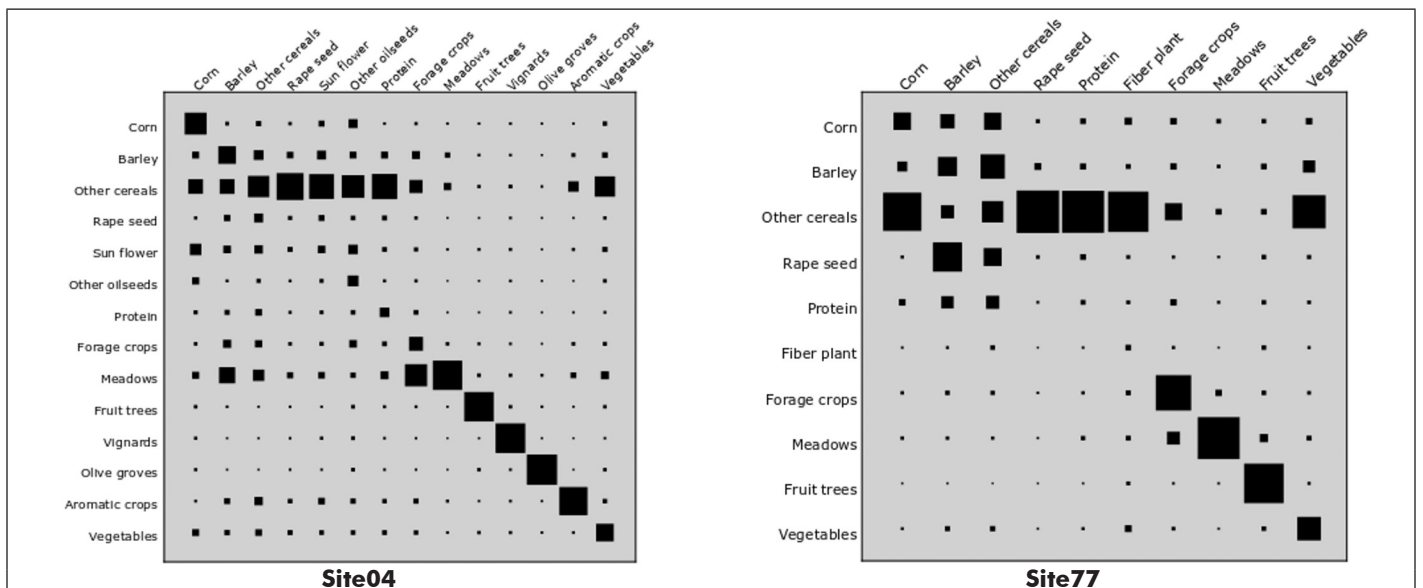


Figure 9. Representation of the transition matrices with a Hinton diagram.

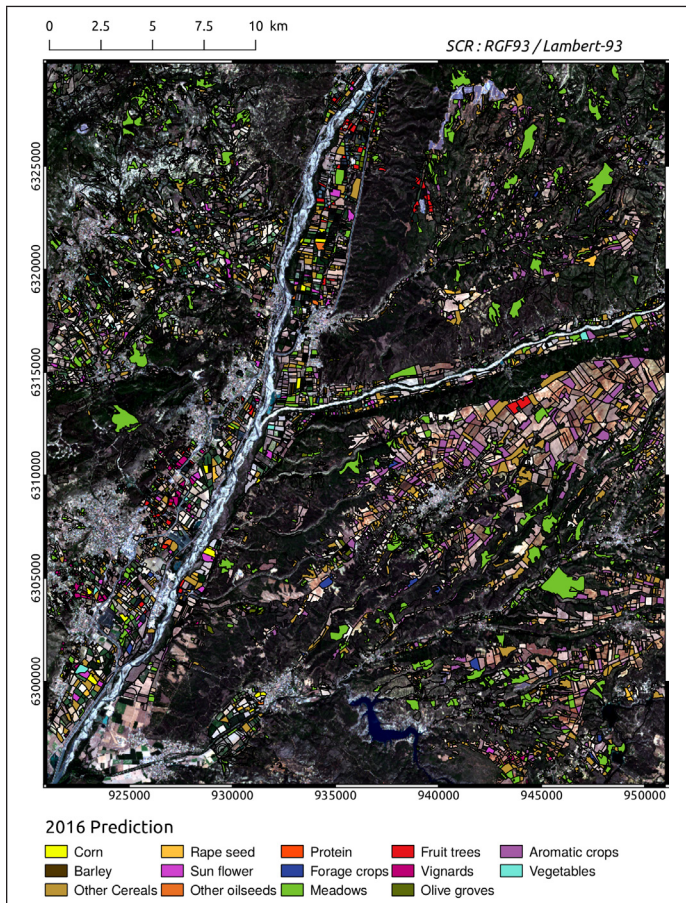


Figure 10. Site04: Crop type predictions.

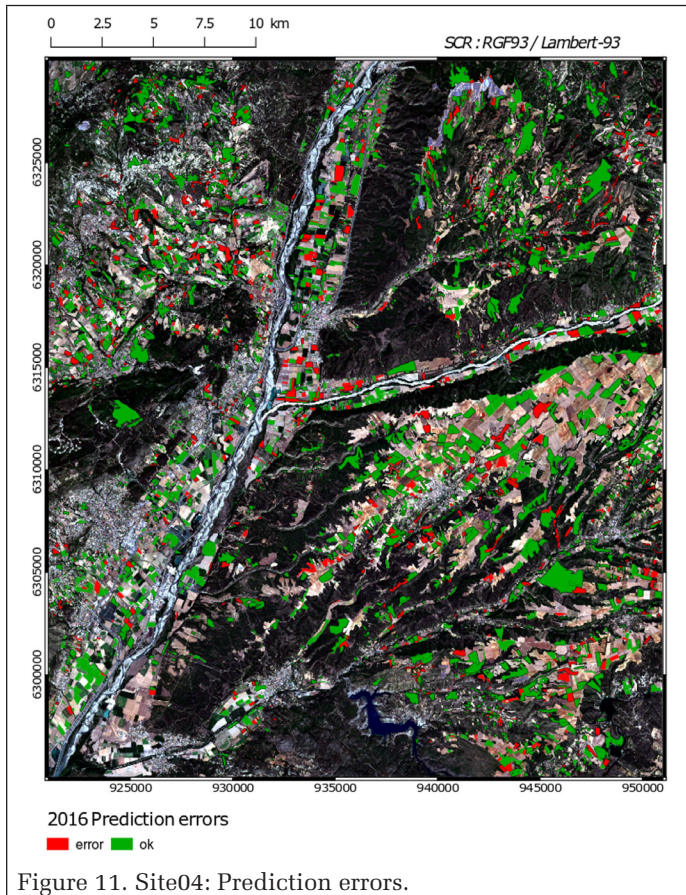


Figure 11. Site04: Prediction errors.

crops (corn (94%), barley (90%), other cereals (95%), rape-seed (96%), ...). However, forage crops and fruit trees were not identified by the classifier and were instead classified as meadows (cf. Table 8). Forage crops class is harder to classify using only satellite observations since it is more a land use class than a land cover class, based on agricultural knowledge about the destination of cereal crops. Table 8 shows that the meadows class is often confused with other classes, particularly fruit trees and other cereals. Meadows are composed of trees and bare soils and have a low volumetric radar response that make them indistinguishable from other cereals.

The quality of the prediction is lower for Site04, with a weighted F-scores varying between 61% and 71%. This is due to the presence of more classes (14), small size of parcels, and highly imbalanced classes where meadows and other cereals represented almost 50% of the area, as shown in Figure 3. Similar to Site77, the confusion matrix for combined optical and radar data (Table 7) shows that most ambiguities occurred on meadows classes, other cereals, and forage crops. Besides, aromatic crops represented 12.3% of the area and proved hard to classify correctly.

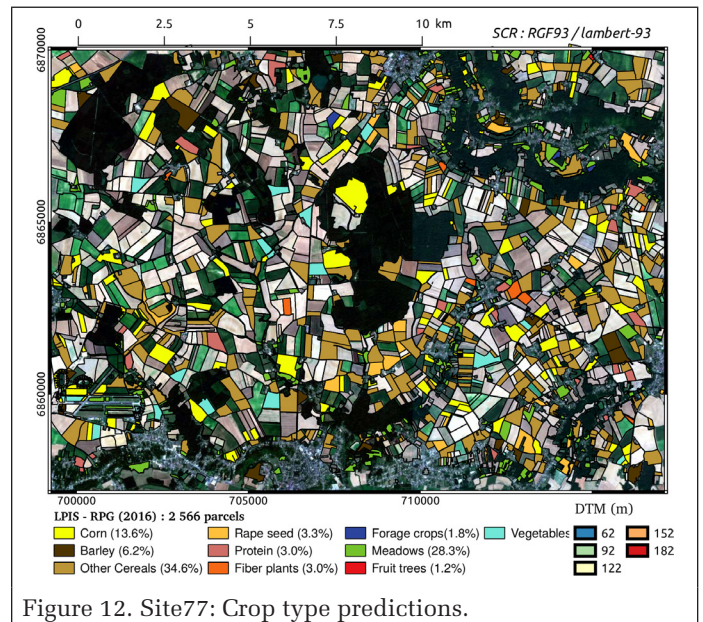


Figure 12. Site77: Crop type predictions.

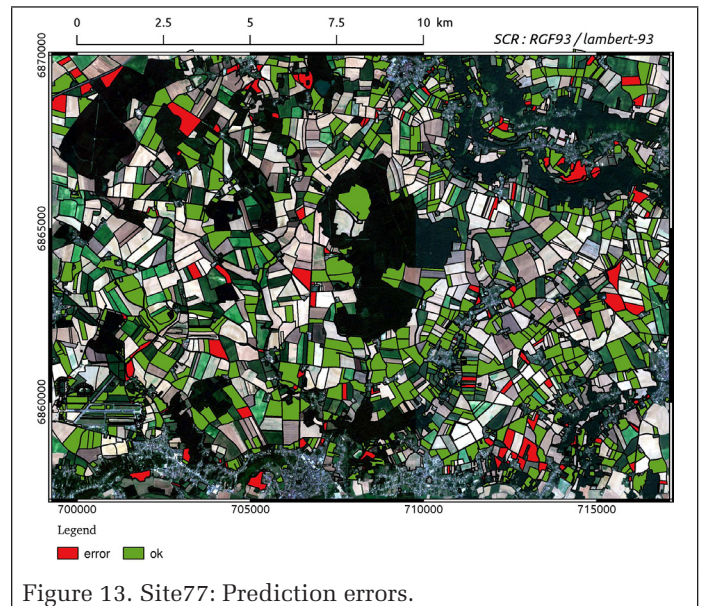


Figure 13. Site77: Prediction errors.

Table 5. Site04—Effect of temporal modeling on classification metrics, using combined radar and optical attributes.

Class	No temporal modeling			Temporal modeling		
	F-score	User. Acc	Proc. Acc	F-score	User. Acc	Proc. Acc
Corn	0.89	0.95	0.83	0.78	0.84	0.73
Barley	0.40	0.85	0.26	0.18	0.67	0.11
Other cereals	0.85	0.83	0.86	0.78	0.73	0.84
Rapeseed	0.92	1	0.86	0.71	1	0.55
Sunflower	0.79	0.78	0.79	0.71	0.75	0.68
Other oilseeds	0.57	0.74	0.46	0.41	1	0.26
Protein	0.49	1	0.32	0	0.07	0
Forage crops	0.47	0.73	0.34	0.1	0.88	0.05
Meadows	0.76	0.67	0.87	0.80	0.67	0.98
Fruit trees	0.61	0.86	0.47	0.97	0.96	0.97
Vineyards	0.69	0.74	0.65	0.99	0.99	0.98
Olive groves	0.74	0.82	0.67	0.99	0.99	0.99
Aromatic crops	0.74	0.65	0.86	0.93	0.94	0.92
Vegetables	0.61	0.72	0.53	0.67	0.9	0.54

Table 6. Site77—Effect of temporal modeling on accuracy metrics, using combined radar and optical attributes.

Class	No temporal modeling			Temporal modeling		
	F-score	User. Acc	Proc. Acc	F-score	User. Acc	Proc. Acc
Corn	0.94	0.93	0.95	0.88	0.83	0.93
Barley	0.90	0.94	0.86	0.82	0.78	0.85
Other cereals	0.95	0.96	0.94	0.95	0.94	0.97
Rapeseed	0.96	0.97	0.94	0.97	0.98	0.95
Protein	0.95	0.93	0.97	0.95	0.97	0.94
Fiber plants	0.97	1	0.95	0	0.1	0
Forage crops	0	0.1	0	0.70	0.78	0.65
Meadows	0.87	0.81	0.93	0.95	0.94	0.97
Fruit trees	0.01	0.1	0	0.94	1	0.89
Vegetables	0.89	0.91	0.88	0.45	0.97	0.30

Table 7. Site04—Confusion matrices using combined optical and radar attributes.

Classification	Ground truth													
	Corn	Barley	O. cereals	Rapeseed	Sunflower	O. oilseeds	Protein	Forage crops	Meadows	Fruit trees	Vineyards	Olive groves	Arom. crops	Vegetables
Optical and radar without temporal modeling														
Corn	31	-	-	-	1	2	-	-	-	-	1	-	-	3
Barley	-	47	9	-	-	-	-	3	37	-	-	-	13	-
O. cereals	-	5	684	-	5	1	-	5	59	-	-	4	25	1
Rapeseed	-	-	1	56	-	-	-	-	10	-	-	-	-	-
Sunflower	-	-	1	-	78	-	-	-	2	-	-	-	13	4
O. oilseeds	1	-	-	-	7	18	-	-	4	-	1	-	2	7
Protein	-	2	6	-	-	-	10	1	7	-	-	-	2	-
Forage crops	-	-	18	-	1	-	-	173	239	6	3	9	64	2
Meadows	-	3	16	-	3	1	-	47	1294	-	9	27	77	3
Fruit trees	1	-	1	-	-	-	-	-	52	56	1	9	5	-
Vineyards	-	-	-	-	-	-	-	-	18	-	74	4	19	-
Olive groves	-	-	4	-	-	1	-	1	113	1	6	311	26	1
Arom crops	-	-	1	-	-	-	-	-	64	-	2	6	480	2
Vegetables	-	-	2	-	6	4	-	2	18	-	4	6	9	60
Structured optical and radar														
Corn	28	-	7	-	1	-	-	-	1	-	-	-	1	-
Barley	-	20	123	-	-	-	-	-	47	-	-	-	-	-
O. cereals	1	1	676	-	2	-	-	-	102	-	-	-	6	1
Rapeseed	-	5	21	35	-	-	-	-	6	-	-	-	-	-
Sunflower	-	-	6	-	67	-	-	1	13	-	-	-	8	3
O. oilseeds	4	-	4	-	7	10	-	-	14	-	-	-	-	1
Protein	-	2	21	-	-	-	-	-	5	-	-	-	-	-
Forage crops	1	-	15	-	3	-	-	25	461	-	-	-	9	1
Meadows	-	1	16	-	1	-	-	2	1456	-	-	1	3	-
Fruit trees	-	-	-	-	-	-	-	-	2	122	1	-	-	-
Vineyards	-	-	-	-	-	-	-	-	3	-	112	-	-	-
Olive groves	-	-	1	-	-	-	-	-	3	2	-	458	-	-
Arom crops	-	1	17	-	-	-	-	-	26	-	-	-	511	-
Vegetables	-	-	20	-	10	-	-	-	16	3	-	-	4	58

Impact of Parcel Size

Figures 14 and 15 show the impact of parcel size on parcel-based classification without temporal modeling on both sites. For Site04, when keeping only large parcels (area >3 ha), overall accuracy improves by 15%, 5.9%, and 8.7% for radar, optical, and combined optical/radar attributes, respectively (Figure 14). Indeed, due to the limited spatial resolution of Sentinel-1 images, radar attributes are less robust on small parcel sizes. When considering parcels larger than >3 ha, radar images achieve similar results as optical images, with an overall accuracy of 79.3%. Finally, combining optical and radar data lead to better results in all cases, and especially for large parcels.

As for Site77, similarly to Site04, when considering only parcels larger than >3 ha, the overall accuracy is greatly improved by radar attributes (+ 8.1% reaching 97.1%), which confirms that radar images are less robust for smaller parcels.

Discussion

In the following, we will compare the contribution of optical and Radar Sentinel time series and the impact of parcel size. We then detail the impact of modeling the temporal structure and finally explain the impact of the site characteristics on the results.

Classification Without Temporal Modeling

First, we will compare the results of both sites using parcel-based crop type prediction based on image observations only (without temporal modeling).

Optical versus Radar Sentinel Time Series

Depending on the image distribution and the cloud cover, optical data may not lead to good results for crop type mapping. In our case, temporal missing data interpolation was used, which led to some uncertainties and decreased the classification accuracy. On the other hand, radar data are less robust for small parcels (≤ 1.5 ha). However, this issue can be reduced by refining the preprocessing framework of radar data.

These results confirm that combining optical and radar data ensures higher crop type prediction accuracy, and lead to more robust prediction, independently from the study site.

Impact of Parcel Size

Weighted F-scores on both sites are highly dependent on parcel sizes as detailed hereby. For both sites, when keeping only large parcels (area >3 ha), overall accuracies are improved by radar attributes (+15% and +8.1% for Site04 and Site77, respectively). Indeed, due to the limited spatial resolution of Sentinel-1 images, radar attributes are less robust on small parcel sizes.

In order to make radar data more robust to parcel of limited sizes, some improvements could be undertaken on radar data preprocessing. To this end, we used speckle filtering (Lee 1980) on a restricted local neighborhood (5 × 5). This is suitable for large parcels as the radar scattering coefficients are averaged afterwards at the parcel level. However, when the parcel area is too small with respect to the Sentinel-1 spatial resolution, this method is no longer suitable. Adaptive

radar speckle filtering to small objects should be investigated (Deledalle, Denis, Tupin *et al.* 2015).

For optical attributes, the relation between parcel size and accuracy is less pronounced. Many factors may impact the overall accuracy such as cloud cover, data imbalance, and the parcel size. Indeed, some classes are more represented in small parcels (0.5–1.5 ha) and are well identified, such as rapeseed, protein, meadows, and fiber plants. Removing these small parcels may decrease the overall accuracy.

Combining optical and radar data lead to better results in all cases, and especially for large parcels. Finally, this sensitivity study confirms the robustness of combined radar and optical data to the parcel size.

Impact of Temporal Structure

The modeling of temporal structure, i.e., crop rotation modeling, improved the global prediction accuracies on both sites. On Site04 (cf. Table 5), temporally-structured classification improved the overall accuracy and the weighted F-score by 5% and 1%, respectively. When considering only radar data,

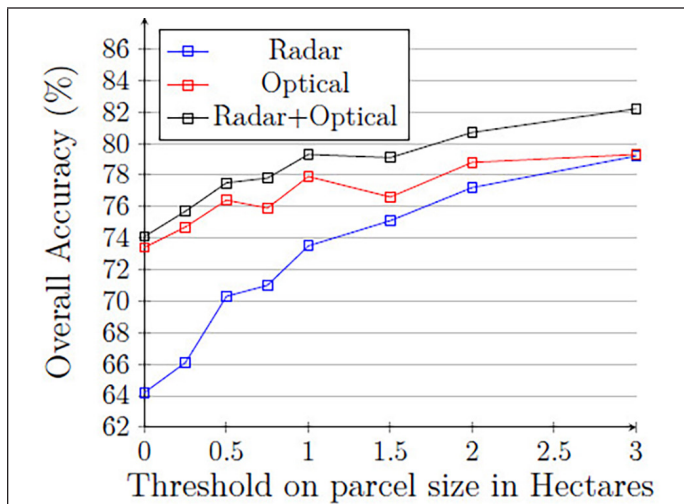


Figure 14. Site04: Impact of parcel size on the overall accuracy of the classification without temporal modeling. x-axis: only parcels whose surface area exceeds the threshold (in ha) are considered.

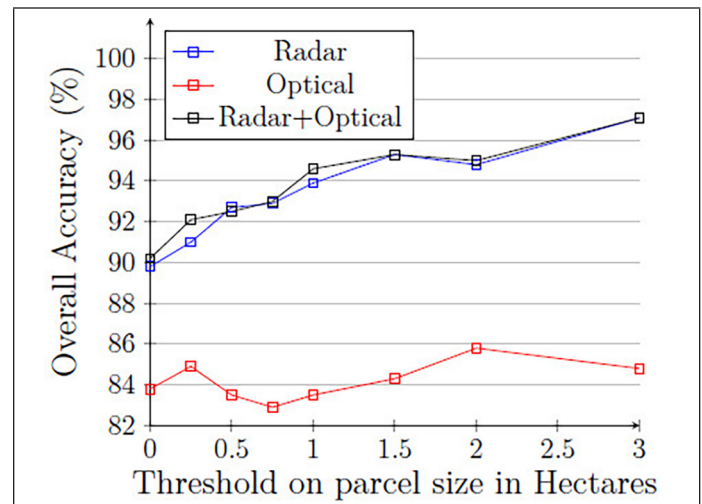


Figure 15. Site77: Impact of parcel size on the overall accuracy of the classification without temporal modeling; x-axis: only parcels whose surface area exceeds the threshold (in ha) are considered.

Table 8. Site77—Confusion matrices using combined optical and radar attributes.

	Ground truth									
	Corn	Barley	O. cereals	Rapeseed	Protein	Fiber plants	Forage crops	Meadows	Fruit trees	Vegetables
Classification										
Optical and radar without temporal modeling										
Corn	119	-	-	-	-	-	-	6	-	-
Barley	1	48	2	-	1	-	-	3	-	-
O. cereals	-	2	309	-	-	-	-	19	-	1
Rapeseed	-	-	-	38	-	-	-	3	-	-
Protein	-	-	-	-	27	-	-	1	-	-
Fiber plants	-	-	-	-	1	9	-	-	-	-
Forage crops	-	-	1	-	-	-	-	20	-	-
Meadows	10	1	9	1	-	-	-	276	-	1
Fruit trees	-	-	-	-	-	-	-	12	-	-
Vegetables	1	-	1	-	-	-	-	1	-	27
Structured optical and radar										
Corn	118	1	1	-	-	-	3	2	-	-
Barley	1	48	5	-	-	-	-	1	-	-
O. cereals	-	2	321	1	-	-	-	7	-	-
Rapeseed	-	-	1	39	-	-	-	1	-	-
Protein	-	-	1	-	27	-	-	-	-	-
Fiber plants	1	8	-	-	1	-	-	-	-	-
Forage crops	-	1	2	-	-	-	13	5	-	-
Meadows	4	-	4	-	-	-	1	289	-	-
Fruit trees	-	-	-	-	-	-	-	-	12	-
Vegetables	19	-	2	-	-	-	-	-	-	9

unstructured accuracies were very low, with an overall accuracy of 64% and a weighted F-score of 61%. The temporal modeling approach improved corresponding OA and weighted F-score by 12% and 9%, respectively, confirming the contribution of temporal structure even if the accuracy of the parcel-wise prediction was low. As for Site77, the structured approach slightly improved the weighted F-scores by 3%, 4%, and 3% for radar, optical, and combined optical/radar attributes, respectively. The contribution of temporal structure is lower than that in Site04, as the initial parcel-wise accuracies were already high (weighted F-scores >0.88).

As seen in Table 5, temporal structure modeling significantly improved per-class accuracies of permanent crops (fruit trees +36%, vineyards +30%, olive groves +25%, aromatic groves +19% for Site04), which reached F-scores higher than 93%. The meadows class F-score was improved by 4%. These results were expected since the permanent crops have the highest transition probability as shown in the section "Transition Matrix Assessment". However, F-scores of annual crops classes decreased when using temporal structure; only slightly so for corn (-11%), other cereals (-7%), and sunflowers (-8%), but rapeseed (-21%), barley (-22%), other oilseeds (-16%), protein (-49%), and forage crops (-46%) are significantly more often misclassified (cf. Table 7). This may be explained, in our opinion, by two facts: first, the crop rotations are modeled by a temporal regularization between the observation-based term (classification without temporal structure) and the crop transition probabilities. The prediction is a trade-off between both data and regularization terms. If the data-term is high (good prediction with observations), adding crop rotation information does not impact the results significantly (as for corn, rapeseed, and sunflower classes). Second, this may be due to the fact that the first order transitions of annual crops are less stable and highly variable with agricultural practices and operators in this area. Hence, temporal modeling does not add useful information and may even wrongly correct an initially correct parcel-wise prediction.

As for Site77, similarly to Site04, the best improvements occur on permanent crops, such as meadows and fruit trees (cf. Table 5). Moreover, the temporal structure improved the prediction of some annual crops, such as other cereals, rapeseeds, and proteins since they have a high first order transition probability to other cereals. The prediction of forage crops is also highly improved using crop rotations information.

On both sites, including rotation knowledge improved the overall accuracy of crop classification. The proposed model is a trade-off between observation-based classification and temporal regularization using learned rotation knowledge. If the precision of observation-based classification is already high and the transition patterns inconclusive or poorly followed, integrating rotation knowledge may decrease the accuracy. However, ambiguous observation-based prediction can be improved by modeling the temporal structure, especially if the temporal aspect is very influential, as with permanent crops or crops alternating with other cereals. The detrimental effect of temporal modeling on some annual crops were can also be explained by the limited availability LPIS (only one edition, 2016, was available at the time), which might not be sufficient to model crop rotation schemes occurring over two or three years. Indeed, in this paper, only first order crop rotation was modeled. However, our approach could be straightforwardly extended to rotations over multiple years, provided more data is available. Further tests should be processed with a newer LPIS edition and over larger areas in order to assess the effect of modeling the temporal structure.

Conclusion and Perspectives

This study focused on improving the automatic prediction of crop types using Sentinel-1 and -2 time series and learned rotation knowledge. This study demonstrated the efficiency of multi-temporal and multi-modal Sentinel (optical and radar) images for crop type classification using a fine nomenclature (>10 classes) and without filtering small parcels. The joint use of optical and radar features ensured more stable and accurate results. However, results varied highly depending on sites depending on cloud cover, crop types, and parcel size.

We modeled the temporal structure (i.e., crop knowledge) with conditional random fields and automatically learning the probability of crop rotations from previous LPIS editions. This rotation knowledge markedly improved the prediction of crop types. However, while a positive impact is demonstrated on permanent crops using first order crop transitions; this impact is fairly limited or even detrimental for some annual crops. Higher transition orders should be investigated to confirm the interest of temporal structure for annual crops and larger areas with more representative classes should be used. Finally, thanks to the growing volume of available LPIS data and the free availability of numerous Sentinel images, deep learning approaches for both parcel-wise feature extraction and temporal modeling should be investigated.

Acknowledgments

This work is supported by the French National Research Agency under the grant ANR-18-CE23-0023. The authors want to thank the ASP (French payment agency) and the French agricultural ministry for the rich discussions and their guidance for the nomenclature choice and crop rotation schemes.

References

- Aurdal, L., R. B. Huseby, L. Eikvil, R. Solberg, D. Vikhamar and A. Solberg. 2005. Use of hidden Markov models and phenology for multitemporal satellite image classification: Applications to mountain vegetation classification. Pages 16–18 in *Proceedings of International Workshop Analysis Multi-Temporal Remote Sensing Images*.
- Belgiu, M. and O. Csillik. 2018. Sentinel-2 cropland mapping using pixel-based and object-based time-weighted dynamic time warping analysis. *Remote Sensing of Environment* 204:509–523.
- Berzsenyi, Z., B. Györfly and D. Q. Lap. 2000. Effect of crop rotation and fertilisation on maize and wheat yields and yield stability in a long-term experiment. *European Journal of Agronomy* 13 (2):225–244.
- Boryan, C., Z. Yang, R. Mueller and M. Craig. 2011. Monitoring us agriculture: The US department of agriculture, national agricultural statistics service, cropland data layer program. *Geocarto International* 26 (5):341–358.
- Castellazzi, M. S., G. A. Wood, P. J. Burgess, J. Morris, K. F. Conrad and J. N. Perry. 2008. A systematic representation of crop rotations. *Agricultural Systems* 97 (1):26–33.
- Defourny, P., S. Bontemps, N. Bellemans, C. Cara, G. Dedieu, E. Guzzonato, O. Hagolle, J. Inglada, L.-t. Nicola, T. Rabaute, M. Savinaud, C. Udrou, S. Valero, A. Bégué, J.-F. Dejoux, A. El Harti, J. Ezzahar, N. Kussul, K. Labbassi, V. Lebourgeois, Z. Miao, T. Newby, A. Nyamugama, N. Sallh, A. Shelestov, V. Simonneaux, P.S. Traore, S.S. Traore and B. Koetz. 2019. Near real-time agriculture monitoring at national scale at parcel resolution: Performance assessment of the Sen2-agri automated system in various cropping systems around the world. *Remote Sensing of Environment* 221:551–568.
- Deledalle, C.-A., L. Denis, F. Tupin, A. Reigber and M. Jäger. 2015. NL-SAR: A unified nonlocal framework for resolution-preserving (pol)(in) SAR denoising. *IEEE Transactions on Geoscience and Remote Sensing* 53 (4):2021–2038.

- European Commission. 2016. Towards future Copernicus service components in support to agriculture? <https://ec.europa.eu/jrc/sites/jrcsh/files/Copernicus_concept_note_agriculture.pdf> Accessed on 7 May 2020.
- GISAT s.r.o. 2018. Sentinel-2 Agriculture: Czech Agriculture National Demonstrator (CzechAgri) Final Report. <<http://www.esa-sen2agri.org/wp-content/uploads/docs/CzechAgri%20Final%20Report%201.2.pdf>> Accessed on 7 May 2020.
- Hagolle, O., M. Huc, D. Villa Pascual and G. Dedieu. 2010. A multi-temporal method for cloud detection, applied to Formosat-2, Venus, Landsat and Sentinel-2 images. *Remote Sensing of Environment* 114 (8):1747–1755.
- Hagolle, O., M. Huc, D. Villa Pascual and G. Dedieu. 2015. A multi-temporal and multi-spectral method to estimate aerosol optical thickness over land, for the atmospheric correction of formosat-2, Landsat, Venus and Sentinel-2 images. *Remote Sensing* 7 (3):2668–2691.
- Hoberg, T., F. Rottensteiner, R. Q. Feitosa, and C. Heipke. 2015. Conditional random fields for multitemporal and multiscale classification of optical satellite imagery. *IEEE Transactions on Geoscience and Remote Sensing* 53 (2):659–673.
- Inglada, Jordi. 2016. OTB Gapfilling, a temporal gapfilling for image time series library, Zenodo. <<http://doi.org/10.5281/zenodo.45572>>.
- Inglada, J., M. Arias, B. Tardy, O. Hagolle, S. Valero, D. Morin, G. Dedieu, G. Sepulcre, S. Bontemps and P. Defourny. 2015. Assessment of an operational system for crop type map production using high temporal and spatial resolution satellite optical imagery. *Remote Sensing* 7 (9):12356–12379.
- Karlen, D. L., E. G. Hurley, S. S. Andrews, C. A. Cambardella, D. W. Meek, M. D. Duffy and A. P. Mallarino. 2006. Crop rotation effects on soil quality at three northern corn/soybean belt locations. *Agronomy Journal* 98 (3):484–495.
- Kenduiywoa, B. K., D. Bargiel and U. Soergel. 2015. Spatial-temporal conditional random fields crop classification from Terrasar-X images. *ISPRS Annals of the Photogrammetry, Remote Sensing and Spatial Information Sciences* 2 (3):79.
- Kussul, N., G. Lemoine, F. J. Gallego, S. V. Skakun, M. Lavreniuk and A. Y. Shelestov. 2016. Parcel-based crop classification in Ukraine using Landsat-8 data and Sentinel-1a data. *IEEE Journal of Selected Topics in Applied Earth Observations and Remote Sensing* 9 (6):2500–2508.
- Lee, J.-S. 1980. Digital image enhancement and noise filtering by use of local statistics. *IEEE Transactions on Pattern Analysis and Machine Intelligence* (2):165–168.
- Leite, P.B.C., R. Q. Feitosa, A. R. Formaggio, G. A. da Costa, O. Pedro, K. Pakzad and I. Del'Arco Sanches. 2011. Hidden Markov models for crop recognition in remote sensing image sequences. *Pattern Recognition Letters* 32 (1):19–26.
- Li, H., C. Zhang, S. Zhang and P. M. Atkinson. 2019. Full year crop monitoring and separability assessment with fully-polarimetric L-band UAVSAR: A case study in the Sacramento Valley, California. *International Journal of Applied Earth Observation and Geoinformation* 74:45–56.
- Liu, D., K. Song, J.R.G. Townshend and P. Gong. 2008. Using local transition probability models in Markov random fields for forest change detection. *Remote Sensing of Environment* 112 (5):2222–2231.
- Manning, C. D., P. Raghavan and H. Schütze. 2008. *Introduction to Information Retrieval*, vol. 1 (1). Cambridge, England: Cambridge University Press.
- Osman, J., J. Inglada and J.-F. Dejoux. 2015. Assessment of a Markov logic model of crop rotations for early crop mapping. *Computers and Electronics in Agriculture* 113:234–243.
- Ottosen, T.-B.Ø, S.T.E. Lommen and C. A. Skjæyth. 2019. Remote sensing of cropping practice in northern Italy using time-series from sentinel-2. *Computers and Electronics in Agriculture* 157:232–238.
- Palchowdhuri, Y., R. Valcarce-Di eiro, P. King and M. Sanabria-Soto. 2018. Classification of multi-temporal spectral indices for crop type mapping: A case study in Coalville, UK. *The Journal of Agricultural Science* 156 (1):24–36.
- Roscher, R., B. Waske and W. Förstner. 2017. Kernel discriminative random fields for land cover classification. Pages 1–5 in *Proceedings of LAPR Workshop on Pattern Recognition in Remote Sensing (PRRS)*.
- Sen2-Agri. Czech agriculture national demonstrator - final report, 2018. <<http://www.esa-sen2agri.org/wp-content/uploads/docs/CzechAgri%20Final%20Report%201.2.pdf>> Accessed on February 6, 2018
- Siachalou, S.u, G. Mallinis and M. Tsakiri-Strati. 2015. A hidden Markov models approach for crop classification: Linking crop phenology to time series of multi-sensor remote sensing data. *Remote Sensing*, 7 (4): 3633–3650.
- Veloso, A., S. Mermoz, A. Bouvet, T. Le Toan, M. Planells, J.-F. Dejoux and E. Ceschia. 2017. Understanding the temporal behavior of crops using Sentinel-1 and Sentinel-2-like data for agricultural applications. *Remote Sensing of Environment* 199:415–426.
- Vuolo, F., M. Neuwirth, M. Immitzer, C. Atzberger, and W.-T. Ng. 2018. How much does multi-temporal Sentinel-2 data improve crop type classification? *International Journal of Applied Earth Observation and Geoinformation* 72:122–130.
- Wagner, B. N. and B. Waske. 2018. Combining Sentinel-1 and Sentinel-2 data for improved land use and land cover mapping of monsoon regions. *International Journal of Applied Earth Observation and Geoinformation* 73:595–604.
- Whelen, T. and P. Siqueira. 2017. Use of time-series L-band UAVSAR data for the classification of agricultural fields in the San Joaquin Valley. *Remote Sensing of Environment* 193:216–224.

Advertise in the #1 publication in the imaging and geospatial information industry!



Impact Factor (2018): 3.15

PE&RS (*Photogrammetric Engineering & Remote Sensing*) is the official journal of the American Society for Photogrammetry and Remote Sensing—the Imaging and Geospatial Information Society (ASPRS). This highly respected publication is the #1 publication in the industry by a wide margin. Advertisers with a desire to reach this market can do no better than PE&RS. It delivers the right audience of professionals who are loyal and engaged readers, and who have the purchasing power to do business with you.

PE&RS Readership Highlights

Circulation: 3,000
Total audience: 6,400*

Founded in 1934, the American Society for Photogrammetry and Remote Sensing (ASPRS) is a scientific association serving professional members throughout the world. Our mission is to advance knowledge and improve understanding of mapping sciences to promote the responsible applications of photogrammetry, remote sensing, geographic information systems (GIS), and supporting technologies.

Our members are analysts/specialists, educators, engineers, managers/administrators, manufacturers/ product developers, operators, technicians, trainees, marketers, and scientists/researchers. Employed in the disciplines of the mapping sciences, they work in the fields of Agriculture/Soils, Archeology, Biology, Cartography, Ecology, Environment, Forestry/Range, Geodesy, Geography, Geology, Hydrology/Water Resources, Land Appraisal/ Real Estate, Medicine, Transportation, and Urban Planning/Development.

RESERVE YOUR SPACE TODAY!

Bill Spilman, ASPRS Advertising, Exhibit Sales & Sponsorships
(877) 878-3260 toll-free
(309) 483-6467 direct
(309) 483-2371 fax
bill@innovativemediasolutions.com

	Corporate Member Exhibiting at a 2019 ASPRS Conference	Corporate Member	Exhibitor	Non Member
<i>All rates below are for four-color advertisements</i>				
Cover 1	\$1,850	\$2,000	\$2,350	\$2,500
<i>In addition to the cover image, the cover sponsor receives a half-page area to include a description of the cover (maximum 500 words). The cover sponsor also has the opportunity to write a highlight article for the journal. Highlight articles are scientific articles designed to appeal to a broad audience and are subject to editorial review before publishing. The cover sponsor fee includes 50 copies of the journal for distribution to their clients. More copies can be ordered at cost.</i>				
Cover 2	\$1,500	\$1,850	\$2,000	\$2,350
Cover 3	\$1,500	\$1,850	\$2,000	\$2,350
Cover 4	\$1,850	\$2,000	\$2,350	\$2,500
Advertorial	1 Complimentary Per Year	1 Complimentary Per Year	\$2,150	\$2,500
Full Page	\$1,000	\$1,175	\$2,000	\$2,350
2 page spread	\$1,500	\$1,800	\$3,200	\$3,600
2/3 Page	\$1,100	\$1,160	\$1,450	\$1,450
1/2 Page	\$900	\$960	\$1,200	\$1,200
1/3 Page	\$800	\$800	\$1,000	\$1,000
1/4 Page	\$600	\$600	\$750	\$750
1/6 Page	\$400	\$400	\$500	\$500
1/8 Page	\$200	\$200	\$250	\$250
Other Advertising Opportunities				
Wednesday Member Newsletter Email Blast	1 Complimentary Per Year	1 Complimentary Per Year	\$600	\$600

A 15% commission is allowed to recognized advertising agencies

THE MORE YOU ADVERTISE THE MORE YOU SAVE! PE&RS offers frequency discounts. Invest in a three-times per year advertising package and receive a 5% discount, six-times per year and receive a 10% discount, 12-times per year and receive a 15% discount off the cost of the package.

*Based on 2 readers per copy as well as online views | Source: PE&RS Readership Survey, Fall 2012

Improved Depth Estimation for Occlusion Scenes Using a Light-Field Camera

Changkun Yang, Zhaoqin Liu, Kaichang Di, Changqing Hu, Yexin Wang, and Wuyang Liang

Abstract

With the development of light-field imaging technology, depth estimation using light-field cameras has become a hot topic in recent years. Even through many algorithms have achieved good performance for depth estimation using light-field cameras, removing the influence of occlusion, especially multi-occlusion, is still a challenging task. The photo-consistency assumption does not hold in the presence of occlusions, which makes most depth estimation of light-field imaging unreliable. In this article, a novel method to handle complex occlusion in depth estimation of light-field imaging is proposed. The method can effectively identify occluded pixels using a refocusing algorithm, accurately select unoccluded views using the adaptive unoccluded-view identification algorithm, and then improve the depth estimation by computing the cost volumes in the unoccluded views. Experimental results demonstrate the advantages of our proposed algorithm compared with conventional state-of-the-art algorithms on both synthetic and real light-field data sets.

Introduction

Light fields (Levoy and Hanrahan 1996) capture not only the radiance but the angular direction of each ray from a scene. Therefore, they can depict the 3D structure of the scene. As a device to acquire a light field, light-field cameras from companies such as Lytro (Ng *et al.* 2005) and Raytrix (<https://raytrix.de>) have drawn wide attention in computational photography, computer vision, and close-range photogrammetry. Compared with traditional cameras, light-field cameras place a microlens array between the main lens and the charge-coupled device array, as shown in Figure 1. Thanks to this microlens array, the light-field camera is capable of capturing multiple views of the scene in a single snapshot, enabling passive depth estimation, which has wide potential applications including autonomous vehicles (Menze and Geiger 2015), light-field segmentation (Mihara *et al.* 2016), 3D reconstruction (Kim *et al.* 2013), and simultaneous localization and mapping (Dong *et al.* 2013).

Depth estimation from light-field cameras is based on a common assumption that when refocused to the correct depth of one spatial pixel in the center subaperture image, all viewpoints (angular pixels) converge to the same point in the scene (Figure 2). If we collect the angular pixels to form an angular patch, they exhibit photo-consistency for Lambertian

Changkun Yang is with the State Key Laboratory of Remote Sensing Science, Aerospace Information Research Institute, Chinese Academy of Sciences, Beijing, China; and the Beijing Institute of Aerospace Control Devices, Beijing, China.

Zhaoqin Liu, Kaichang Di, Yexin Wang, and Wuyang Liang are with the State Key Laboratory of Remote Sensing Science, Aerospace Information Research Institute, Chinese Academy of Sciences, Beijing, China (liuzq@radi.ac.cn).

Changqing Hu is with the Beijing Institute of Aerospace Control Devices, Beijing, China; and the Pilot National Laboratory for Marine Science and Technology, Qingdao, China.

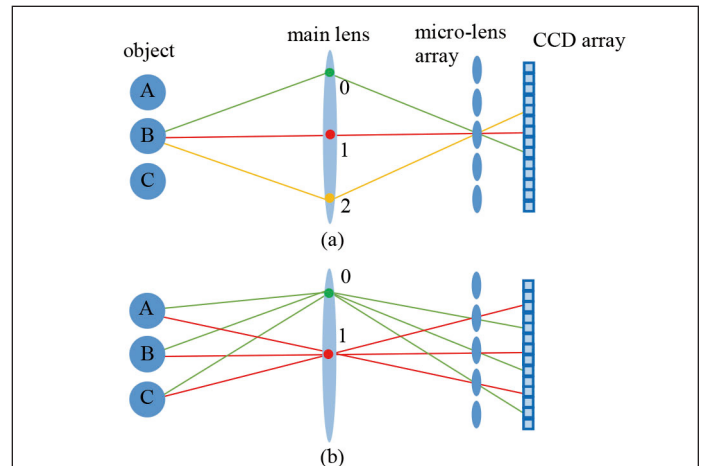


Figure 1. Imaging model of a lenslet light-field camera. (a) The different direction rays (red, green, and yellow lines) from object *B* are recorded in different pixels in the charge-coupled device array. 0, 1, and 2 represent different locations on the main lens. Location 1 is the center of the main lens. (b) The rays passing through the same location on the main lens are collected to form subaperture images. The subaperture image formed by the rays passing through location 1 on the main lens is called the center subaperture image.

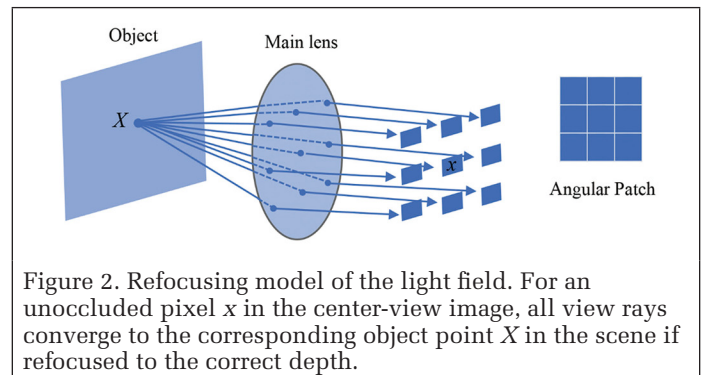


Figure 2. Refocusing model of the light field. For an unoccluded pixel *x* in the center-view image, all view rays converge to the corresponding object point *X* in the scene if refocused to the correct depth.

surfaces, which means their colors ought to be the same or similar. In setting a different refocusing depth, the depth corresponding to the minimum variance of the angular patch is the correct one. Many algorithms have been proposed for depth estimation from light-field cameras under this assumption. Perwaß and Wietzke (2012) proposed an algorithm to estimate depth from light-field cameras using correspondence techniques. Wanner and Goldluecke (2013) proposed a local

Photogrammetric Engineering & Remote Sensing
Vol. 86, No. 7, July 2020, pp. 443–456.
0099-1112/20/443–456

© 2020 American Society for Photogrammetry
and Remote Sensing
doi: 10.14358/PERS.86.7.443

depth-estimation algorithm using a structure tensor to compute directions of feature pixels in an epipolar plane image (EPI). Yu *et al.* (2013) analyzed the 3D geometry of lines in a light-field image and encoded the line constraints to improve the disparity map. Tao *et al.* (2013) combined defocus and correspondence cues to estimate scene depth using EPIs, and optimized the depth map using a Markov random field (MRF). Tosić and Berkner (2014) estimated depth by defining a description of EPI texture and mapping this texture to scale-depth space. Sabater *et al.* (2015) proposed a depth-estimation algorithm based on block matching using subaperture images without demosaicking. Compared with these algorithms, Jeon *et al.* (2015), Zhang Liu, and Dai (2015), and Yang *et al.* (2019) improved depth accuracy by achieving the subpixel displacement estimation of subaperture images using the phase-shift theorem. However, none of these algorithms consider occlusion, and they would provide oversmooth results at occlusion boundaries. Kim *et al.* (2013) computed reliable depth estimation around object boundaries using densely sampled light fields and implicitly handled occlusions. Chen *et al.* (2014) introduced a bilateral consistency metric on the surface camera to estimate depth in the presence of occlusions. However, the occlusion problem is solved there in images with a wide baseline in the two algorithms, which is not applicable to images acquired by a single light-field camera at one position.

When a pixel is occluded, the photo-consistency assumption no longer holds, since some viewpoints will be blocked by the occluder. Enforcing photo-consistency on the occluded pixels will lead to an incorrect depth result, causing oversmoothing around the sharp occlusion boundaries. In order to solve the occlusion problem, T.-C. Wang *et al.* (2016) proposed a single-occluder occlusion theory and derived the occluder consistency between the spatial and angular patches for the occluded pixels—i.e., when refocused to the correct depth, the angular patch can be separated into occluded and unoccluded views by a line which has the same orientation as the occlusion edge. The algorithm selects the occluded pixels by dilating the edge detected by the Canny edge detector in the center-view image, extracts the unoccluded views of the occluded pixels according to the occluder consistency, and improves depth estimation by computing the cost only in unoccluded views. However, the proposed occluder consistency is unsuitable for multi-occluder occlusion because the occluded and unoccluded views in the angular patch cannot be simply divided into two regions by a straight line in a multi-occluder situation.

Zhu, Wang, and Yu (2017) derived the occluder consistency between the spatial and angular patches for multi-occluder occlusion—i.e., the corresponding views of the occluder are the occluded views, and the corresponding views of the background are unoccluded views. The occluded and unoccluded views in the angular patch of an occluded pixel correspond to the regions that the spatial patch of the pixel is divided into. In order to obtain the unoccluded views of each pixel at occlusion boundaries, that algorithm divides the spatial patch of the pixel into two regions using *k*-means clustering according to the occluder consistency, with the occluded and unoccluded views in the angular patch of the pixel corresponding to the two regions. For each pixel around an occlusion edge, the algorithm finds two edge pixels closest to the pixel, and the unoccluded views of the pixel are obtained by finding the intersection of the unoccluded views of the two edge pixels; this is called *voting strategy*. However, the selection of unoccluded views in this method is unsatisfactory in a complex-textured region for two reasons. First, the *k*-means clustering requires specifying the number of clusters in advance, which may be different from the actual number of clusters, which would make the clustering results

inaccurate. Second, the voting strategy to obtain unoccluded views for the pixels around the occlusion boundaries is not very effective in regions with complex textures. A consensus on depth estimation in computer vision is that more effective views lead to more accurate depth estimation. The key to getting an accurate depth map is to select correct unoccluded views. However, it is difficult to effectively select unoccluded views in complex-textured regions based on prior methods. Therefore, we propose an algorithm to accurately select the unoccluded views in the angular patch.

In addition, the method identifying the occluded pixels by dilating the edge pixels in the algorithms by T.-C. Wang *et al.* (2016) and Zhu *et al.* (2017) results in many unoccluded pixels being included among the selected occluded pixels, so that the step of selecting unoccluded views from the angular patch for occluded pixels has also been done for the selected unoccluded pixels—which is unnecessary, because all views in the angular patch of the unoccluded pixels are unoccluded views. Moreover, since the selected unoccluded views are only a portion of all the unoccluded views, using them to estimate the depth of the unoccluded pixels in these algorithms decreases the depth accuracy. Therefore, effectively identifying the occluded pixels is very important.

Different from the methods of T.-C. Wang *et al.* (2016) and Zhu *et al.* (2017), Schilling *et al.* (2018) used EPIs to handle occlusion. By integrating the occlusion handling, their method improved performance for object borders and smooth surface reconstruction. Besides the conventional methods, deep-learning methods have been used in depth estimation in light fields. Shin *et al.* (2018) achieved fast and accurate depth estimation based on a fully convolutional neural network and proposed a data-augmentation method to overcome the lack of training data. Tsai *et al.* (2020) proposed an attention-based view-selection network for light-field depth estimation and improved accuracy by using the views more effectively and reducing redundancy within views.

In this article, we explicitly take occlusion into account. By effectively identifying the occluded pixels and accurately selecting the unoccluded views in complex-textured regions, we obtain accurate depth for multi-occluder occlusion boundaries. Our main contributions are the following:

- We present an algorithm to effectively identify occluded pixels, improving depth accuracy.
- We propose an algorithm to accurately select the unoccluded views in the angular patch, obtaining more accurate unoccluded views compared with prior methods.
- We propose an algorithm to accurately estimate depth which can preserve occlusion boundaries.

In the next section, we introduce the single-occluder and multi-occluder occlusion models. Then an accurate depth-estimation method for multi-occluder occlusion is proposed and elucidated: First the occluded pixels are effectively identified, and then the unoccluded views for occluded pixels are accurately selected. Third, the initial depth map is improved by computing the cost volumes in the unoccluded views. Finally, we refine the depth with MRF regularization. In the section after that, we demonstrate the advantages of our proposed method compared with state-of-the-art algorithms quantitatively and qualitatively.

Light-Field Occlusion Theory

In this section, the single-occluder and multi-occluder occlusion models are introduced. T.-C. Wang *et al.* (2016) developed a light-field single-occluder occlusion model based on the physical image formation and proved the occluder consistency for single-occluder occlusion. Each pixel on the occlusion edge is assumed to be occluded by only one occluder.

When refocused to the occluded plane, the edge separating the occluded and unoccluded pixels in the angular patch has the same orientation as the occlusion edge in the spatial patch (Figure 3). Moreover, photo-consistency will still hold for the angular patch in the unoccluded views. However, the single-occluder model fails in multi-occluder occlusion.

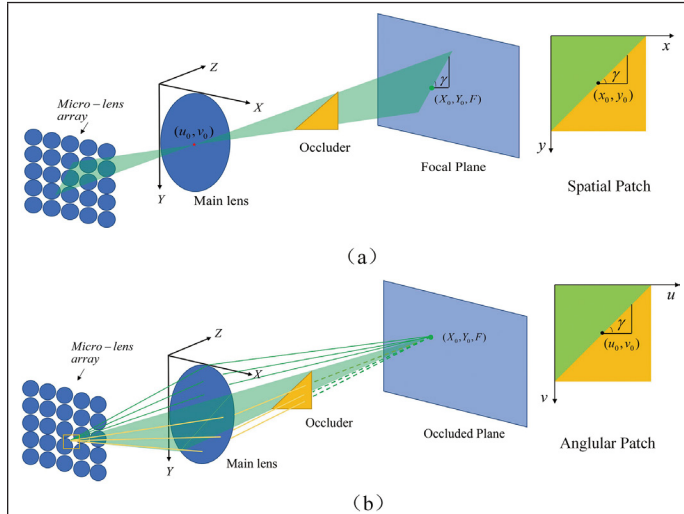


Figure 3. The single-occluder occlusion model of the light field (T.-C. Wang *et al.*, 2016). The left part of (a) shows pinhole imaging at the central view (u_0, v_0) . The right part of (a) shows a spatial patch centered at (x_0, y_0) in the center-view image. An occlusion edge on the spatial patch corresponds to an occluding plane in the 3D space with orientation γ . The left part of (b) shows a refocusing at the occluded plane. Only the views above the occluder (green rays) can observe the 3D point (X_0, Y_0, F) ; other views are blocked by the occluder. The right part of (b) shows the corresponding angular patch of (x_0, y_0) . The orientation of the edge separating the occluded views (yellow region) and unoccluded views (green region) in the angular patch is γ .

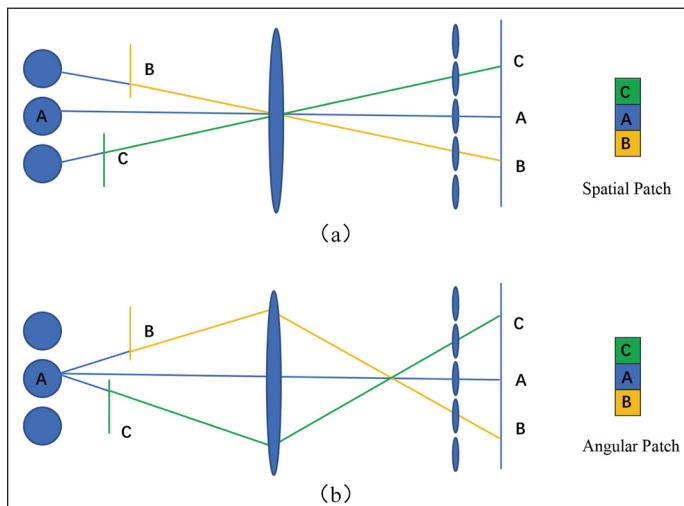


Figure 4. The multi-occluder occlusion model of the light field. The left part of (a) shows pinhole imaging at the center view. The right part of (a) shows a spatial patch (1D) centered at A in the center-view image. The left part of (b) shows a refocusing at object A. Only the center view can observe the object A; other views are blocked by the occluder. The right part of (b) shows the corresponding angular patch of pixel A.

Zhu *et al.* (2017) explored the multi-occluder occlusion model in the light field and proved the occluder consistency between the spatial and angular patches for multi-occluder occlusion. When refocused to the correct depth of the occluded pixel, the occluded views in the angular patch are the reprojections of the occluder in the spatial space. The unoccluded views are the corresponding views of the background. Therefore, the angular patch is similar to the spatial patch (Figure 4). For more complex multi-occlusion (Figure 5), the occluder consistency proved correct in that article. The -occluder consistency for single-occluder occlusion is the special case of the occluder consistency for multi-occluder occlusion.

The correctness of the occluder consistency in multi-occluder occlusion is demonstrated on a Mona data set (Wanner, Meister, and Goldluecke 2013) in Figure 6. As can be seen from the figure, the angular patch is similar to the spatial patch. The occluded pixels in the angular patch are the reprojection of the occluder in the spatial space.

Depth Estimation

A new depth-estimation method is proposed in this article for multi-occluder occlusion based on the foregoing occlusion theory. The flowchart of depth estimation is shown in Figure 7. It consists of the following steps: identifying the occluded pixels with the center subaperture image; selecting the unoccluded views for the occluded pixels; obtaining the initial depth by computing the cost volumes in the unoccluded views; and regularizing the initial depth with an MRF.

Occluded-Pixel Identification

In this section, the occluded pixels are effectively identified. The initial occluded pixels are found by applying Canny edge detection on the center subaperture image. There are obviously many unoccluded pixels in the edge obtained. We identify

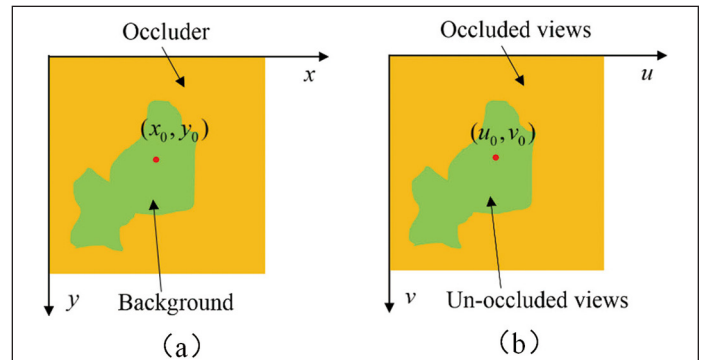


Figure 5. Complex occlusion boundary in (a) spatial patch and (b) angular patch. The yellow and green areas in (a) correspond to the occluder and background; in (b), to the occluded and unoccluded views.

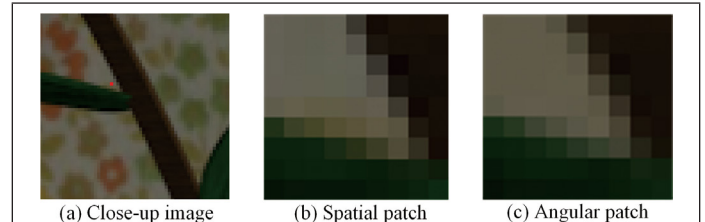


Figure 6. An example of occluder consistency. (a) The close-up image of the center-view image in the Mona data set. (b) The spatial patch of the red pixel in (a). (c) The angular patch corresponding to the red pixel when refocused to the correct depth.

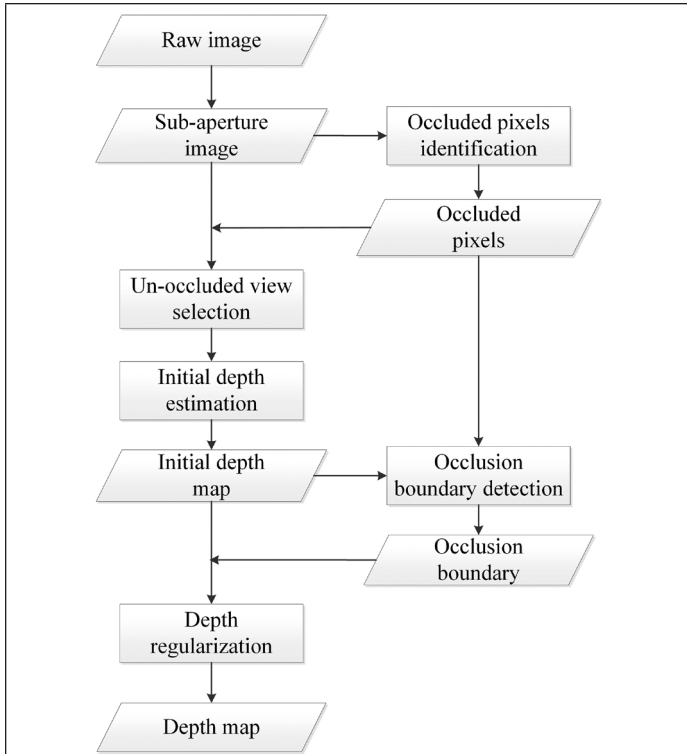


Figure 7. Flowchart of the proposed depth-estimation method.

the occluded pixels from the edge pixels using a refocusing method.

First, the orientation angle θ at each edge pixel is obtained by applying the edge-orientation predictor on the edge. Then two pixels on either side of the edge pixel are selected according to Equations 1 and 2 as shown in Figure 8. Next, one region of pixels in the angular patch of pixel p_1 is selected according to Equation 3 as shown in Figure 9a, and one region of pixels in the angular patch of pixel p_2 is selected according to Equation 4 as shown in Figure 9b.

$$\begin{cases} x_1 = \text{floor}\left(x + 2\cos\left(\theta + \frac{\pi}{2}\right) + 0.5\right) \\ y_1 = \text{floor}\left(y - 2\sin\left(\theta + \frac{\pi}{2}\right) + 0.5\right) \end{cases} \quad (1)$$

$$\begin{cases} x_2 = \text{floor}\left(x - 2\cos\left(\theta + \frac{\pi}{2}\right) + 0.5\right) \\ y_2 = \text{floor}\left(y + 2\sin\left(\theta + \frac{\pi}{2}\right) + 0.5\right) \end{cases}, \quad (2)$$

where (x_1, y_1) is the coordinates of pixel p_1 in Fig. 8, (x, y) is the coordinates of the edge pixel, and (x_2, y_2) is the coordinates of pixel p_2 .

$$x\sin\theta + y\cos\theta < 0 \quad (3)$$

$$x\sin\theta + y\cos\theta > 0 \quad (4)$$

If the edge pixel is not occluded, two pixels p_1 and p_2 on either side of the edge pixel will be at the same or similar depth; when the two regions of pixels in the angular patch refocus to the corresponding object point at the same or similar depth, the variances of the two regions will be minimal. If the edge pixel is occluded, when the pixels in one region refocus to the correct depth, having the minimum variance, the pixels in the other region still have large variance. Therefore, the refocused depth will be different when the two regions of pixels minimize variance. According to this feature, the occluded pixels can be identified from the edge pixels.

For the two pixels, we refocus to different depths using the 4D light field (Ng *et al.* 2005):

$$L_{a,j}(x, y, u, v) = L_j\left(x + u\left[1 - \frac{1}{\alpha}\right], y + v\left[1 - \frac{1}{\alpha}\right], u, v\right), \quad j = 1, 2, \quad (5)$$

where L_j is the input light field, α is the ratio of the refocused depth to the current focused depth, $L_{a,j}$ is the refocused light field, (x, y) is the spatial coordinates in the center-view image, and (u, v) is the angular coordinates. The center view is located at $(u, v) = (0, 0)$. This provides an angular patch for each depth. We first compute the means and variances of the two regions:

$$\bar{L}_{a,j} = \frac{1}{N_j} \sum_{u_j, v_j} L_{a,j}(x, y, u_j, v_j), \quad j = 1, 2 \quad (6)$$

$$V_{a,j}(x, y) = \frac{1}{N_j - 1} \sum_{u_j, v_j} \left(L_{a,j}(x, y, u_j, v_j) - \bar{L}_{a,j}(x, y)\right)^2, \quad (7)$$

where N_j is the number of pixels in region j .

Then the optimal depth of the two regions is determined as

$$\alpha_j^* = \underset{\alpha}{\text{argmin}} V_{a,j}(x, y). \quad (8)$$

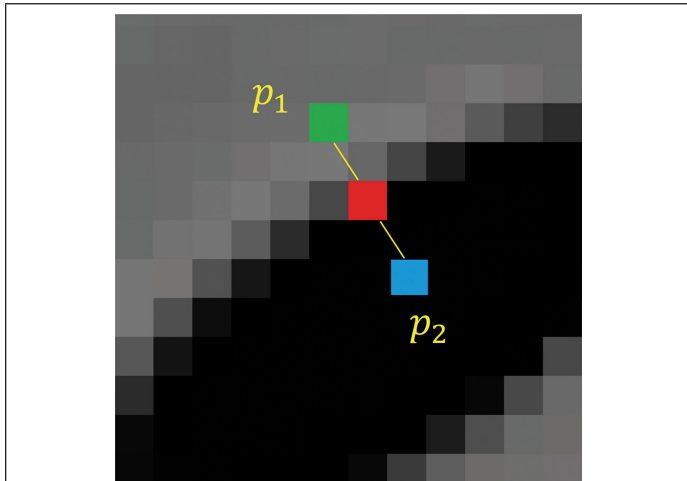


Figure 8. The selection of adjacent pixels.

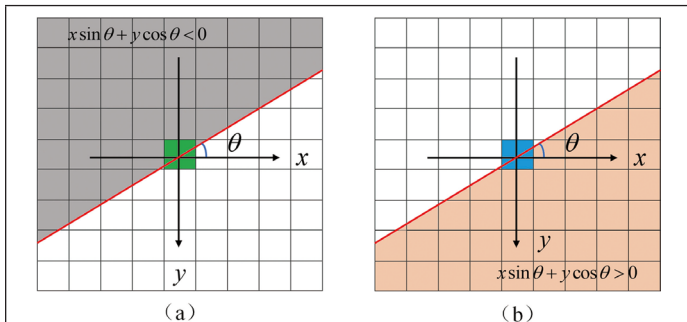


Figure 9. The selected pixels in angular patches of pixels p_1 and p_2 . (a) The gray pixels in the angular patch of pixel p_1 are selected. (b) The orange pixels in the angular patch of pixel p_2 are selected. The line equation is determined by the orientation angle θ of the edge pixel.

Finally, the occluded pixels are identified based on the discriminant formula

$$|\alpha_1^* - \alpha_2^*| > \delta, \quad (9)$$

where δ is a threshold value which is set to 5.

Some pixels which are not located in the edge are occluded in some views of the angular patch, as shown in Figure 10. In order to identify such occluded pixels, the final occluded pixels are obtained by dilating the occluded pixels identified.

An example of occluded-pixel identification is shown in Figure 11. Obviously, using our proposed method removes

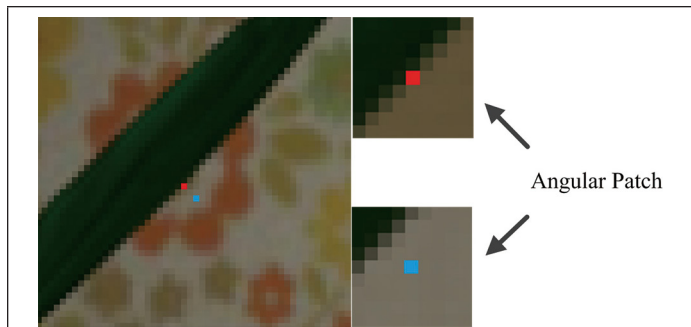


Figure 10. Occlusions around occlusion edges. The left image is the close-up of the center subaperture image, and the right images are the angular patches when the red and blue dots in the close-up image are refocused at the correct depth. The red dot is located on the occlusion edge of the center subaperture image, and its corresponding angular patch is divided into two parts on average. The lower right part is all from the unoccluded red dot, whereas the upper left part is occluded by the leaf. The blue dot is located around the occlusion edge, and some views in the upper left corner of its angular patch are also occluded.

a number of unoccluded pixels compared with the methods of T.-C. Wang *et al.* (2016) and Zhu *et al.* (2017). It can avoid selection of unoccluded views for unoccluded pixels and thus ensure the accuracy of depth estimation of the unoccluded pixels.

Unoccluded-View Selection

Because the photo-consistency assumption only holds for unoccluded views for occluded pixels, in this section unoccluded views are selected for occluded pixels, which will be used for depth estimation of occluded pixels in the next section. For the occluded pixels, the angular patch corresponds to the spatial patch according to the occluder consistency. Therefore, the angular patch can be divided into the same regions as the spatial patch. For some occluded pixels in a complex scene, spatial patches are divided into multiple regions, and the corresponding unoccluded views may correspond to a combination of several regions in the spatial patches. In order to obtain the optimal unoccluded views, an adaptive unoccluded-view selection method is proposed.

First, the spatial patch of each occluded pixel is divided into different categories by affinity-propagation clustering (Frey and Dueck 2007), an adaptive clustering algorithm that does not specify the number of clusters. Instead, the preferences p influence the final number of clusters. Usually a good choice is to set p to the median of all the similarities between data points. However, in many cases that setting cannot lead to an optimal clustering solution. According to experimental experience, we set p to two-thirds of the minimum of all the similarities between data points. The clustering result is generally two or three categories. If the spatial patch is divided into two categories, the pixels in one region that share the same label with the center pixel are labeled as the unoccluded points; the corresponding views in the angular patch are labeled as unoccluded views, as shown in Figure 12. If the spatial patch is divided into three categories, we mark the pixels sharing the same label with the center pixel as region 1 and

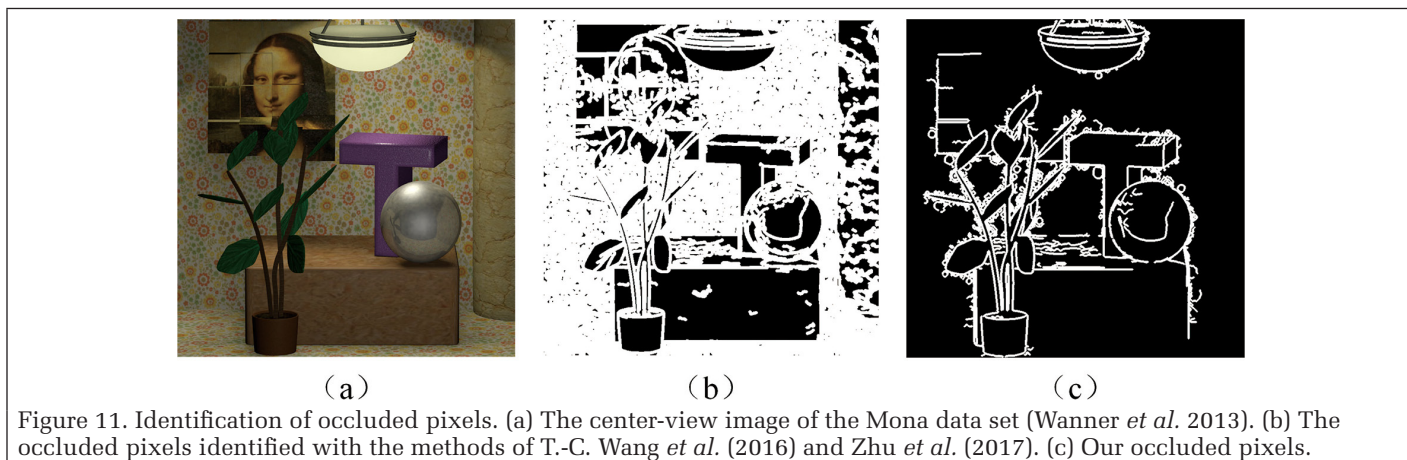


Figure 11. Identification of occluded pixels. (a) The center-view image of the Mona data set (Wanner *et al.* 2013). (b) The occluded pixels identified with the methods of T.-C. Wang *et al.* (2016) and Zhu *et al.* (2017). (c) Our occluded pixels.

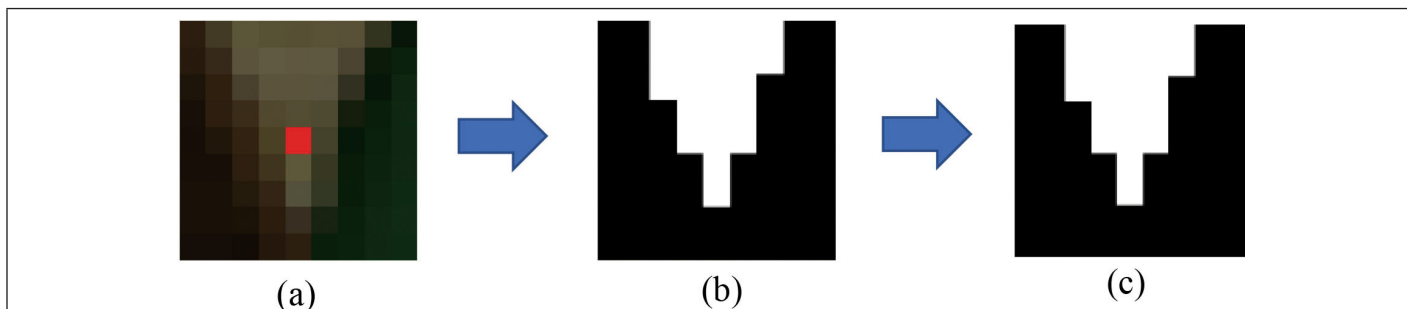


Figure 12. Selection of unoccluded views (two categories). (a) The spatial patch of one occluded pixel in the center subaperture image. (b) Two categories that the spatial patch is divided into. The pixels that share the same label with the center pixel are shown in white. (c) The angular patch. The corresponding unoccluded views are shown in white.

combine region 1 with the other two categories to get another two regions, marked as region 2 and region 3, respectively. Then the angular patch is divided into the same regions as the spatial patch and an adaptive strategy is used to obtain the optimal unoccluded views. First, we compute the means $\bar{L}_{a,j}$ and variances $V_{a,j}$ of the three regions using Equations 6 and 7. Then, we find the depth α_j^* corresponding to the minimum of the three regions using Equation 8. The minimum variance and mean corresponding to the depth α_j^* are

$$V_{\min,j} = V_{\alpha_j^*,j}(x, y) \quad (10)$$

$$\bar{L}_j = \bar{L}_{\alpha_j^*,j} \quad (11)$$

Let

$$j^* = \operatorname{argmin}_j V_{\min,j} \quad (12)$$

be the index of the region that exhibits minimum variance. If $j^* = 2$ or 3 , the region j^* in the angular patch is the optimal unoccluded views. If $j^* = 1$, the index j_u of the region corresponding to the optimal unoccluded views is selected by comparing the means of the three regions:

$$j_u = \begin{cases} 1 & \text{if } |\bar{L}_j - \bar{L}_1| > \epsilon, \quad j: j \neq 1 \\ 2 & \text{if } |\bar{L}_2 - \bar{L}_1| < \epsilon \\ 3 & \text{if } |\bar{L}_3 - \bar{L}_1| < \epsilon \end{cases}, \quad (13)$$

where ϵ is a threshold value which is set to 0.01. Now the unoccluded views of the occluded pixel are shown in Figure 13.

In order to verify the effectiveness of the proposed method to select unoccluded views, the F-measure (Sasaki 2007) of the unoccluded views in occlusion using our algorithm is computed and compared with previous work (T.-C. Wang *et al.* 2016; Zhu *et al.* 2017). The quantitative comparisons are listed in Table 1. The qualitative comparisons of the unoccluded views are shown in Figure 14.

Table 1. F-measures for unoccluded-view selection.

Method	Data Set						
	Buddha	Mona	Medieval	Horse	StillLife	Papillon	Average
T.-C. Wang <i>et al.</i> (2016)	0.61	0.65	0.52	0.56	0.54	0.59	0.58
Zhu <i>et al.</i> (2017)	0.70	0.75	0.61	0.61	0.68	0.71	0.68
Ours	0.78	0.83	0.80	0.80	0.78	0.79	0.80

As can be seen from Table 1 and Figure 14, our algorithm can select more accurate unoccluded views and has more obvious advantages in the multi-occluder areas. The unoccluded views selected in the method of T.-C. Wang *et al.* (2016) always include some occluded views, resulting in oversmoothness in the multi-occluded areas. The method of Zhu *et al.* (2017) selects more accurate unoccluded views, but its accuracy is lower than that of our algorithm. In the StillLife data set, the red point in the yellow box is occluded by two objects. The selection of unoccluded views in the methods of T.-C. Wang *et al.* and Zhu *et al.* fail, while our algorithm still selects the most accurate unoccluded views. In the Horses data set, there are many textures near the occluded points in the background (the red, green, and yellow boxes), and the methods of T.-C. Wang *et al.* and Zhu *et al.* select some occluded views. Although our method does not select all the unoccluded views, the selected views are all unoccluded views, which can avoid oversmoothing.

In order to eliminate the aliasing influence of edge pixels in the angular patch, selected unoccluded views corresponding to the edge pixels in the spatial patch are removed, as shown in Figure 15. Consequently, the accuracy of depth estimation can be improved using the refined unoccluded views.

Initial Depth Estimation

After selection of the unoccluded views, the initial depth map is obtained by computing the cost volumes in the unoccluded

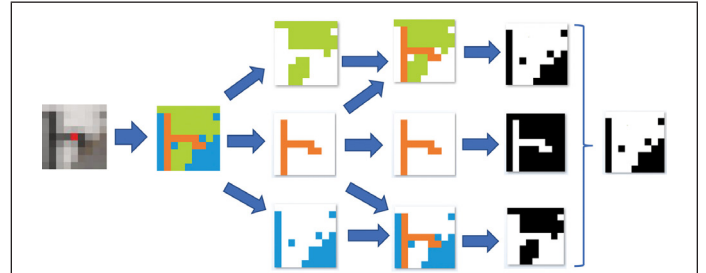


Figure 13. Selection of unoccluded views (three categories). The first two columns represent that the spatial patch of one occluded pixel is divided into three categories by affinity propagation. The third and fourth columns represent that the spatial patch is divided into three regions. The fourth and fifth columns represent that the angular patch is divided into the same regions (white) as the spatial patch. The last column represents the selected unoccluded views.

Center sub-aperture image	Close-up image	GroundTruth	Wang	Zhu	Ours
Mona					
Medieval					
StillLife					
Horses					

Figure 14. Comparisons of unoccluded-view selection. White areas denote the selected unoccluded views. All the data sets are from Wanner *et al.* (2013).

views. The cost volumes $C(x,y,l)$ are defined by combining the refocus $C_r(x,y,l)$ and correspondence $C_c(x,y,l)$ cues as

$$C(x,y,l) = \alpha C_r(x,y,l) + (1-\alpha)C_c(x,y,l) \quad (14)$$

where $\alpha \in (0,1)$ adjusts the relative importance between the defocus cost C_r and the correspondence cost C_c . Here, α is set to 0.5. The cost volumes are computed based on the subpixel shifts of subaperture images using the phase-shift theorem (Jeon *et al.* 2015):

$$I(x + \Delta x) = F^{-1} \{ F \{ I(x) \} \exp^{2\pi i \Delta x} \}, \quad (15)$$

where $I(x)$ is an image, $I(x + \Delta x)$ is the subpixel image shifted by Δx , $F\{\cdot\}$ denotes the discrete 2D Fourier transform, and $F^{-1}\{\cdot\}$ denotes the inverse discrete 2D Fourier transform. Therefore, the defocus cue is defined as

$$\bar{I}(x,y,l) = \frac{1}{N} \sum_{u,v} I_{u,v}(x + d_u, y + d_v) \quad (16)$$

$$C_r(x,y,l) = \frac{1}{N-1} \sum_{u,v} |\bar{I}(x,y,l) - I_{u,v}(x + d_u, y + d_v)|^2, \quad (17)$$

where N is the number of unoccluded views, l is the cost label, (u,v) are unoccluded views, $I_{u,v}$ denotes the images corresponding to the unoccluded views, (x,y) is the spatial coordinates, and the subpixel shifts d_u and d_v are defined as

$$\begin{bmatrix} d_u \\ d_v \end{bmatrix} = \begin{bmatrix} kl(u - u_c) \\ kl(v - v_c) \end{bmatrix}, \quad (18)$$

where k is the unit of the label in pixels and (u_c, v_c) is the center view.

The correspondence cue is defined as

$$C_c(x,y,l) = |\bar{I}(x,y,l) - I_{u_c,v_c}(x,y)|^2, \quad (19)$$

where I_{u_c,v_c} is the center-view image.

Then the initial depth map is obtained by minimizing the cost volumes:

$$I_d(x,y) = \underset{l}{\operatorname{argmin}} C(x,y,l). \quad (20)$$

Depth Regularization

In this section, the occlusion boundary is detected and the initial depth map is refined with global regularization using an energy function.

Occlusion-Boundary Detection

We find the occlusion boundary by combining the depth cues and the occluded pixels obtained previously.

For an occluded pixel in an occlusion boundary, the depth gradient is larger than for an unoccluded pixel. So we can get an initial occlusion boundary by computing and thresholding the gradient of the initial depth:

$$\operatorname{Occ_d} = \begin{cases} 1 & \text{if } \mathcal{N}\left(\frac{\nabla I_d}{I_d}\right) > \varepsilon \\ 0 & \text{if } \mathcal{N}\left(\frac{\nabla I_d}{I_d}\right) \leq \varepsilon \end{cases}, \quad (21)$$

where I_d is the initial depth and ∇I_d is the gradient of the initial depth. Since the depth gradient becomes larger as the depth becomes greater, we divide the gradient ∇I_d by I_d to increase robustness. $\mathcal{N}(\cdot)$ is a normalization function that subtracts the mean and divides by the standard deviation. Here the threshold ε is set to 1.

The occlusion boundary can be computed by

$$\operatorname{Occ} = \operatorname{Occ_d} \cap \operatorname{Occ_c}, \quad (22)$$

where $\operatorname{Occ_c}$ is the occluded pixels obtained previously. An example is shown in Figure 16.

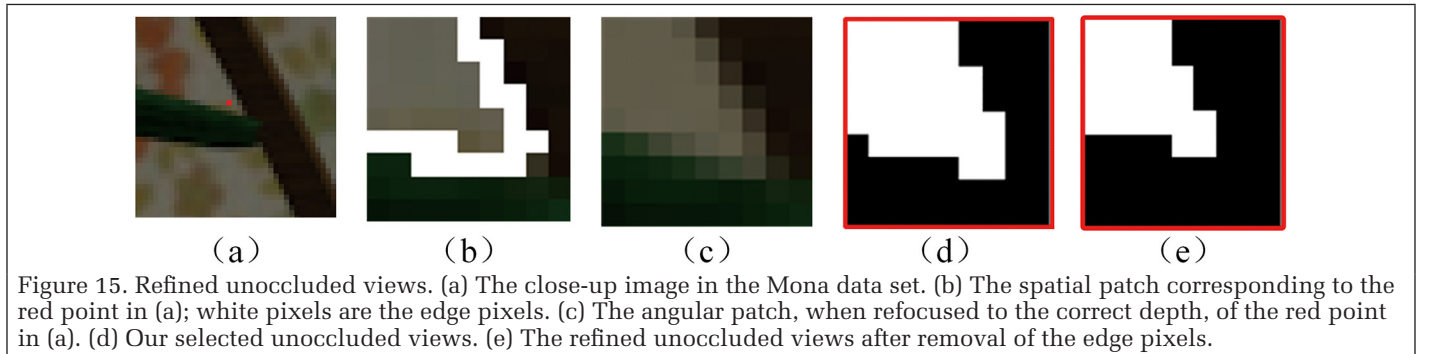


Figure 15. Refined unoccluded views. (a) The close-up image in the Mona data set. (b) The spatial patch corresponding to the red point in (a); white pixels are the edge pixels. (c) The angular patch, when refocused to the correct depth, of the red point in (a). (d) Our selected unoccluded views. (e) The refined unoccluded views after removal of the edge pixels.

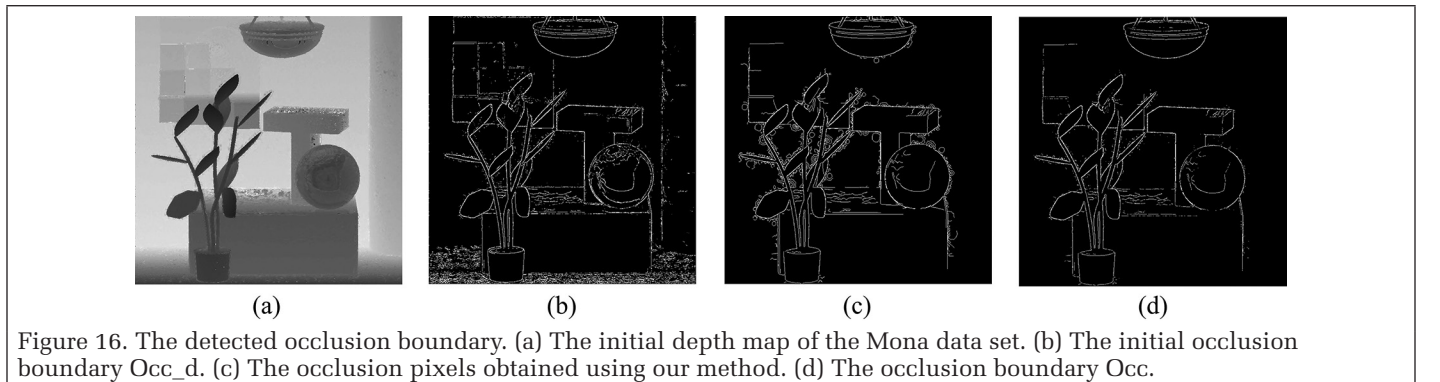


Figure 16. The detected occlusion boundary. (a) The initial depth map of the Mona data set. (b) The initial occlusion boundary $\operatorname{Occ_d}$. (c) The occlusion pixels obtained using our method. (d) The occlusion boundary Occ .

Final Depth Regularization

Given the initial depth, edge cues, and occlusion cues, we regularize the depth map with an MRF. The final depth map is obtained by minimizing the energy function:

$$I_{\text{final}} = \underset{I}{\operatorname{argmin}} \left\{ \sum_{x,y} |I(x,y) - I_d(x,y)| + \lambda \sum_{(x',y') \in \mathcal{N}(x,y)} E_{\text{smooth}}(I(x,y), I(x',y')) \right\}, \quad (23)$$

where $\mathcal{N}(x,y)$ are the neighboring pixels of (x,y) and λ is a factor to control the smooth term. The first term in Equation 23 is the data term. The smooth term means the smoothness constraint of the adjacent pixels. Similar to in Zhu *et al.* (2017), the smooth term is defined as

$$E_{\text{smooth}}(I(x,y), I(x',y')) = \varpi |I(x,y) - I(x',y')| \quad (24)$$

$$\varpi = \exp \frac{\frac{[\text{Occ}(x,y) - \text{Occ}(x',y')]^2}{2\sigma_{\text{occ}}} + \frac{[I_e(x,y) - I_e(x',y')]^2}{2\sigma_e^2} + \frac{[I(x,y) - I(x',y')]^2}{2\sigma^2}}{2}, \quad (25)$$

where I_e is the edge map of the center-view image, I is the center-view image, ϖ is a weighting function used to preserve sharp occlusion boundaries, and σ_{occ} , σ_e , and σ are three weighting factors (set to 1.6, 0.8, and 0.08, respectively, in our experiments). The minimization is solved using a standard graph-cut algorithm (Boykov, Veksler, and Zabih 2001).

Experimental Results

In this section, we first show the results of different stages of our algorithm, then demonstrate the advantages of our algorithm by comparing with different state-of-the-art algorithms.

Algorithm Stages

The results of different stages of our algorithm are shown in Figure 17. First, edge detection is applied on the center-view image (Figure 17a) to find the initial occluded pixels (Figure 17b). There are many unoccluded pixels in the edge obtained. We identify the occluded pixels from the edge using the refocusing method (Figure 17c). Then the initial depth is computed (Figure 17d) and the occlusion boundaries are detected

using the method previously explained (Figure 17e). Finally, given the initial depth and occlusion cues, we regularize the depth with an MRF for a final depth map (Figure 17f).

Comparisons

We compare our results with those of the algorithms by Tao *et al.* (2013), Jeon *et al.* (2015), T.-C. Wang *et al.* (2016), and Zhu *et al.* (2017) on synthetic data sets created by Wanner *et al.* (2013) and real-scene data sets captured by the Lytro Illum camera. The results of these algorithms can be obtained by running their public codes. In addition, we compare our method with several top-ranked methods from publications on the 4D Light Field Benchmark (Honauer *et al.* 2017), OBER-CROSS+ANP (Schilling *et al.* 2018), Epinet-fcn-m (Shin *et al.* 2018), and LFattNet (Tsai *et al.* 2020) on the training sets in the 4D Light Field Benchmark.

Synthetic Data-Set Results

The qualitative comparisons of the depth map on the data sets from Wanner *et al.* (2013) are shown in Figure 18. As we can see from the figure, the method of Tao *et al.* always gives oversmooth results in the occlusion boundaries and generates thicker structures than the ground truth. The method of Jeon *et al.* provides good results for some occlusion boundaries (the branches in Figure 18a and the close-up of the red box in Figure 18c) but gives no solution to dealing with occlusion, due to the lack of an occlusion model. Therefore, some occlusion boundaries are still oversmoothed, such as the close-ups in Figure 18b and 18d. The method of T.-C. Wang *et al.* can perform well in single-occluder areas, but it always provides oversmooth results in multi-occluder areas. The method of Zhu *et al.* can select more accurate unoccluded views than the method of T.-C. Wang *et al.* in multi-occluder areas, so it achieves better results on the depth map; however, it can select some occluded views in complex-textured regions, which leads to oversmoothing in the occlusion areas (the branches in Figure 18a and the close-up of the red box in Figure 18c).

Compared with the state-of-the-art algorithms, our proposed method yields sharper occlusion boundaries in the depth map. Our method finds more accurate occluded pixels, illustrated in close-ups of the green box in Figure 18b. The edge pixels of the black dots on the dice are identified as

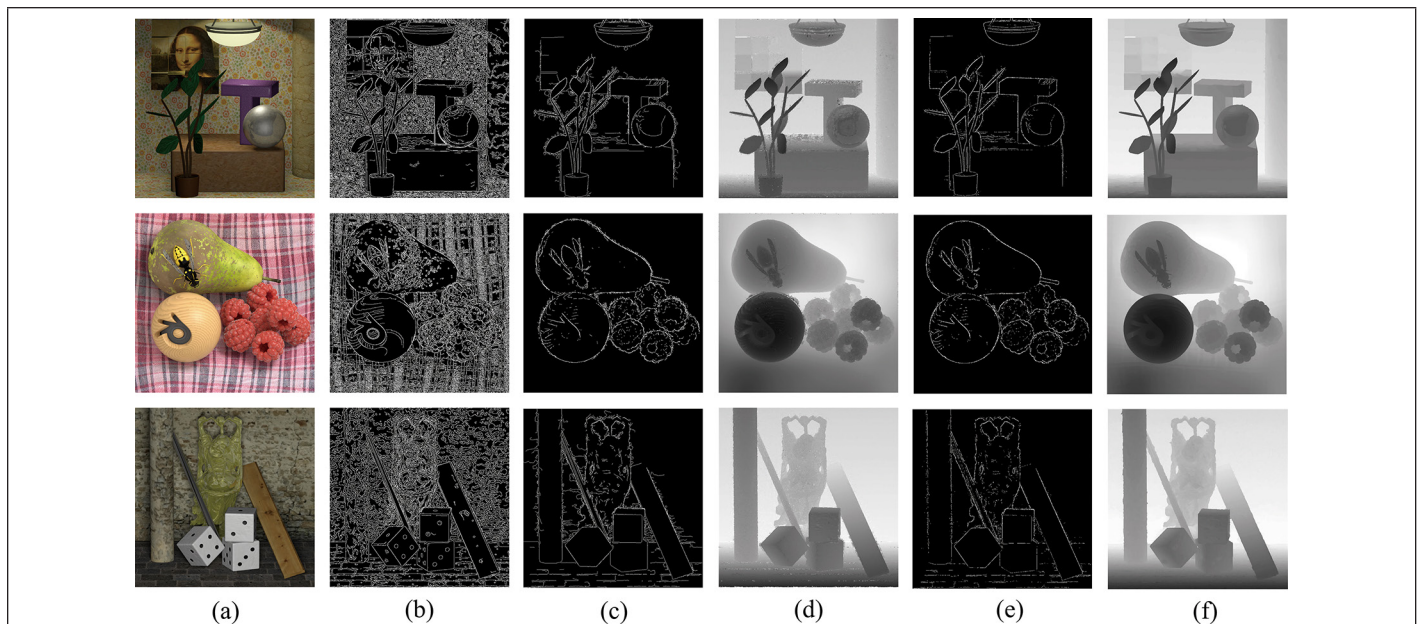


Figure 17. The results of our algorithm at different stages on synthetic data sets: (a) Center-view images, (b) edge detection, (c) occluded pixels, (d) initial depth, (e) occlusion-boundary detection, and (f) final depth.

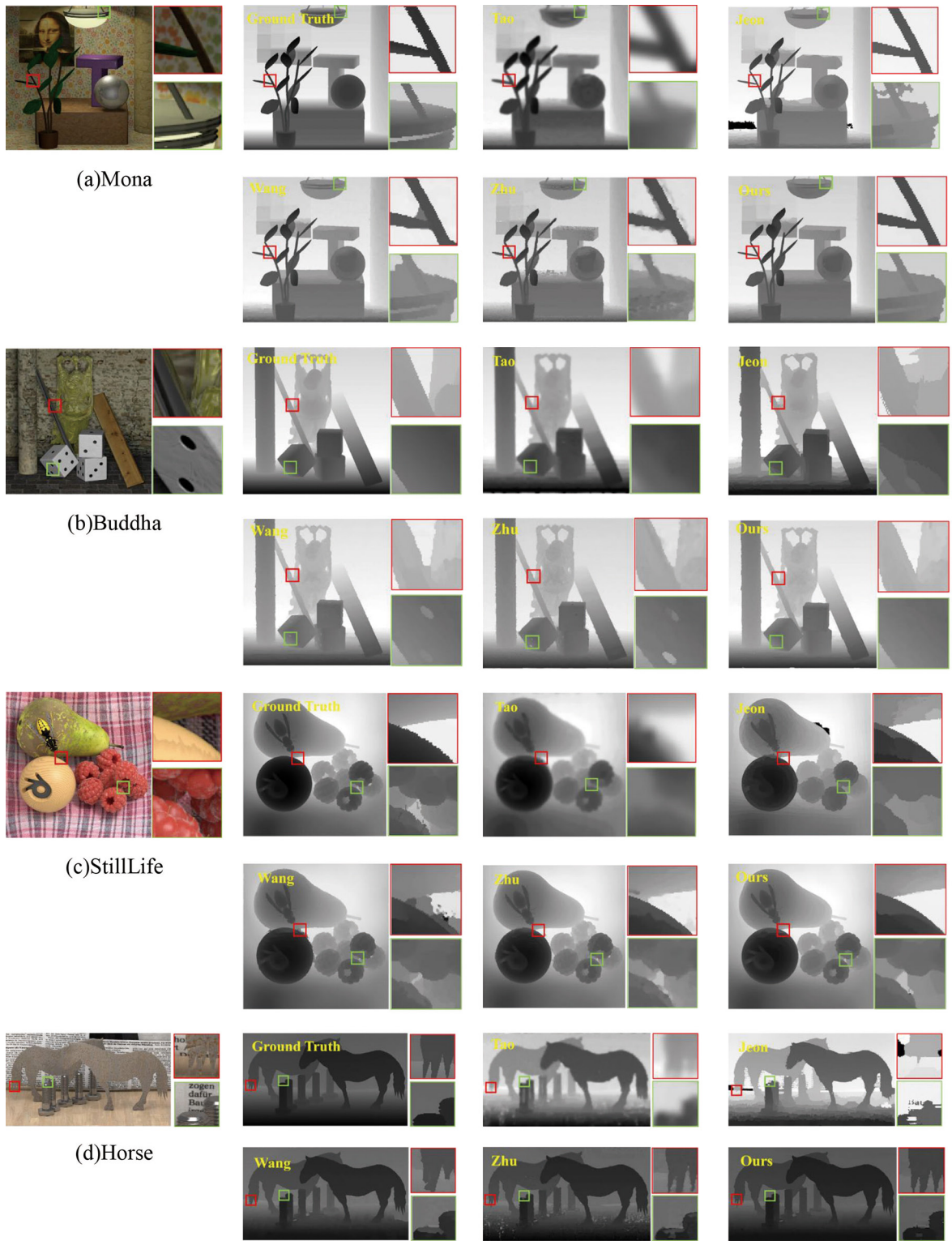


Figure 18. The depth maps of synthetic data sets: (a) Mona, (b) Buddha, (c) StillLife, and (d) Horse.

occluded pixels in other algorithms; only the selected occluded views of the occluded pixels are used to estimate depth, which leads to a reduction in depth accuracy, whereas the edge pixels are removed from the occluded pixels in our method, so all views are used to estimate depth, which improves the depth accuracy. In addition, our method selects more accurate unoccluded views and eliminates the aliasing influence of edge pixels in the angular patch by removing the views corresponding to the edge pixels in the spatial patch.

Experimental results show that our proposed method can effectively deal with complex occlusions (the branches in Figure 18a and the close-up of the red box in Figure 18c).

The quantitative comparisons of the depth map on the Wanner *et al.* data sets are shown in Figure 19. As we can see from the line charts, the error distribution concentrates toward smaller error, except for the method of Tao *et al.* (2013), and that trend is most obvious using our method. In addition, the number of large errors in the error line charts obtained by our

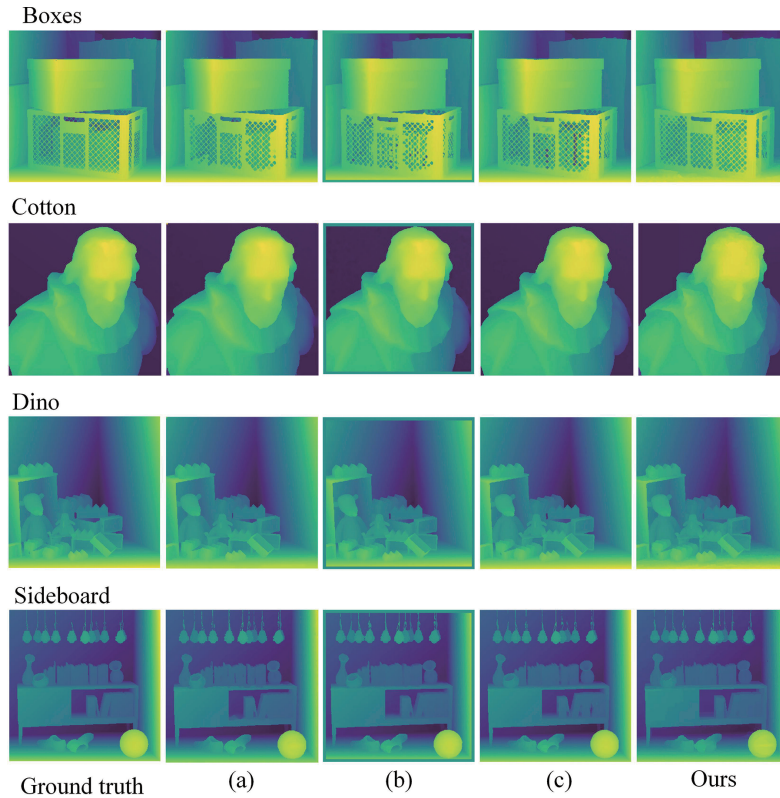


Figure 20. The estimated disparity maps of our method and comparison methods for the four scenes in the Training set. The comparison methods are (a) OBER-cross+ANP, (b) Epinet-fcn-m, and (c) LFattNet.

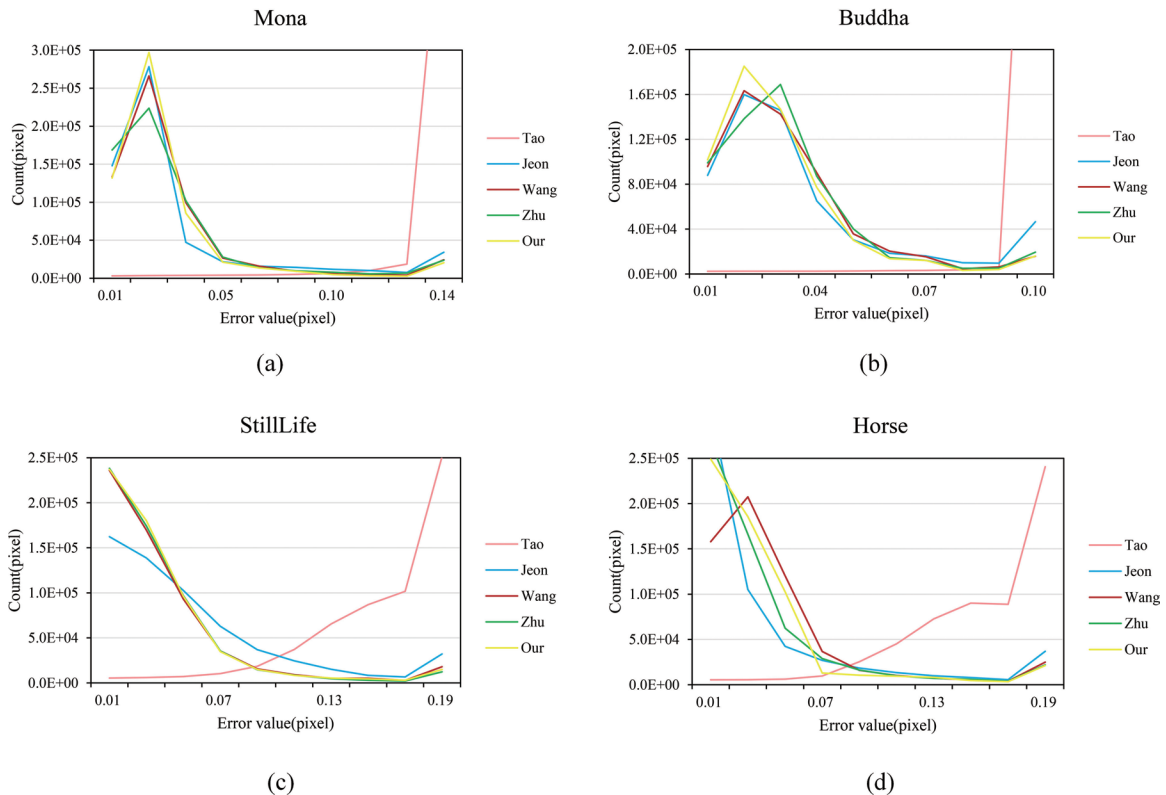


Figure 19. Error line charts: (a) Mona, (b) Buddha, (c) StillLife, and (d) Horse.

method is lower than those from other methods, further verifying the effectiveness of our method. The quantitative comparisons of the root-mean-square (RMS) errors of the depth maps are listed in Table 2. As can be seen from the table, our proposed method is superior to other advanced algorithms in accuracy: The RMS error decreases by about 15% with our proposed method compared with the best of the four other methods.

Table 2. Root-mean-square error (pixels) of depth maps.

Method	Data Set			
	Mona	Buddha	StillLife	Horse
Tao <i>et al.</i> (2013)	0.189	0.186	0.260	0.202
Jeon <i>et al.</i> (2015)	0.087	0.110	0.193	0.155
T.-C. Wang <i>et al.</i> (2016)	0.077	0.081	0.171	0.093
Zhu <i>et al.</i> (2017)	0.082	0.112	0.113	0.103
Ours	0.063	0.069	0.095	0.065

The qualitative comparisons of the depth map on training data sets from the 4D Light Field Benchmark are shown in Figure 20. Our method achieves similar visual results to the top-ranked methods.

The quantitative comparisons of the depth map are shown in Table 3. Compared with conventional methods, our method is superior in terms of mean square error to OBER-cross+ANP on the Boxes, Cotton, and Dino data sets, but inferior on the Sideboard data set. Compared with deep-learning methods, our method outperforms only Epinet-fcn-m on the Boxes data set, and m underperforms Epinet-fcn-m and LFattNet on the other data sets. However, both of those methods take about one week to train the networks on an Nvidia GTX 1080Ti graphics processing unit. The average running time of our algorithm is 1027 s. If you do not have a graphics processing unit and want to get the disparity map quickly, we think our approach is a good choice.

Table 3. Mean square error of disparity maps.

Method	Data Set			
	Boxes	Cotton	Dino	Sideboard
OBER-cross+ANP	4.750	0.555	0.336	0.941
Epinet-fcn-m	5.967	0.197	0.157	0.798
LFattNet	3.996	0.208	0.093	0.530
Ours	4.474	0.545	0.332	0.972

Real-Scene Results

In order to further verify the effectiveness of our proposed method, experiments were conducted on real-scene images captured with the Lytro Illum camera. The disparities of the images range from -1.1 to 1.1 . In order to get the ground truth of the scenes, we fixed an RGB-D camera (Kinect 2.0) on the top of the camera as shown in Figure 21.



Figure 21. The Lytro Illum camera and RGB-D camera.

First, the Lytro Illum camera was calibrated with checkerboard patterns using the Camera Calibration Toolbox for MATLAB (https://sites.google.com/site/yunsbok/lf_geo_calib) to get the interior parameters, as shown in Table 4, and sub-aperture images. Then the infrared camera of the RGB-D sensor was calibrated with checkerboard patterns to get the interior parameters as shown in Table 5. Finally, stereo calibration was performed between the center subaperture images and the infrared camera images by fixing the interior parameters of the two cameras to obtain the relative pose of the infrared camera with respect to the Lytro Illum camera, as shown in Table 6. After the calibration procedure, we registered the depth maps to the center subaperture image to get the ground truth of the scenes, as shown in Figure 22.

Table 4. The interior parameters of the Lytro Illum camera.

Parameter	Value
K_1	-13.682
K_2 (mm)	17457.348
f_x (pixels)	18935.380
f_y (pixels)	18915.222
c_x (pixels)	3566.461
c_y (pixels)	2720.078
k_1	0.472
k_2	-1.094

Table 5. The interior parameters of the infrared camera.

Parameter	Value
f_x (pixels)	371.022
f_y (pixels)	370.187
c_x (pixels)	254.828
c_y (pixels)	207.339
k_1	0.108
k_2	-0.302

Table 6. External parameters of the two cameras.

Rotation Angle ($^\circ$)	Translation (mm)
0.0165	37.0562
-0.0057	-135.3635
0.0158	-61.0438

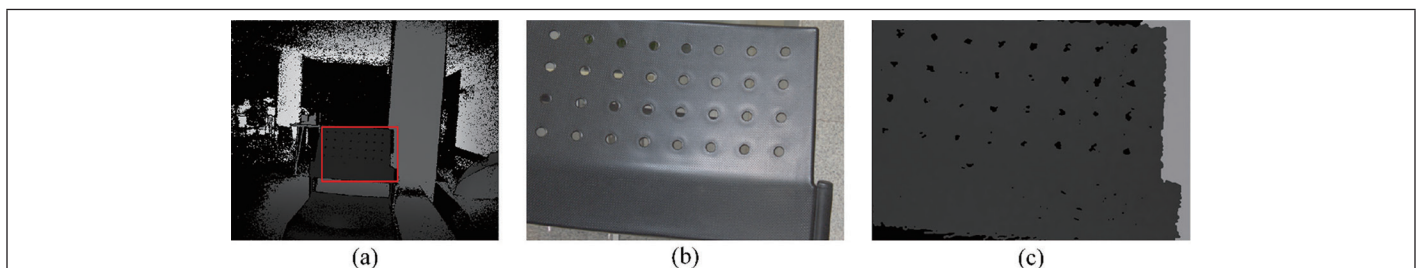


Figure 22. Obtaining the ground truth. (a) The depth map obtained by the Kinect camera. (b) The center subaperture image. (c) The ground truth of the center subaperture image.

The experimental results of the real scenes are shown in Figure 23. The method of Tao *et al.* can roughly extract the basic contour of the scenes, but the depth map is oversmooth. The method of Jeon *et al.* provides oversmooth results and fails to extract the occlusion boundaries. On the whole, the depth maps obtained by the methods of T.-C. Wang *et al.* and Zhu *et al.* are similar to that obtained by our method. To better illustrate the advantages of our method, we scale up the depth of some heavy occlusion areas. From the enlarged close-up images, it can be seen that our algorithm can preserve the occlusion boundaries well, especially for thin objects. For example, the method of T.-C. Wang *et al.* does not reconstruct all the holes in the chair (Figure 23a), and the accuracy of the method of Zhu *et al.* is less than ours; the branches in the red box of Figure 23b are not separated by either of those methods, but they are clearly distinguished by ours. The thin leaves in the green box of Figure 23b are oversmooth by the method of T.-C. Wang *et al.*, and the leaves reconstructed by the method of Zhu *et al.* are thicker than real leaves; however, our method reconstructs thin leaves. The leaves in the green box of Figure 23c are oversmooth by the method of T.-C. Wang *et al.*, and the branches in the red box of Figure 23d are oversmooth by the methods of both T.-C. Wang *et al.* and Zhu *et al.*, whereas our method restores fine branches.

The Kinect camera could not provide a refined depth map for a complex occlusion scene like Figure 22c, but we can get an accurate depth value of some pixels in the depth map to compute the depth error. The quantitative comparisons of the RMS error of the depth maps are listed in Table 7. It can

be seen from the table that the depth error of the methods of Tao *et al.* and Jeon *et al.* method is large, which is consistent with the phenomenon of oversmoothing of the two methods in Figure 23. The accuracy of the methods of T.-C. Wang *et al.* and Zhu *et al.* are lower than ours, which proves the effectiveness of our method. The RMS error decreases by about 9% with our proposed method compared with the best of the four methods.

Table 7. Root-mean-square error (mm) of the depth maps.

Method	Data Set			
	Chair	Plant1	Flower	Plant2
Tao <i>et al.</i> (2013)	382.256	189.829	165.388	175.267
Jeon <i>et al.</i> (2015)	108.246	95.562	67.280	97.476
T.-C. Wang <i>et al.</i> (2016)	89.952	52.987	65.570	68.595
Zhu <i>et al.</i> (2017)	67.848	51.953	53.795	72.821
Ours	58.019	49.176	50.354	63.176

In addition, experiments were conducted on the real data sets of the light-field camera provided by Stanford University (Raj, Lowney, and Shah 2016). Since there is no ground truth in the real-scene data, we replace the ground-truth depth with the depth map provided by commercial Lytro Illum software. Only qualitative comparisons are conducted, shown in Figure 24. It can be seen that there are a lot of single-occluder and multi-occluder areas in the real-scene images captured by

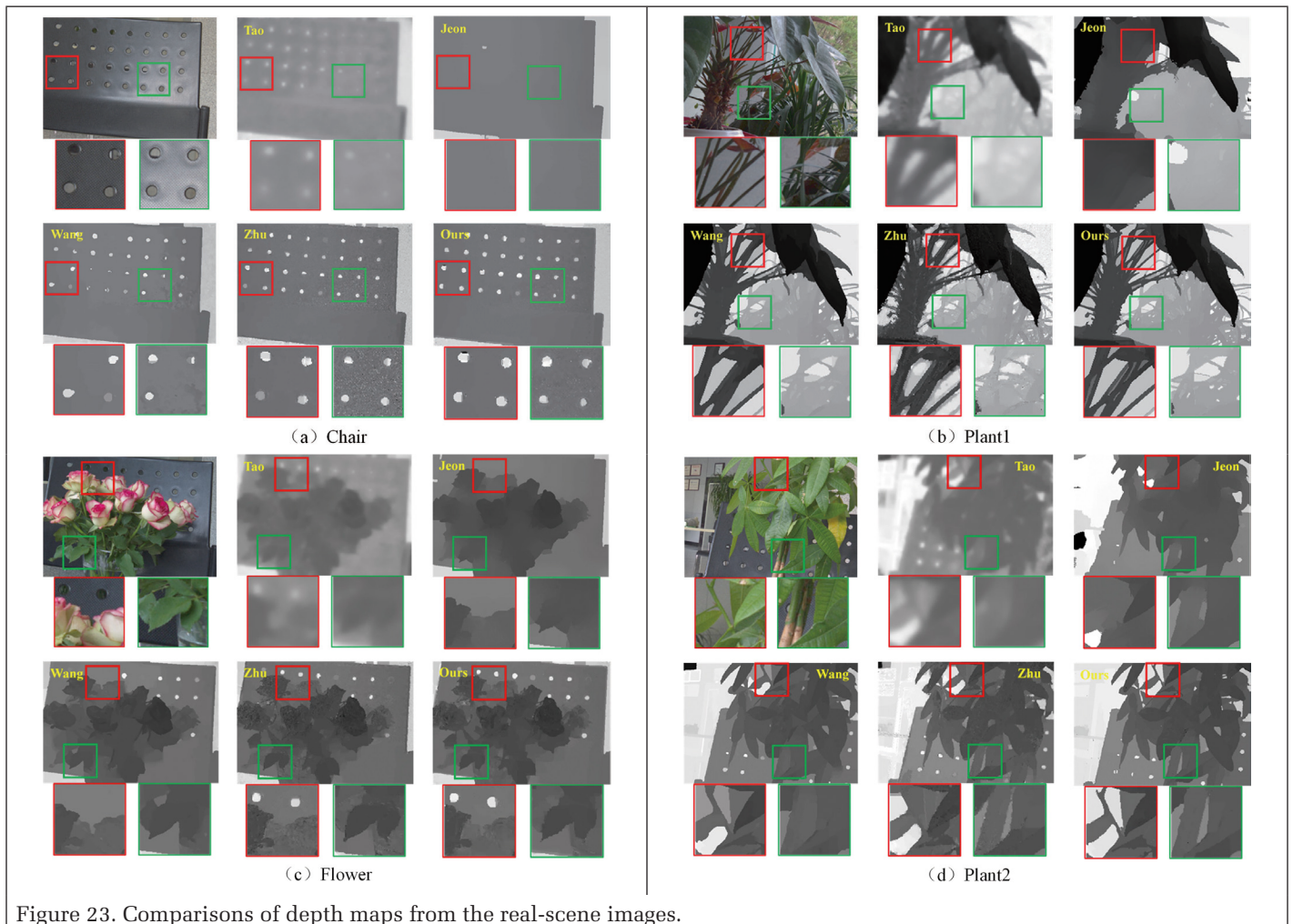


Figure 23. Comparisons of depth maps from the real-scene images.

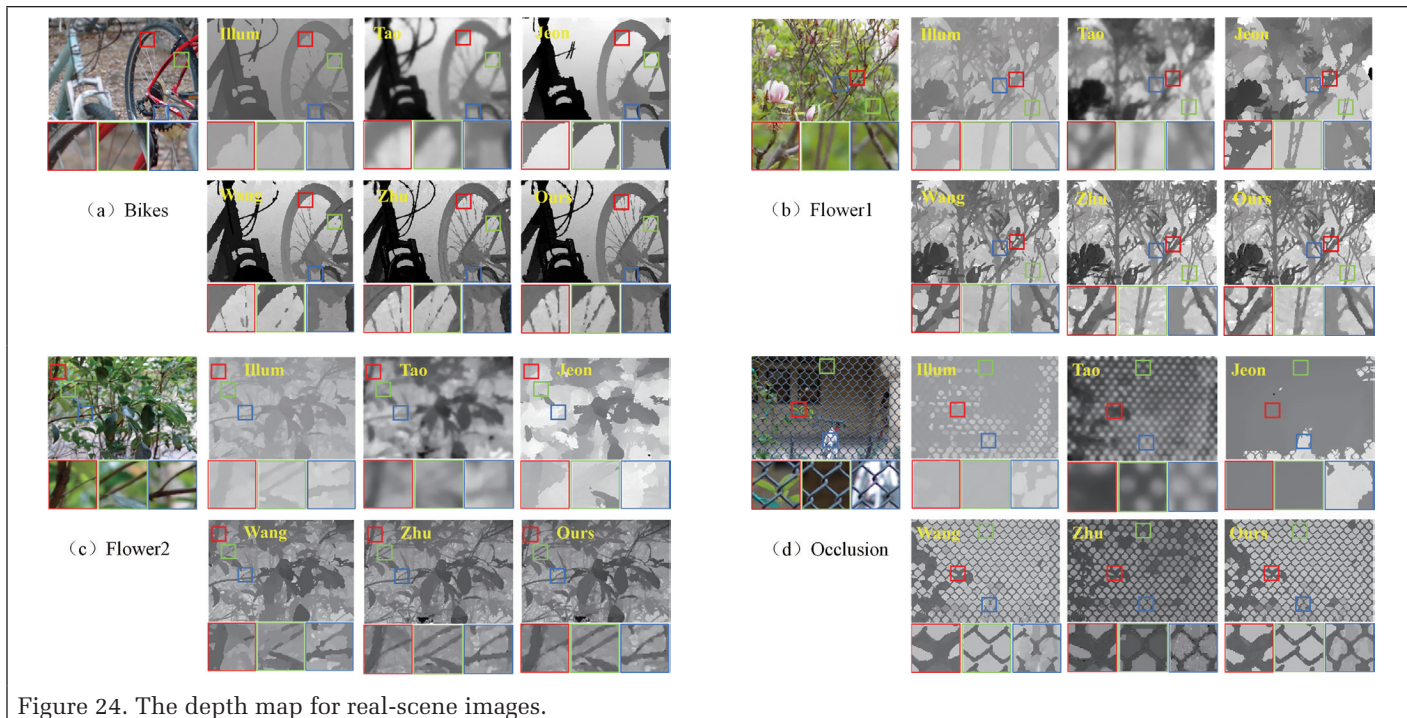


Figure 24. The depth map for real-scene images.

the Lytro Illum camera. The methods of Tao *et al.* and Jeon *et al.* still provide severely oversmooth results and fail to extract the occlusion boundaries. On the whole, the depth maps obtained by the Lytro Illum software and the methods of T.-C. Wang *et al.* and Zhu *et al.* are similar to the depth map obtained by our method; the depth of some heavy occlusion areas is also scaled up to illustrate the advantages of our method. From the enlarged close-up images, it can be seen that our algorithm can restore subtler boundaries compared with other methods. For example, the Lytro Illum software and the method of T.-C. Wang *et al.* reconstruct only a few spokes of the bicycle (Figure 24a); the method of Zhu *et al.* reconstructs more spokes, but fewer than our method. The Lytro Illum software fails to accurately restore the shape of the wire mesh (Figure 24d); the methods of T.-C. Wang *et al.* and Zhu *et al.* can reconstruct the shape of the wire mesh, but the T.-C. Wang *et al.* method breaks some intersections of wires, and the Zhu *et al.* method provides oversmooth results, and some wires cannot be distinguished from the background correctly. In comparison, our proposed method provides a more accurate depth map.

Conclusion

In this article, we proposed an algorithm to handle complex occlusion in depth estimation of a light field. The occluded pixels are effectively identified using a refocus method. For each occluded pixel, the unoccluded views are accurately selected using an adaptive unoccluded-view identification method. Then the initial depth map is obtained by computing the cost volumes in the unoccluded views. The final depth is regularized using an MRF with occlusion cues. The advantages of our proposed algorithm are demonstrated on various synthetic data sets as well as real-scene images compared with the conventional state-of-the-art algorithms. Compared with the four algorithms—Tao *et al.* (2013), Jeon *et al.* (2015), T.-C. Wang *et al.* (2016), and Zhu *et al.* (2017)—the RMS error decreases by about 15% with our proposed method on the synthetic data sets and by about 9% percent on real-scene images. Compared with the top-ranked conventional method,

OBER-cross+ANP, our method is a little higher in term of mean square error. Compared with the top-ranked deep-learning methods, our method is inferior. However, our method is a good choice if you do not have a graphics processing unit to train a network and want to obtain your disparity map as soon as possible. Because a light-field camera can reconstruct detailed three-dimensional models, it can be used in the comprehensive inspection of industrial mechanical parts, life medicine, face recognition, and the establishment of three-dimensional models in games and movies. The proposed method can be valuable in these applications.

Acknowledgments

This research is funded by the National Key Research and Development Program of China (project 2018YFB1305004) and the National Natural Science Foundation of China (project 41471388).

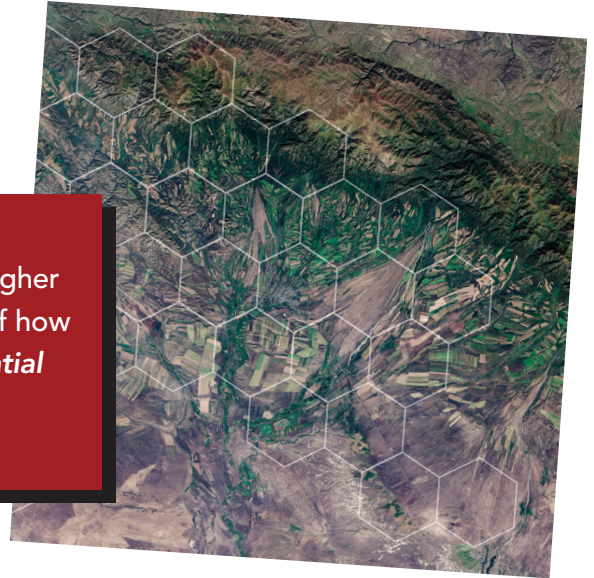
References

- Anzai, Y. 2012. Pattern Recognition and Machine Learning. Boston: Elsevier.
- Boykov, Y., O. Veksler and R. Zabih. 2001. Fast approximate energy minimization via graph cuts. *IEEE Transactions on Pattern Analysis and Machine Intelligence* 23 (11):1222–1239.
- Chen, C., H. Lin, Z. Yu, S. B. Kang and J. Yu. 2014. Light field stereo matching using bilateral statistics of surface cameras. Pages 1518–1525 in *2014 IEEE Conference on Computer Vision and Pattern Recognition*, held in Columbus, Ohio, 23–28 June 2014. Edited by J. Editor. Los Alamitos, Calif.: IEEE Computer Society.
- Dong, F., S.-H. Ieng, X. Savatier, R. Etienne-Cummings and R. Benosman. 2013. Plenoptic cameras in real-time robotics. *The International Journal of Robotics Research* 32 (2):206–217.
- Dudoit, S. and J. Fridlyand. 2002. A prediction-based resampling method for estimating the number of clusters in a dataset. *Genome Biology* 3 (7):research0036.1.
- Frey, B. J. and D. Dueck. 2007. Clustering by passing messages between data points. *Science* 315 (5814):972–976.

- Honauer, K., O. Johannsen, D. Kondermann and B. Goldluecke. 2017. A dataset and evaluation methodology for depth estimation on 4D light fields. Pages 19–34 in *Computer Vision—ACCV 2016*, held in Taipei, Taiwan, 20–24 November 2016. Edited by S.-H. Lai, V. Lepetit, K. Nishino and Y. Sato. Cham, Switzerland: Springer.
- Jeon, H.-G., J. Park, G. Choe, J. Park, Y. Bok, Y.-W. Tai and I. S. Kweon. 2015. Accurate depth map estimation from a lenslet light field camera. Pages 1547–1555 in *2015 IEEE Conference on Computer Vision and Pattern Recognition*, held in Boston, Mass., 7–12 June 2015. Edited by J. Editor. Los Alamitos, Calif.: IEEE Computer Society.
- Kim, C., H. Zimmer, Y. Pritch, A. Sorkine-Hornung and M. Gross. 2013. Scene reconstruction from high spatio-angular resolution light fields. *ACM Transactions on Graphics* 32 (4):73.
- Levoy, M. and P. Hanrahan. 1996. Light field rendering. Pages 31–42 in *Proceedings of the 23rd Annual Conference on Computer Graphics and Interactive Techniques*, held in New Orleans, La., 4–9 August 1996. Edited by J. Editor. New York: Association for Computing Machinery.
- Ma, Z., K. He, Y. Wei, J. Sun and E. Wu. 2013. Constant time weighted median filtering for stereo matching and beyond. Pages 49–56 in *2013 IEEE International Conference on Computer Vision*, held in Sydney, Australia, 1–8 December 2013. Edited by J. Editor. Los Alamitos, Calif.: IEEE Computer Society.
- Menze, M. and A. Geiger. 2015. Object scene flow for autonomous vehicles. Pages 3061–3070 in *2015 IEEE Conference on Computer Vision and Pattern Recognition*, held in Boston, Mass., 7–12 June 2015. Edited by J. Editor. Los Alamitos, Calif.: IEEE Computer Society.
- Mihara, H., T. Funatomi, K. Tanaka, H. Kubo, Y. Mukaigawa and H. Nagahara. 2016. 4D light field segmentation with spatial and angular consistencies. Pages PPP–PPP in *2016 IEEE International Conference on Computational Photography*, held in Evanston, Ill., 13–15 May 2016. Edited by J. Editor. Los Alamitos, Calif.: Institute of Electrical and Electronic Engineers.
- Ng, R., M. Levoy, M. Brédif, G. Duval, M. Horowitz and P. Hanrahan. 2005. Light field photography with a hand-held plenoptic camera. Stanford Tech Report CTSR 2005-02. <<https://graphics.stanford.edu/papers/lfcamera/lfcamera-150dpi.pdf>> Accessed DD Month YYYY.
- Perwaß, C. and L. Wietzke. 2012. Single lens 3D-camera with extended depth-of-field. *Proceedings of SPIE* 8291:829108.
- Raj, A. S., M. Lowney and R. Shah. 2016. Light-field database creation and depth estimation. <https://stanford.edu/class/ee367/Winter2016/Lowney_Shah_Sunder_Raj_Report.pdf> Accessed DD Month YYYY.
- Sabater, N., M. Seifi, V. Drazic, G. Sandri and P. Pérez. 2015. Accurate disparity estimation for plenoptic images. Pages 548–560 in *Computer Vision—ECCV 2014 Workshops*, held in Zurich, Switzerland, 6–7 and 12 September 2014. Edited by L. Agapito, M. Bronstein and C. Rother. Cham, Switzerland: Springer.
- Sasaki, Y. 2007. The truth of the F-measure. <URL> Accessed DD Month YYYY.
- Schilling, H., M. Diebold, C. Rother and B. Jähne. 2018. Trust your model: Light field depth estimation with inline occlusion handling. Pages 4530–4538 in *2018 IEEE/CVF Conference on Computer Vision and Pattern Recognition*, held in Salt Lake City, Utah, 18–23 June 2018. Edited by J. Editor. Los Alamitos, Calif.: IEEE Computer Society.
- Shin, C., H.-G. Jeon, Y. Yoon, I. S. Kweon and S. J. Kim. 2018. EPINET: A fully-convolutional neural network using epipolar geometry for depth from light field images. Pages 4748–4757 in *2018 IEEE/CVF Conference on Computer Vision and Pattern Recognition*, held in Salt Lake City, Utah, 18–23 June 2018. Edited by J. Editor. Los Alamitos, Calif.: IEEE Computer Society.
- Tao, M. W., S. Hadap, J. Malik and R. Ramamoorthi. 2013. Depth from combining defocus and correspondence using light-field cameras. Pages 673–680 in *2013 IEEE International Conference on Computer Vision*, held in Sydney, Australia, 1–8 December 2013. Edited by J. Editor. Los Alamitos, Calif.: IEEE Computer Society.
- Tosic, I. and K. Berkner. 2014. Light field scale-depth space transform for dense depth estimation. Pages 435–442 in *Proceedings of the IEEE Conference on Computer Vision and Pattern Recognition Workshops*, held in Columbus, Ohio, 23–28 June 2014. Edited by J. Editor. Los Alamitos, Calif.: IEEE Computer Society.
- Tsai, Y.-J., Y.-L. Liu, M. Ouhyoung and Y.-Y. Chuang. 2020. Attention-based view selection networks for light-field disparity estimation. *Proceedings of the 34th Conference on Artificial Intelligence*.
- Wang, K., J. Zhang, D. Li, X. Zhang and T. Guo. 2008. Adaptive affinity propagation clustering. arXiv 0805.1096.
- Wang, T.-C., A. A. Efros and R. Ramamoorthi. 2016. Depth estimation with occlusion modeling using light-field cameras. *IEEE Transactions on Pattern Analysis and Machine Intelligence* 38 (11):2170–2181.
- Wanner, S. and B. Goldluecke. 2013. Variational light field analysis for disparity estimation and super-resolution. *IEEE Transactions on Pattern Analysis and Machine Intelligence* 36 (3):606–619.
- Wanner, S., S. Meister and B. Goldluecke. 2013. Datasets and benchmarks for densely sampled 4d light fields. Pages 225–226 in *Vision, Modeling, and Visualization*, held in Lugano, Switzerland, 11 September–13 October 2013. Edited by M. Bronstein, J. Favre and K. Hormann. Goslar, Germany: The Eurographics Association.
- Yang, C., Z. Liu, K. Di, Y. Wang and M. Peng. 2019. Improved camera distortion correction and depth estimation for lenslet light field camera. *Photogrammetric Engineering and Remote Sensing* 85 (3):197–208.
- Yu, Z., X. Guo, H. Lin, A. Lumsdaine and J. Yu. 2013. Line assisted light field triangulation and stereo matching. Pages 2792–2799 in *2013 IEEE International Conference on Computer Vision*, held in Sydney, Australia, 1–8 December 2013. Edited by J. Editor. Los Alamitos, Calif.: IEEE Computer Society.
- Zhang, Z., Y. Liu and Q. Dai. 2015. Light field from micro-baseline image pair. Pages 3800–3809 in *2015 IEEE Conference on Computer Vision and Pattern Recognition*, held in Boston, Mass., 7–12 June 2015. Edited by J. Editor. Los Alamitos, Calif.: IEEE Computer Society.
- Zhu, H., Q. Wang and J. Yu. 2017. Occlusion-model guided antiocclusion depth estimation in light field. *IEEE Journal of Selected Topics in Signal Processing* 11 (7):965–978.

GEOSPATIAL REVOLUTION

With more than 1 million video views, the *Geospatial Revolution Project* is the go-to source for government, higher education, and workforce development for an overview of how geospatial technology is changing the world. The *Geospatial Revolution Project* is anchored in a world-class research university and trusted for its PBS editorial standards.



THE NEXT GENERATION

WPSU Penn State is celebrating the 10th Anniversary (2010-2020) of the launch of the original *Geospatial Revolution Project* with a new video episode about next-generation innovations in geospatial technology.

Our Emmy Award-winning production team explores stories from public safety, business, and national defense. The real revolution in geospatial technologies is just beginning!



CONTACT

Please make a philanthropic gift to WPSU Penn State to support the new episode. For more information, contact:

Elaine Brzycki
Project Development
WPSU Penn State
ejb23@psu.edu

Kristian Berg
Director, Geospatial Revolution Project
WPSU Penn State
kjb35@psu.edu

Dr. Todd S. Bacastow
Teaching Professor
Dept. of Geography • Penn State
tsb4@psu.edu

Karen Schuckman
Associate Teaching Professor
Dept. of Geography • Penn State
kls505@psu.edu

AUDIENCES & DISTRIBUTION

The new episode—with ready-made *Geospatial Revolution* audiences in government, public safety, industry, education, and the general public—will be screened at conferences, posted to social media, linked to the original project website, and shared with original engagement partners:

- U.S. government (e.g., U.S. DOD, NGA, FBI, U.S. Army Corps of Engineers)
- Higher education/workforce development collaborators
- K-12 STEM education

“Geospatial Revolution is considered the ‘Bible’ of the GIS field. I can’t wait to see the next episode!”

– Dr. Salvatore Amaduzzi
University of Udine, Italy



GEOSPATIAL REVOLUTION
geospatialrevolution.psu.edu

LEARN
DO
GIVE
BELONG

ASPRS Offers

- » Cutting-edge conference programs
- » Professional development workshops
- » Accredited professional certifications
- » Scholarships and awards
- » Career advancing mentoring programs
- » *PE&RS*, the scientific journal of ASPRS

asprs.org

ASPRS